DEVELOPMENT OF AN AUTONOMOUS SINGLE-POINT CALIBRATION FOR A
CONSTANT VOLTAGE HOT-WIRE ANEMOMETER

A Thesis

presented to

the Faculty of California Polytechnic State University,

San Luis Obispo

In Partial Fulfillment

of the Requirements for the Degree

Master of Science in Mechanical Engineering

by

Ryan Christopher Murphy

March 2015

COMMITTEE MEMBERSHIP

TITLE: Development of an Autonomous Single-Point
                             Calibration for a Constant Voltage Hot-Wire
                             Anemometer

AUTHOR: Ryan Christopher Murphy

DATE SUBMITTED: March 2015

COMMITTEE CHAIR: Russell V. Westphal, Ph.D
                             Professor of Mechanical Engineering

COMMITTEE MEMBER: Christopher C. Pascual, Ph.D
                             Professor of Mechanical Engineering

COMMITTEE MEMBER: Kira J. Abercromby, Ph.D
                             Assistant Professor of Aerospace Engineering

ABSTRACT

Development of an Autonomous Single-Point Calibration for a Constant Voltage Hot-Wire Anemometer

Ryan Christopher Murphy

Traditionally, the measurement of turbulence has been conducted using hot-wire anemometry. This thesis presents the implementation of a constant voltage hot-wire anemometer for use with the Boundary Layer Data System (BLDS). A hot-wire calibration apparatus has been developed that is capable of operation inside a vacuum chamber and flow speeds up to 50 m/s. Hot-wires operated with a constant-voltage anemometer (CVA) were calibrated at absolute static pressures down to 26 kPa. A thermal/electrical model for a hot-wire and the CVA circuit successfully predicted the measured CVA output voltage trend at reduced pressure environments; however, better results were obtained when the Nusselt number was increased. A calibration approach that required only one measured flow speed was developed to allow autonomous calibrations of a CVA hot-wire. The single-point calibration approach was evaluated through comparison with the experimental data from the vacuum chamber over a range of 14-50 m/s and at pressures from 26 to 100 kPa. The thermal-electrical model was used to make predictions of CVA output voltage and the corresponding flow speed for conditions that could not be replicated within a laboratory. The first set of predictions were made for conditions from 7.5 to 100 kPa, at a constant temperature of 25$^\mathbf{o}$C, within a flight speed range of 40 to 150 m/s. Single-point calibrations were developed from these predictions. Additionally, the thermal-electrical model was used to predict hot-wire response for a change in temperature of $\pm$ 25$^\mathbf{o}$C at 26 kPa and the single-point calibration developed for the pressure range 7.5 to 100 kPa was tested for its ability to adjust. The temperature variation at a single pressure of 26 kPa proved that the single-point function was capable of adapting to off-standard temperatures with the largest deviations of +/- 7% in the mid-range velocities. With a temperature drop, the deviations were below 5%. The second set of thermal-electrical predictions involved conditions for altitude from 0 to 18 km at flow speeds from 40 to 150 m/s. A single-point calibration was developed for altitude conditions. Furthermore, to test the single-point calibration the thermal-electrical model was used to predict hot-re response for a temperature variation of $\pm$ 25$^\mathbf{o}$C at 18 km. The single-point calibration developed for altitude proved that it was capable of adjusting to a temperature variation of $\pm$ 25$^\mathbf{o}$C with maximum deviations of about 5% at mid-range velocities. It is proposed that the single-point calibration approach could be employed for CVA measurements with the Boundary Layer Data System (BLDS) to allow hot-wire data to be acquired autonomously during flight tests.

Keywords: Hot-wire, constant voltage anemometer, boundary layer, calibration jet apparatus, BLDS, frequency response, laminar-to-turbulent transition, vacuum chamber

ACKNOWLEDGMENTS

TABLE OF CONTENTS

LIST OF FIGURES

NOMENCLATURE

A	=	Power law offset coefficient
a_w	=	OHR - 1
B	=	Power law multiplying factor
c_w	=	Specific heat capacity for tungsten wire, 140 J/kg-K in prediction model
Cp	=	Pressure Coefficient
D	=	Hot-wire probe wire diameter, μm
E	=	Mean voltage output from HWA, V
E_w	=	Elastic modulus of tungsten wire, 400 GPa
e	=	Instantaneous HWA output voltage, V
f	=	Friction factor
g	=	Gravitational constant, 9.81 m/s^2, 32.2 ft/s^2
G	=	Feedback amplifier gain for CTA
H	=	Amplitude ratio
h	=	Heat transfer convection coefficient, W/(m^{2}K)
I_T	=	Total feedback current in CVA circuit analysis
I_w	=	CVA output proportional to current, V
$\varDelta I_w$	=	CVA output difference between actual temperature and reference, V
$I_{w,Corrected}$	=	Corrected CVA output calibration data, V
k	=	Exponent for inverted calibration curve power law
$k_{f,\infty}$	=	Thermal conductivity of air at film or fluid temperature, W/m-K
k_L	=	Loss coefficient
L	=	Hot-wire probe wire length, 1.27 mm for 1210-T1.5
L_C	=	Adjustable inductor for cable inductance compensation, H
M	=	Time constant for HWA system (CCA, CTA, or CVA), ms
M_n	=	Mach number
N	=	Number of data points for mean square error calculation
Nu	=	$\dfrac{hD}{k_f}$ (Nusselt number)

n	$=$	Power law exponent
OHR	$=$	Traditional overheat ratio, ratio of hot to cold probe resistance
P_T	$=$	Total pressure, inH_2O
P_s	$=$	Fan static pressure, inH_2O
ΔP	$=$	Plenum pressure difference, inH_2O
q	$=$	Dynamic pressure, inH_2O
R_0	$=$	Probe resistance at 20 °C reference temperature, Ω
R_1	$=$	HWA fixed circuit resistor, 5000 Ω in CVA prediction model
R_2	$=$	HWA fixed circuit resistor, 50 Ω in CVA prediction model
R_3	$=$	Adjustable resistor for balancing bridge circuit, Ω
$R_{a,b}$	$=$	Resistance of hot-wire probe at conditions a and b
R_{box}	$=$	Resistance of internal circuitry of CVA system, Ω
R_{cable}	$=$	Resistance of probe BNC cable, Ω
R_{DVM}	$=$	Probe resistance at ambient temperature measured by DVM, Ω
Re	$=$	$\dfrac{\rho_f UD}{\mu_f}$ (Reynolds number)
R_F	$=$	CVA circuit resistor, 1000 Ω in prediction model
R_{int}	$=$	Resistance inside hot-wire probe, before actual wire sensor, Ω
R_L	$=$	Resistance of probe cable in anemometer circuit, Ω
R_s	$=$	Adjustable resistor to vary source current, Ω
$R_{support}$	$=$	Resistance of probe support stem, Ω
R_T	$=$	Total feedback resistance in CVA circuit analysis, Ω
R_w	$=$	Resistance (hot) of hot-wire probe at operating temperature, Ω
R_∞	$=$	Resistance (cold) of hot-wire probe at ambient temperature, Ω
P	$=$	Offset coefficient for inverted calibration curve power law
Q	$=$	Multiplier coefficient for inverted calibration curve power law
$S_{T\infty}$	$=$	Freestream temperature sensitivity coefficient
S_u	$=$	Velocity sensitivity coefficient
$T_{a,b}$	$=$	Temperatures at different conditions a and b, °C
T_f	$=$	Film temperature, °C
T_w	$=$	Hot-wire sensor operating temperature, °C

T_∞	=	Ambient fluid temperature, °C
U	=	Freestream velocity, m/s
u	=	Instantaneous velocity, m/s
V_1	=	Voltage source powering HWA circuit, V
V_o	=	Op-amp output from prototype CVA system, $V_o = V_s/2$
V_s	=	Op-amp output voltage for simplified circuit in literature, V
V_w	=	Probe wire voltage set-point, V
z	=	Height, feet
α_0	=	Temperature coefficient of resistance at 20 °C reference, 0.0042 °C^{-1}
β	=	Screen open area ratio
ε	=	Equivalent roughness, feet
$\mu_{f,\infty}$	=	Air viscosity at film or fluid temperature, N-s/m^2
$\rho_{f\infty}$	=	Air density at film temperature or fluid temperature, kg/m^3
ρ_w	=	Density assumed for platinum plated tungsten wire, 20,000 kg/m^3
θ_∞	=	Fluctuating ambient fluid temperature, °C
γ	=	Specific weight, lb/ft^3

1. Introduction

In-flight calibration of an anemometer is a very challenging proposition, therefore, developing an autonomous calibration for a constant voltage hot-wire anemometer for the sake of boundary layer measurements at various altitudes (i.e. decreased density), is the next step to further the knowledge of boundary layer data at high altitudes and to verify laminar flow over the surface of aircraft. Aerodynamic refinements in the 1930's led to, "low drag coefficients achieved by internally braced monoplanes equipped with retractable landing gears", which, "suggested that any further large reductions in drag could only be achieved through the maintenance of extensive laminar flow over the surface of the aircraft" [1]. Ludwig Prandtl's boundary layer theory suggests that near the surface of an object immersed in a flow, a thin region will form, where at the surface-fluid interface a no-slip condition occurs so that the fluid is stationary relative to that surface. The boundary layer is comprised of large velocity gradients and, depending on the Reynolds number, the velocity at some small distance normal to the wall will be approximately equal that of the free stream. Outside the boundary layer, inviscid flow theory holds true. For Newtonian fluids (air, water, etc.), the shear stresses within the fluid are proportional to the large velocity gradients; therefore boundary layers apply a significant "skin-friction" drag tangent to the surface [2]. Laminar flows may be thought of as layers of undisturbed fluid sliding steadily over one another and there is diminutive interchange of fluid mass between the adjacent layers. Thus, momentum exchanges within the laminar boundary layer are due entirely to the viscosity of the fluid [3].

For initially laminar flow, the Reynolds number increases as the flow develops and the boundary layer will possibly transition to a state of turbulence. In turbulent flows, substantial ostensibly random motion occurs, in the form of velocity fluctuations both along the mean direction of the flow and perpendicular to it. Turbulence, characterized by space and time, may be time-averaged to define the velocity profile. Mixing and diffusion occur between the adjacent layers due to the perpendicular fluctuations; thus increasing the shear stresses within the boundary layer [3]. The shearing stresses of a turbulent boundary layer are a result of viscous fluid motion and Reynolds stresses causing the skin friction coefficient for turbulent flow to be considerably larger than that of laminar flow. Thus, increasing the extent of laminar flow over the surface of an aircraft can provide a substantial reduction in total drag and improve fuel efficiency.

To date, there is no comprehensive theory that can predict transition from laminar to turbulent flow for realistic situations including wing-type flow and flow disturbances. However, there are observations and empirical correlations supported by over a century of research. Linearized stability theory assesses the stability of the Navier-Stokes equations which predicts the amplification of certain types of disturbances in laminar flow on a smooth surface at some finite Reynolds number, but cannot predict turbulence. Subsequently, the flow becomes unstable; infinitesimal disturbances entering the boundary layer will amplify and develop into two-dimensional wave-like disturbances known as Tollmien-Schlichting (TS) waves. After reaching the critical Reynolds number, the flow disturbances will continue to grow and become three-dimensional; the formation of turbulent spots can occur which combine into fully turbulent flow [4] [5].

Transition can be delayed to increase the extent of laminar flow by using wall shaping techniques to produce favorable pressure gradients. This technique is a form of passive laminar flow control referred to as natural laminar flow (NLF) [6]. This concept initiated the development of laminar flow airfoils in the late 1930's by the NACA [1]. By designing for a favorable pressure gradient, the freestream flow is not permitted to deaccelerate, thus sustaining the thin laminar boundary layer. Numerical computations by Wazzan [7] [5] for the conditions of boundary layer similarity known as the Falkner-Skan flows indicates that for favorable pressure gradients the boundary layer remains stable to a considerably greater Reynolds number. Furthermore, when the flow does become unstable, the amplification rates are significantly reduced [7] [5] [4].

Separation of a laminar boundary layer flow is another mechanism that can cause transition to turbulence. A great number of airfoils are designed with high local curvature over the forward part of the chord. At a large angle of incidence, the laminar boundary layer will approach the point of maximum airfoil thickness where the adverse pressure gradient may initiate laminar separation. As a result, the separated boundary layer may transition to a state of turbulence with characteristic rapid thickening. If the surface length permits adequate thickening, the turbulent shear layer may contact the surface and reattach as a turbulent boundary layer. Consequently, a separation "bubble" will be trapped under the shear layer between the separation and reattachment locations [3]. Natural transition usually occurs immediately within the separation region [4].

Nonlinear bypass transition is an additional mechanism through which a flow can become turbulent before the predicted transition location. While extraordinary levels of preliminary disturbances exist, transition may occur through nonlinear mechanisms, entirely bypassing the linear stability regime. This type of transition process may include external disturbances such as freestream vorticity, freestream sound, particulates, high amplitude acoustic waves and surface imperfections. The latter is of particular practical interest and includes roughness (both discrete and distributed), steps, gaps and waviness. The physics through which bypass transition takes place is not well understood. LFC designers, using linear stability theory as an analytical tool, must avoid any disturbance mechanism which initiates early transition. Modern manufacturing advancements, including composite aircraft construction, specialized clear coats and the addition of polymer coatings, have aided in keeping the disturbance levels to a minimum [8].

Computational analysis tools are commonly employed to design for and predict transition to turbulence on aircraft surfaces. Currently, the most widely used tool is computational fluid dynamics (CFD). Other tools include in-house computational codes such as the transition analysis program system (TAPS), developed by Wazzan and others [4], and a similar program; the compressible stability analysis code (COSAL), developed by Malik [4]. While computational tools offer a particularly attractive means of transition prediction and turbulent flow simulation, the engineer is still faced with a few consequential realizations; transition theory is limited to linear stability and amplification, there is no general solution for turbulent flow, and what does exist is based largely on empirical correlations. Therefore, experimental validation is often deemed necessary.

For aircraft applications, experimentation is typically conducted with wind tunnels: a scaled model of the aircraft or a section of the aircraft is placed inside the test section where measurements can be taken. Although wind tunnels have seen drastic improvements throughout the last century, they continue to present obstacles during experiments. Wind tunnel walls can influence the pressure distribution over the model and tend to have higher freestream turbulence which can initiate transition earlier than might occur in flight. Flight tests have proven to be vital for experimental validation, but they are costly for numerous reasons. For example, to instrument an aircraft for surface pressure measurements requires drilling a hole in the surface and connecting internal plumbing and additional instrumentation. This sort of alteration to an aircraft is not only costly, but creates safety-of-flight concerns that are often seen as insurmountable. However, measurements from flight tests continue to be seen as highly desirable particularly when laminar flow diagnosis is required.

In pursuance of flight test data, Northrop Grumman Corporation has sponsored the development of the Boundary Layer Data System (BLDS) [9] [10]. The BLDS series of devices are compact, lightweight, autonomous, internally-powered, capable of being affixed to most locations on an aircraft, and measure a host of boundary layer properties to characterize the boundary layer as well as other important fluid properties. BLDS devices are programmed preflight with a laptop, operate autonomously during flight, and data is offloaded post-flight. This ensures that there is no interruption of standard flight procedures. The BLDS comes in numerous configurations depending on the desired measurements and application. The internal software of BLDS devices is programmed to record only time-averaged pressures. One example BLDS configuration is the Preston tube data system (PTDS), as seen in Figure 1.1, which utilizes a Pitot tube placed in the freestream, above the aircraft surface, to measure the local total pressure,

a static probe on the surface to measure the local surface static pressure and a Preston tube placed directly on the surface. Essentially, PTDS data can be used to calculate local skin friction and dynamic pressure; these results can then be used to determine if the flow is laminar or turbulent based on the large increase in skin friction that accompanies transition. Another version of BLDS, as seen in Figure 1.2, utilizes a fixed freestream total pressure probe and a wall static probe with a pressure probe that is mounted to a motor driven stage that traverses the probe through the boundary layer. This system not only characterizes the boundary layer profile, but also provides the skin friction. This data can be used to determine the laminar-to-turbulent transition location. The traversing stage can be outfitted with many configurations including, but not limited to, a Pitot probe, a Conrad Probe, a rotatable single-hole probe; the latter is capable of measuring 3-component mean velocity profiles.
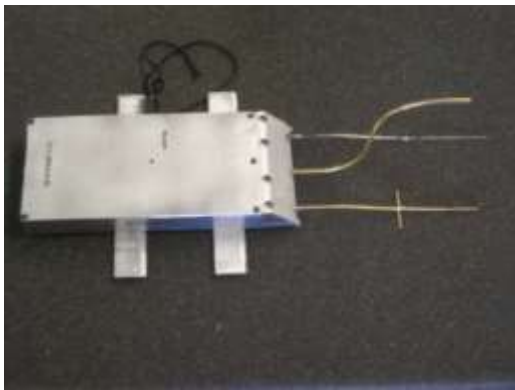
Figure 1.1 Preston tube data system (PTDS) [11]
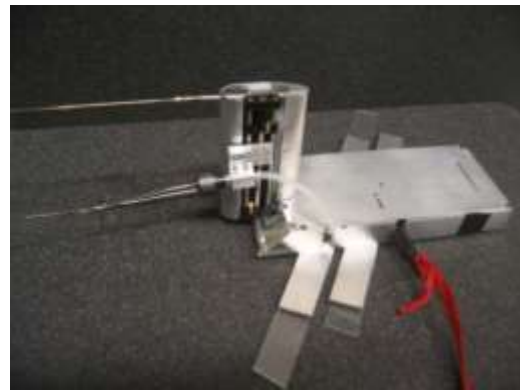
Figure 1.2 Boundary layer data system [11]

More recently, the BLDS has been successfully outfitted with devices capable of direct measurements of flow fluctuations to detect the onset of transition. One method of measuring turbulence is by measuring the fluctuating pressure [4]. Karasawa [11] investigated the implementation of a Kulite Model XCS-062-5D dynamic pressure transducer (Figure 1.3) on the

PTDS to measure the total pressure fluctuations in a flat plate boundary layer. Her results indicated that the root-mean-square (RMS) of the total pressure fluctuations was less than 1% of the local dynamic pressure in the laminar boundary layer, but was approximately 2% in the fully turbulent case. At the transition location, the RMS was approximately 4%, which demonstrated successful transition detection. However, freestream measurements indicated a noise floor of 1%, so a low signal-to-noise ratio was attained.
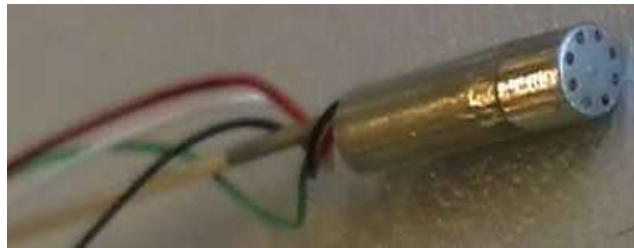
Figure 1.3 Kulite Model XCS-062-5D [11]

Lillywhite **[5]** investigated the implementation of low-cost microphones in a variety of probe configurations to measure the RMS of total pressure fluctuations in order to detect transition. His results showed that, at low dynamic pressures, that the RMS pressure fluctuations measured in turbulent boundary layers were up to ten times larger than that of laminar. Probe Configuration # 1 (Figure 1.4), proved to be the best choice due to its small size and ability to measure the pressure spectrum without resonant distortion. Unfortunately, as dynamic pressure is increased, the amplitude of the pressure fluctuations increases until clipping ensues and causes the difference in fluctuating total pressure divided by the local dynamic pressure ($p'_{t,RMS}/q_e$) to decrease as does the capability to differentiate between laminar and turbulent boundary layer **[5]**. This means the microphone configurations tested can only be used in low speed wind tunnel experiments. Direct measurement of the mean and fluctuating velocity components allow for

high spatial resolution and very low noise with RMS fluctuations less than 0.01% **[12]**. Thus, hot-wire anemometry measurements of velocity fluctuations have the potential to provide greater sensitivity for transition detection.
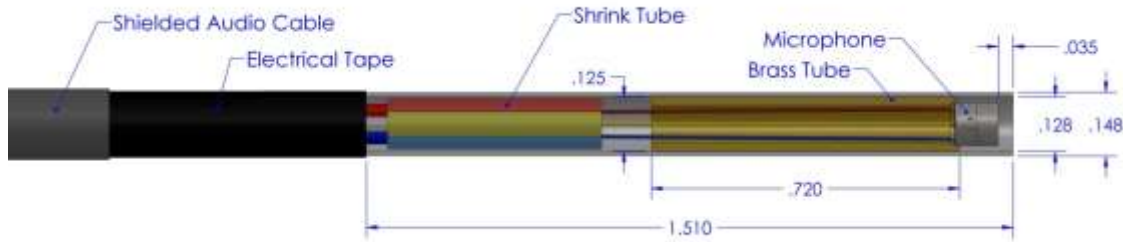
Figure 1.4 Section view of the microphone probe Configuration #1 [5]

Hot-wire anemometers are widely used in fluid mechanics research to measure the mean and fluctuating flow components. Additionally, hot-wires have remained successful in compressible flow research for over 60 years [13], which indicates that they are well-suited for high speed experiments, in contrast to the above stated pressure fluctuation methods. Also, hot-wire anemometers have proven effective in determining the location of shock-induced boundary layer separation at transonic speeds [14]. Three different hot-wire configurations exist; Constant Temperature Anemometer (CTA), Constant Current Anemometer (CCA) and more recently the Constant Voltage Anemometer (CVA) [15]. The sensing element, a fine wire is heated above the ambient temperature by passing sufficient current through the wire. Convection due to the fluid flow causes heat loss from the wire which, depending on the type of hot-wire, will change the wire's electrical properties; as depicted in Figure 1.5 and Figure 1.6. Thus a given power or current will correspond to a specific flow velocity if the flow temperature is kept constant or known [16]. All hot-wire configurations possess an inherent time constant, where instantaneous changes in velocity correspond to a delay in temperature change. Consequentially, hot-wire frequency

8

response is adversely affected by thermal inertia which behaves like a first-order low-pass filter to velocity fluctuations.
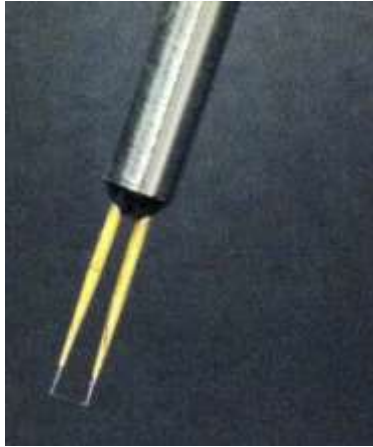
Figure 1.5 Commercial hot-wire probe (TSI 1210-T1.5) [17]
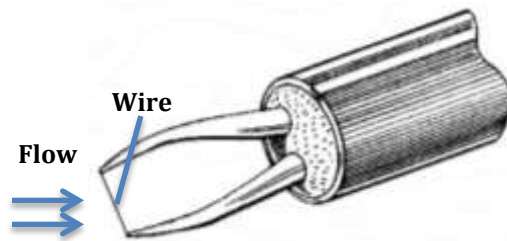
Figure 1.6 Diagram of hot-wire probe [17]

Hot-wire frequency response is the quantifiable frequency range of velocity fluctuations or disturbances [17]. The frequency response of a hot-wire alone will be, typically, a few hundred Hertz for CCA; a few kHz for CVA, but with proper circuit compensation, the limit can be extended within a range of tens to a few hundred kHz for CTA [18]. Outside of a hot-wire system's expected frequency range, velocity fluctuations become damped and can contaminate the data. Therefore operating within the transitional frequency range is of great importance to determine the laminar-to-turbulent transition location. Using the spatial stability plot developed by Wazzan [7], Neumeister [17] was able to predict the expected frequency range in the transitioning boundary layer on a flat plate. The neutral curve (Figure 1.7) displays the expected frequency range for amplified disturbances as a function of distance on the flat plate (i.e. increasing Reynolds number). The curve begins with the highest frequencies at 5,720 Hz at the

minimum critical Reynolds number based on the boundary layer displacement thickness, $Re_{\delta*}$, of 520, which is the minimum Reynolds number for initial instability [4].
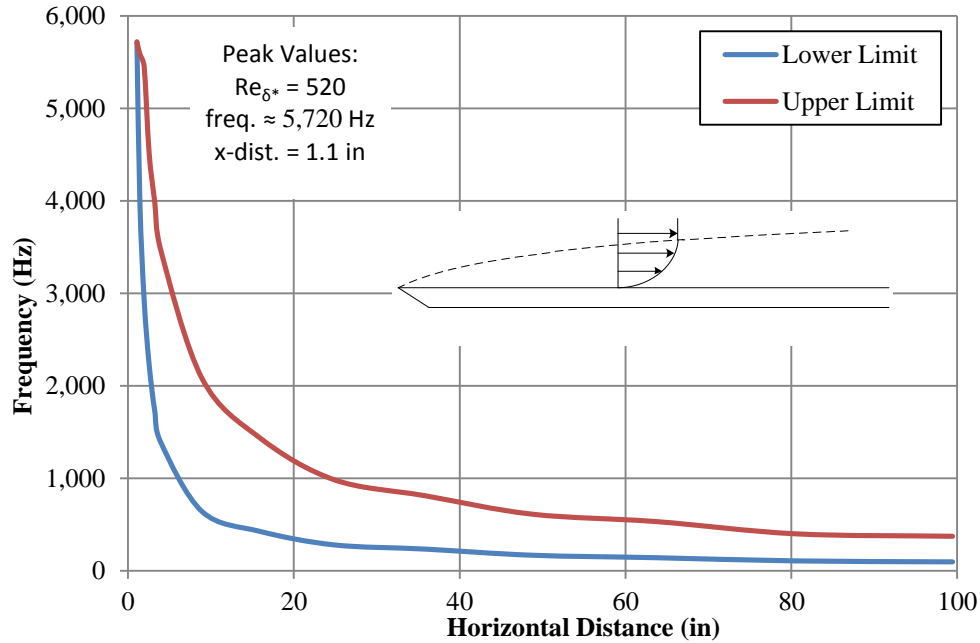
Figure 1.7 Estimated frequencies of amplified disturbances in the flat plate boundary layer for 50 m/s freestream velocity and sea level air properties from the spatial stability plot [17] [7]

Neumeister [17] investigated all three common hot-wire circuits for implementation into BLDS. The Constant Voltage anemometer (CVA) was chosen due to its ease of hardware integration, the absence of a delicate bridge, and a desirable frequency response without the need for bridge "tuning". Using the Collis and Williams thermal correlation coupled to the electrical model of the CVA operating circuit, an approximate thermal/electrical prediction model was developed [19]. A bench top CVA system was developed by BLDS consultant Don Frame. The system was used to calibrate a 3.8 micron diameter, 6 ohm cold resistance, platinum-coated tungsten probe (TSI 1210-T1.5) in the laminar jet of a velocity calibrator. To fit the calibration data for converting the CVA data to velocity, a power law calibration curve proved to be

suitable. The thermal/electrical CVA model was found to undershoot the true hot-wire behavior by 10%. In anticipation of future flight testing, the thermal/electrical CVA model was used to predict behavior at high altitude (decreased density and temperature) [17]. A large temperature increase is undesirable since temperature is held constant for prediction results to keep the calibration equation as a single degree of freedom. Additionally, temperature drift does not occur for flight conditions, therefore predicting and validating hot-wire performance at constant temperature is necessary. To accommodate temperature drift, Neumeister [17] investigated the "pdr" calibration method first introduced by Sarma and Comte-Bellot [20]. However, the results predicted that the pdr method would not compensate for low air density at high altitude and that the frequency response would also drop at high altitude.

Li [21], took CVA research one step further, by implementing CVA on BLDS. After testing in the Northrop Grumman's Variable Temperature Research Wind Tunnel, it was apparent that a slightly off-standard temperature would not be enough to vary the density and validate the thermal/electrical CVA model. However, after investigating the temperature drift caused by the conduction from the wind tunnel fan motor to the free stream air, Li [21] suggested a simple, but elegant solution for temperature drift; the thermal/electrical CVA model from Neumeister [17] was used to solve for a prospective temperature change. The temperature change was then applied to the data so that temperature is kept as a constant variable. In addition, Li [21] used the thermal/electrical CVA model to predict hot-wire results for high altitude conditions at typical flight cruise speeds.

Hot-wire anemometer calibrations require a benchtop flow with a variable flow speed at an approximate fixed temperature and fixed static pressure. The hot-wire response is then fitted to the known velocity variation, producing the calibration curve. Calibrating a hot-wire in a

11

laboratory setting is very simple, but many problems are introduced when a calibration is necessary during flight. In-flight calibrations require implementing a lab procedure at some cruise altitude, where you want boundary layer data and calibrating there. If the flight is piloted, the pilot would have to vary the air speed, which would be very time consuming. Additionally, the air speed cannot be varied too much at altitude or the aircraft could lose lift. Alternatively, an extensive calibration matrix can be developed on the ground. However, facilities with the ability to create the necessary combination of velocity, pressure and temperature, needed to create this matrix, do not exist. Hypothetically, if such a facility was possible and the matrix was created at standard atmosphere, a broad range of temperature exists at altitude.

The objective of this thesis is to develop an in-flight autonomous single-point calibration for a constant voltage hot-wire anemometer (CVA) for BLDS. First, the design of a calibration apparatus capable of operation inside a vacuum chamber will be presented in thorough detail. The calibration jet apparatus will be used to calibrate a hot-wire at conditions involving decreased pressures which presents the pressure range of ¼ ATM to 1 ATM. The experimental results will be compared to the thermal/electrical model and the appropriate adjustments will be made to better predict CVA output voltage. CVA frequency response and sensitivity will be predicted using the conditions recorded for the experimental data. Power-law fits will be applied to the experimental data which will then be used to develop a single-point calibration function which can later be implemented on BLDS for different altitudes and flight conditions. A summarized approach for implementation will be laid out and a flow chart will be presented in Appendix H. Predictions for flight conditions at altitude will be made using the adjusted thermal/electrical model and the single-point calibration will be applied to the results. CVA frequency response and sensitivity will also be discussed for altitude.

2. Calibration Apparatus Development

Design Requirements

To validate the thermal/electrical CVA model results for high altitude conditions, the calibration apparatus needed to be able to operate inside the Cal Poly Aerospace Department's Space Environment Lab vacuum chamber. Ideally, a thermal vacuum chamber (TVAC) would have been the best test-bed to simulate high altitude flight conditions. Unfortunately, the only working TVACs at Cal Poly are in high demand and have a lengthy waitlist. The desired environment involved an operating pressure range of ¼ to 1 ATM (190 to 760 Torr) which corresponds to an approximate altitude range of 31,800 feet to sea level. The apparatus had to be compact to fit within the vacuum chamber (17inch ID x 22inch deep), simple to assemble/disassemble and still capable of hot-wire probe attachment. To accommodate the existing hot-wire probe with its sensor length of 1.7 mm, a removable nozzle with a 10 mm exit diameter was chosen. Since the Cal Poly Mechanical Engineering Department's wind tunnels are capable of 0 to 110 mph, it was seen fit to design the apparatus with a comparable flow speed. To achieve quality flow characteristics the apparatus needed the appropriate flow conditioning.

Nozzle

The nozzle profile was a scaled down version of TSI model 1128 nozzles [22]. A polynomial wall shape was chosen with a slight curvature at the inlet and no slope at the exit. An initial 10 mm nozzle exit diameter was selected to match the minimum TSI 1128 nozzle size [22]. An inlet to exit diameter ratio of 7 was chosen to fit well within the recommended range of 4 – 8 [23] which gave an inlet diameter of 2.73 inches.

Pre-conditioning and flow conditioning

Pre-conditioning elements consisted of a coarse mesh followed by a medium mesh, spaced 5/8 inch apart. The coarse 4 x 4 stainless steel mesh chosen had an open area of 62 % and a wire diameter of 0.054 inch. The medium 24 stainless steel mesh chosen had an open area of 67.2 % and a wire diameter of 0.0075 inch. The coarse and medium meshes treat the gross swirl and mean axial flow non-uniformities exiting the fan. The honeycomb was placed 1/2 inch downstream of the medium mesh to provide further flow straightening because it cannot endure more than minor flow angularities [23]. The flow conditioning elements consisted of the PN1 commercial grade aramid fiber honeycomb with a 90% open area, 1/4 inch cell and 1.5 inches in length placed against fine 32 stainless steel mesh chosen had an open area of 62.7% and a wire diameter of 0.0065 inch.

Conditioning element framework and settling chamber duct-work

Acrylic tubing was chosen for its machinability and geometric dimensions. The tubing size chosen was 2.75 ID and 3.25 inch OD so that 1/4 inch wide 1/8 inch closed cell foam could be used to seal between adjacent conditioning elements.

Loss Estimates for individual parts and total system

The Hydraulic Energy equation was used to determine the fan total pressure (FTP) which was used to determine the fan static pressure (FSP) to compare with published commercial fan data. Initial hand calculations were performed for all system losses at 1/4 ATM and 110 mph. An annotated sketch was drawn to assist in the system analysis (Figure 2.1).

14
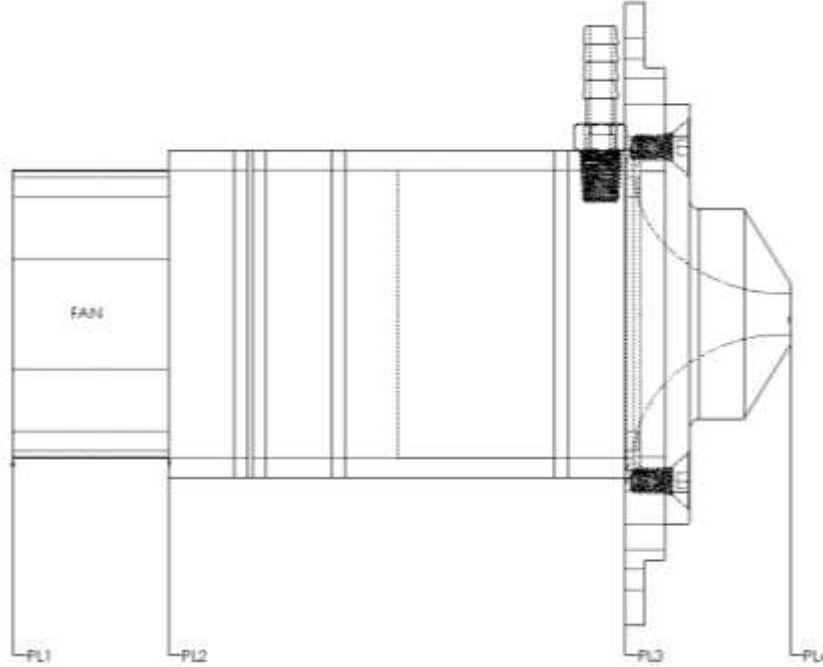
Figure 2.1 Basic Sketch for Pressure Calculations

Initially, the analysis development involved the section from plane 2 to plane 3, as follows:

$$P_2 + \frac{\rho U_2^2}{2} + \gamma z_2 = P_3 + \frac{\rho U_3^2}{2} + \gamma z_3 + \gamma h_{L_{2,3}}. \tag{2.1}$$

Neglecting gravitational effects yields the following equation:

$$P_{T2} = P_3 + \frac{\rho U_3^2}{2} + \gamma h_{L_{2,3}}. \tag{2.2}$$

Then, the section from plane 3 to plane 4 was considered:

$$P_3 + \frac{\rho U_3^2}{2} + \gamma z_3 = P_4 + \frac{\rho U_4^2}{2} + \gamma z_4 + \gamma h_{L_{3,4}}. \tag{2.3}$$

Once again, neglecting gravitational effects yields:

$$P_3 = P_4 + \frac{\rho(U_4^2 - U_3^2)}{2} + \gamma h_{L_{3,4}}. \tag{2.4}$$

Now, taking (2.4) and plugging it into (2.2) gives:

$$P_{T2} = P_4 + \frac{\rho U_4^2}{2} + \gamma h_{L_{2,3}} + \gamma h_{L_{3,4}}. \tag{2.5}$$

The fan total pressure can be calculated as follows:

$$P_T = P_{T2} - P_{T1}. \tag{2.6}$$

A second equation for the FTP is given as:

$$P_T = P_s + \frac{\rho U_{Fan}^2}{2}. \tag{2.7}$$

Rearranging (2.7) to solve for the FSP, assuming P_{T1} is equal to the chamber static pressure P_1, and substituting into (2.6) gives:

$$P_s = P_{T2} - P_1 - \frac{\rho U_{Fan}^2}{2}. \tag{2.8}$$

Substituting (2.5) for the total pressure at 2 produces:

$$P_s = P_4 + \frac{\rho U_4^2}{2} + \gamma h_{L_{2,3}} + \gamma h_{L_{3,4}} - P_1 - \frac{\rho U_{Fan}^2}{2}. \tag{2.9}$$

The static pressure at the nozzle must be equal to the static pressure in the chamber. Thus $P_4 = P_1$ gives the final equation for FSP:

$$P_s = \frac{\rho(U_4^2 - U_{Fan}^2)}{2} + \gamma h_{L_{2,3}} + \gamma h_{L_{3,4}}. \tag{2.10}$$

The losses were organized in the following manner:

$$\gamma h_L = \gamma h_{L,Major} + \gamma h_{L,Minor}. \tag{2.11}$$

First, the major losses throughout the ductwork were considered due to the skin friction along the tubing walls. The total length of all tubing including fan walls was approximately 8.25 inches. The major losses associated with the duct were calculated using the following [24]:

$$\gamma h_{L,Major} = f \frac{l}{D_{2,3}} \frac{\rho U_{2,3}^2}{2}. \tag{2.12}$$

The major losses throughout the nozzle are calculated with the following equation:

$$\gamma h_{L,Major_{3,4}} = f_{3,4} \frac{l_{3,4}}{D_4} \frac{\rho U_4^2}{2}. \tag{2.13}$$

The friction factor f, can then be found using the *Colebrook formula* [24]:

$$\frac{1}{\sqrt{f}} = -2.0 \log \left(\frac{\varepsilon/D_{2,3}}{3.7} + \frac{2.51}{Re\sqrt{f}} \right). \tag{2.14}$$

Drawn Plastic Tubing: $\varepsilon = 0.000005\ feet$

Next to be considered, were the minor losses due to pre-conditioning and flow conditioning. Losses due to honeycomb are usually less than 5 % of the total loss and are therefore negligible [25]. Low flow velocity within the tubing, ensure that the meshes cause minimal losses. Therefore, the analysis does not consider a change in velocity past each subsequent mesh. The minor losses within the mesh can be calculated using:

$$\gamma h_{L,Minor_{2,3}} = \gamma h_{L,Minor\_Meshes}, \tag{2.15}$$

which is dependent on the velocity throughout the duct and loss coefficient of each mesh.

$$\gamma h_{L,Minor\_Meshes} = \frac{K_L \rho U_{2,3}^2}{2}. \tag{2.16}$$

The following equation was developed for the mesh loss coefficient, using empirical correlations [26]:

$$K_L = 6.5 \left[\frac{1 - \beta}{\beta^2} \right] \left[\frac{U_{2,3} d}{\beta v} \right]^{-0.33}. \tag{2.17}$$

$$\beta \equiv Screen\ Open\ Area\ Ratio$$

$$d \equiv Screen\ Wire\ Diameter$$

Normally, any losses through the meshes can be neglected because the pressure losses associated are typically less than 1%. However, equation (2.16) and (2.17) were kept for completeness to show the pressure loss dependence on velocity. The minor losses within the nozzle can also be neglected when the nozzle is well-rounded. However, the equation is presented below for completeness [24]:

$$\gamma h_{L,Minor_{3,4}} = \frac{K_L \rho U_4^2}{2}. \tag{2.18}$$

Well-Rounded Nozzle Entrance: $K_L = 0$

Once all equations and calculations were checked with a hand calculation, an Engineering Equation Solver (EES) code was developed that could easily be altered given a change in fan diameter or system component (Appendix C). Fan scaling laws [24] were implemented to compare to commercial fan curves at standard atmospheric pressure. Evaluation of available fans revealed that two axial fans in series could produce the desired flow and pressure, as explained in the next section.

Fan Selection

The fans required for the calibration apparatus needed to be low cost and readily available. These constraints led to one option; PC/server cooling fans available in small quantities over the internet. San Ace 9GA0712P1G001 high static pressure fans were chosen to accomplish the desired flow speeds. Although the operating point is near the shut-off pressure, this was the best option given the constraints. The life of the fans is of no concern given the low cost. A range of nozzle sizes of $10 - 19$ mm ($\approx 3/8 - 3/4$ inch) was implemented within the EES code to display the possible operating point ranges. Fan scaling laws were used to shift the fan curve down to match an operating point of 110 MPH at an FSP of 5.80 inH_2O and 7.83 CFM (Figure 2.2).
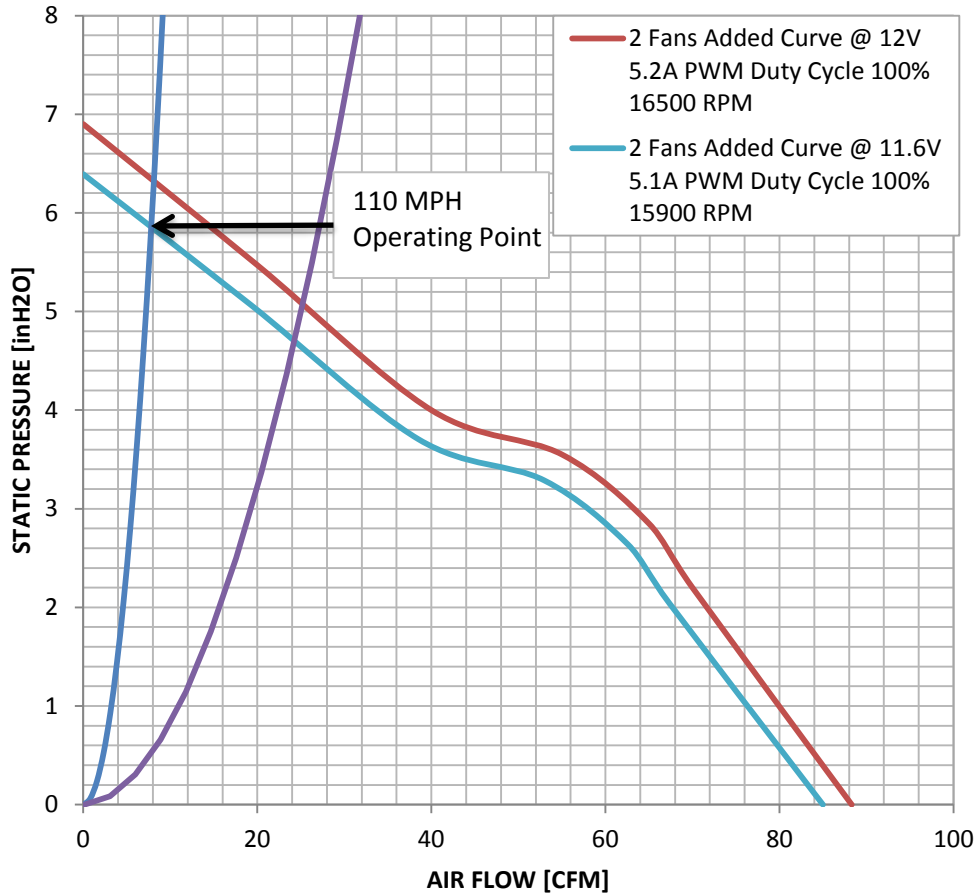
Figure 2.2 Operating Point Range Prediction

Method of Control

Pulse-width modulation (PWM) was the recommended signal input to control the fan speed. The PWM signal changes the duty cycle therefore having the same effect as a change in voltage and is most valuable when your system uses a constant voltage supply. For example, a 5 volt system operating at 50 % duty cycle would produce the same fan speed as a 2.5 volt system operating at 100 % duty cycle. However for the present application, a DC power supply with variable DC voltage was chosen as the method for power and speed control since a general-purpose laboratory DC power supply was readily available and provides simple, continuously-variable control.

Solid-Modeling, 3-D Printing and Fabrication

Concepts for the final solid-model were derived from the TSI 1128 and previous thesis work [17]. The TSI 1128 nozzle was scaled down to meet the new requirements of ducting and fan size. The hot-wire clamp arm assembly was a scaled down version from [17]. Both the nozzle and hot-wire clamp arm assembly were 3-D printed out of black ABS with use of an Eden Objet 250. The aluminum plates were designed for quick removal and replacement of the nozzle. The strut supports have six height levels and the main strut assembly can slide within the top plate to allow the probe being calibrated to be positioned within the core of the jet flow. Tight tolerance 4 mm struts were used to align all of the tubing with the fans and are secured by 4 10-32 socket head cap screws. The duct tubing is 2.75 inch ID, 3.25 inch OD acrylic. Closed cell foam is used to construct an air-tight seal between components of the calibration apparatus. Nine inch 1/4-20 socket head cap screws secure the entire duct-work and fans. 3 inch long T-Slot legs fastened to vibration-damping adjustment levelers hold up the structure. The final SolidWorks assembly can be seen in Figure 2.3.
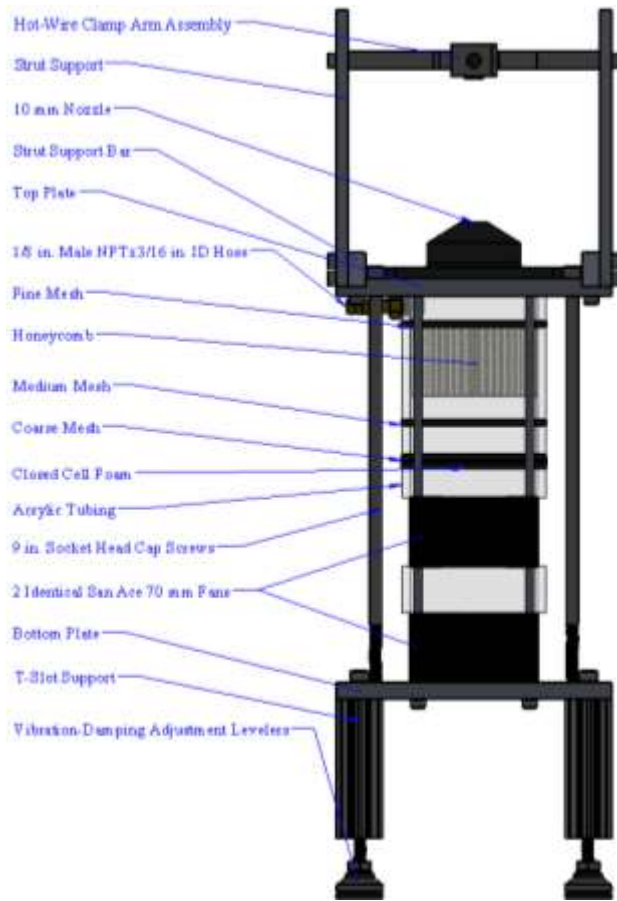
Figure 2.3 Final SolidWorks Assembly

Table 2.1 Parts List with descriptions

Part Name	Item Description
Hot-Wire Clamp Arm Assembly	Rapid Prototype Plastic
2X Strut Support	6061 Al 1/4 in. x 3/4 in.
10mm nozzle	RP Plastic Inlet to Exit Diameter Ratio: 7
2X Strut Support Bars	6061 Al 3/8 in. x 3/4 in.
Top Plate	6061 AL 3/8 in. Plate W/ Buna Cord Groove
1/8 in. Male NPT	Brass 1/8 in. Male NPT to 3/16 in ID Hose
Fine Mesh	32 SS 0.0065 in. Wire Dia. 62.7 % Open Area
Honeycomb	Aramid Fiber 90% Open Area 1/4 in. Cell
Medium Mesh	24 SS 0.0075 in. Wire Dia. 67.2% Open Area
Coarse Mesh	4x4 SS 0.054 in. Wire Dia. 62% Open Area
Closed Cell Foam	1/8 in. x 1/4 in Adhesive Neoprene Foam
5X Acrylic Tubing	2.75 in. ID x 3.25 in. OD Acrylic
9 in. Socket Head Cap Screw	1/4-20 Black Oxide Steel
2X San Ace 70 mm Fan	12V/2.6A/31.2W
T-Slot Support	6061 AL 1x1 in. 3 in. Long T-Slot
Bottom Plate	6061 AL 3/8 in. Plate
Vibration-Damping Adjustment Leveler	1/4-20 1.5 in. long Rubber Padded Adjusters

All of the parts were machined in-house by the author in the Cal Poly machine shops. Acrylic tubing was cut to length and faced on the lathe for a flat sealable surface. Holes were tapped by hand and the calibration apparatus was assembled with the utmost care. The Top Plate was the most complicated part to machine. The center hole was cut starting out at 1/8 inch and up to 1 1/32 inches. Then a fly cutter was used to cut the through hole at 2.73 inches. A 2.985 in. step was then cut at 0.150 in. vertically to make a space for an O-ring to create a seal between the plate, nozzle and tubing. Lastly, a 3.250 in. step was cut at 0.075 in. vertically to provide a close tolerance fit for the tubing. The final assembly can be seen in Figure 2.4.
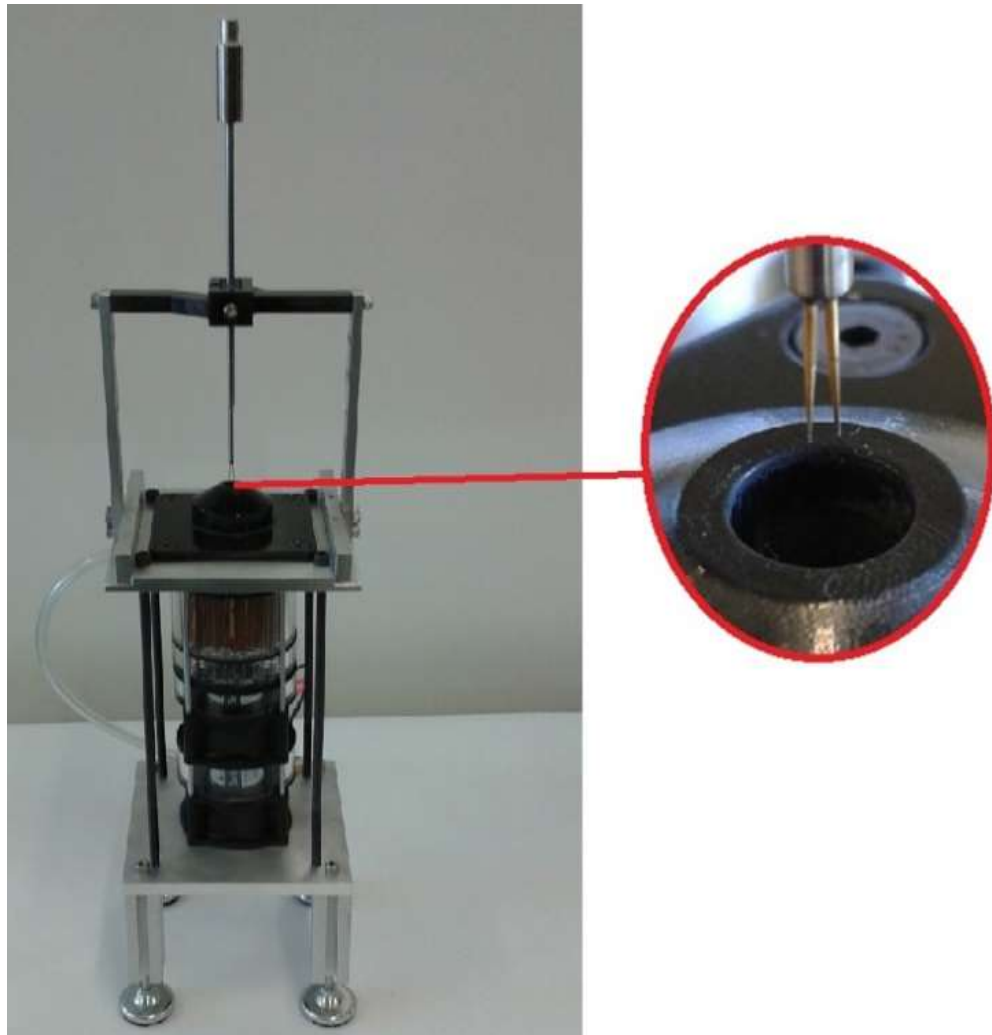
Figure 2.4 Final calibration apparatus assembly with hot-wire probe installed

Performance Validation Testing

Initial tests of the calibration apparatus were conducted to validate the estimated performance. The dynamic pressure at the nozzle exit was measured with a 0.065 inch diameter Pitot probe plumbed to a Setra 239 pressure transducer connected to a Fluke 289 DVM. An analysis of the uncertainty in Setra pressure and velocity was performed (Appendix G). The pressure measurement locations are pointed out in Figure 2.5 and the experimental set-up can be seen in Figure 2.6.
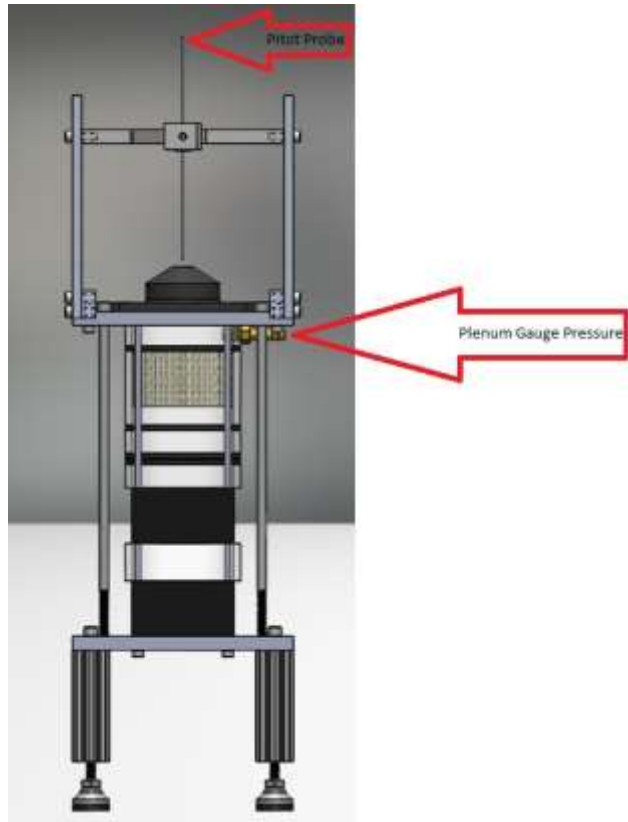
Figure 2.5 Locations for pressure measurement
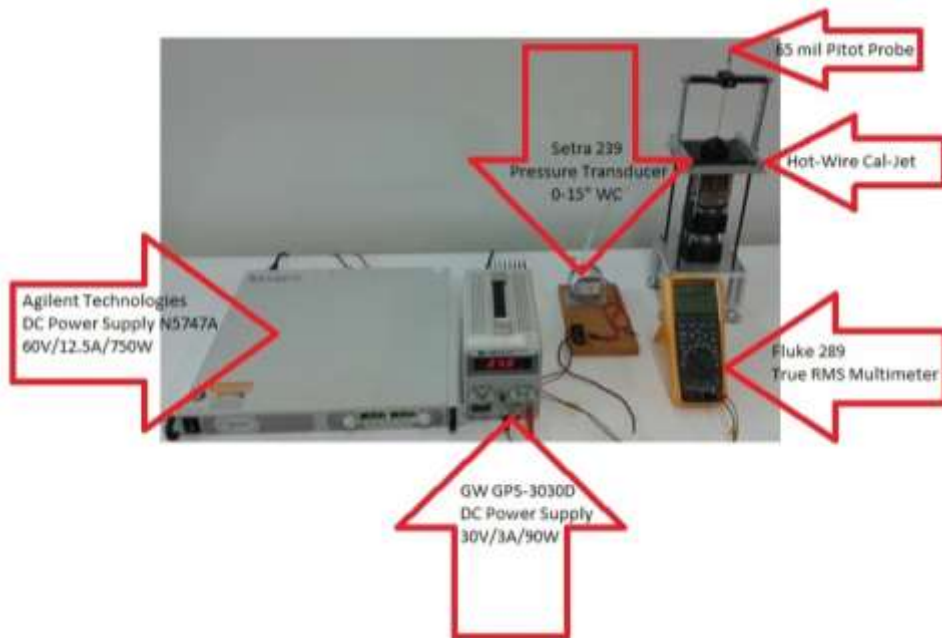
Figure 2.6 Experimental setup for performance validation and pressure coefficient, *Cp*

The calibration apparatus was tested to confirm that a nozzle flow speed of 110 MPH was achievable. A flow speed of 110 MPH corresponds to a flowrate of 7.83 CFM which produces a dynamic pressure of 6.34 inH$_2$O. Theoretically, to produce these results, the fans would require an input of 11.6 volts and 5.10 amps corresponding to a total power input of 59 watts. Additionally, the fan motors would be performing at a PWM duty cycle of 100% and 15900 RPM. The experiment involved using the DC power supply to control the total power input and using a Fluke 289 DVM to monitor fan motor speed. The power was increased until a flow speed of 110 MPH was achieved. The voltage and amperage input were recorded and a total power input of 75.2 watts was calculated. At a PWM 100% duty cycle, the fan motors reached a speed of 15100.

Table 2.2 Comparison between theoretical and experimental power input and fan speed used to achieve 110 MPH

	Theoretical	Experimental	% Difference
Total Power Input [W]	59.0	75.2	22
Fan Motor Speed [RPM]	15900	15100	-5.0

A percent difference was taken, to directly compare the theoretical power input to the experimental. As expected, the power required to achieve a flow speed of 110 MPH was underestimated. This resulted in a percent difference of 22%. Additionally, a comparison was made between the theoretical and experimental fan motor speed. This resulted in a percent difference of -5%. At first thought, it appears concerning that the results would change sign, but the theoretical values are based off of a test in a facility with unknown fluid properties and conditions. Also, these ratings correspond to the same type of fan, but not the exact fans used in this analysis. San Ace 70 data may also be based on results of multiple fans and then averaged.

Furthermore, the fans operate at the desired flow speed of 110 MPH slightly above the suggested voltage range of 10.8 to 13.2 volts; prescribed by the manufacturer. Therefore, the San Ace 70 fans are regarded as an excellent choice for the calibration jet apparatus.

Additional tests of the calibration apparatus involved solving for a pressure coefficient to relate the pressure at the nozzle to the pressure in the settling chamber plenum. The measurement ports are pointed out in Figure 2.5. The dynamic pressure q, at the nozzle was measured with the Setra 239 pressure transducer with the plenum tubing clamped. The Pitot probe was placed 5 mm above the jet exit. Then the pressure difference between the total plenum pressure and room static pressure was measured. By dividing the plenum pressure difference by the dynamic pressure, a pressure coefficient was computed (Figure 2.6). The resulting equation is as follows:

$$Cp = \frac{\Delta P_{Plenum}}{q_{nozzle}} \qquad (2.16)$$

The results of this calibration proved to be a linear curve with a Cp value of 1.00 (Figure 2.7). This Cp value will be used to accurately determine the flow speed out of the nozzle without using a Pitot-Static probe during hot-wire calibrations.

Additionally, the uncertainty determined for the use of the Setra for this study involved a RSS accuracy of $\pm$ 0.14% full scale; where full scale was 5 volts. Half of the RSS accuracy was taken, considering that the measurements involved pressure/voltage readings up to approximately half scale. This corresponds to an uncertainty of $\pm$ 0.012 inH2O. Further uncertainty analysis is detailed in Appendix G.
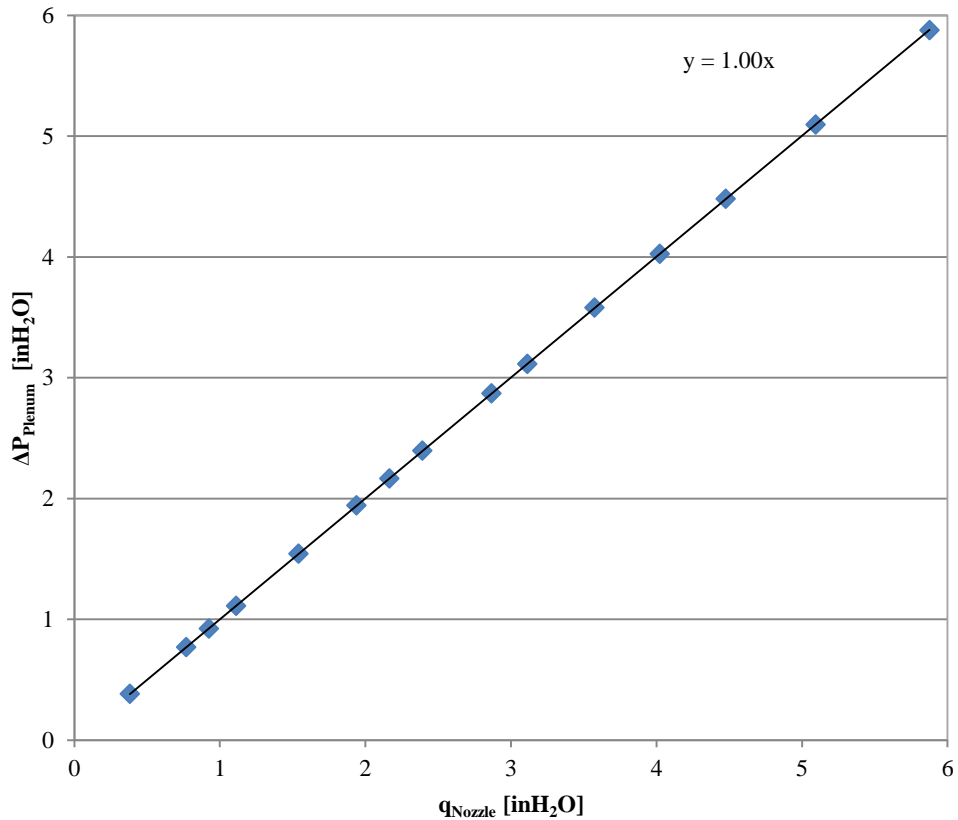
Figure 2.7 Plenum pressure difference plotted as a function of dynamic pressure

An initial test of the calibration apparatus was performed at ¼ ATM to ensure it was capable of operation inside the vacuum chamber without overheating. This test was performed by placing a thermocouple on the second fan up and recording temperature while proceeding through the desired wind speed range. This resulted in a 10.0 ^{0}C increase in fan temperature from 24.1 to 34.1^{0}C. Since the fans are rated up to 70 ^{0}C, the experimental set-up was regarded as a safe fan environment.

The increase in fan temperature will contribute some heat transfer to the free stream air. When CVA calibration is thoroughly discussed in the next chapter, it will become apparent that the calibration of a hot-wire must rely on constant static pressure and free stream temperature;

because this is the trend seen in-flight. However, this will present a temperature drift in the data which will be discussed as well in the next chapter.

The calibration apparatus has been designed to accommodate the hot-wire CVA, as well as the vacuum chamber geometric/environmental constraints. The nozzle successfully accelerates the flow to match the current Cal Poly Mechanical Engineering Department's low speed wind tunnels which can reach flow speeds up to 50 m/s. Conditioning elements selected, satisfy the condition for turbulent free flows and the San Ace 70 fans in series provide the total pressure necessary to achieve the desired flow speeds. A complicated speed controller has been replaced with the use of a general DC variable voltage power supply. In the following chapter, the calibration apparatus was used experimentally to validate the existing theoretical thermal/electrical CVA model in low to standard density flight conditions. An overview of the thermal/model is presented for reference and the test parameters are provided. An issue involving temperature variation will be explained and the experimental results will be corrected. The thermal/electrical model's Nusselt number correlation will be scaled to better predict CVA output results. Frequency response will be briefly discussed. Finally, the thermal/electrical model will be compared to corrected experimental data and calibration curves will be applied to the experimental data.

3. CVA Calibration

Overview of the Thermal/Electrical Model

To validate the thermal/electrical model, some key concepts and steps in predicting CVA behavior must be understood and will be presented briefly here [17]. The output parameters considered for CVA are either the op-amp output voltage V_s, or the CVA output I_w (measured as a voltage which is proportional to current), through the hot-wire sensor. The CVA probe wire is, essentially a voltage follower op-amp circuit. The set-point voltage of the sensor is set at a nominal value, at which it stays during testing. To compensate for this behavior, the hot-wire resistance R_w, must decrease with an increase in flow speed to maintain the set-point voltage V_w. This also means the hot-wire current I_w will increase with the increase in flow speed ($I_w = V_w/R_w$). The CVA instrument panel was designed with BNC connections which can interface with a digital voltmeter (DVM) (Figure 3.1).

Figure 3.1 CVA system built for Cal Poly BLDS [17]

29

Depending on the selection on the DVM, volts, amps or current can be measured at any connection. Both the V_o-*Out* or I_w-*Out* BNC output connections can be used for data collection. To easily measure multiple variables with limited DVMs, voltage was measured at the output connections. A basic CVA circuit diagram is shown in Figure 3.2. The hot-wire sensor characteristics are tabulated below in Table 3.1 [27].
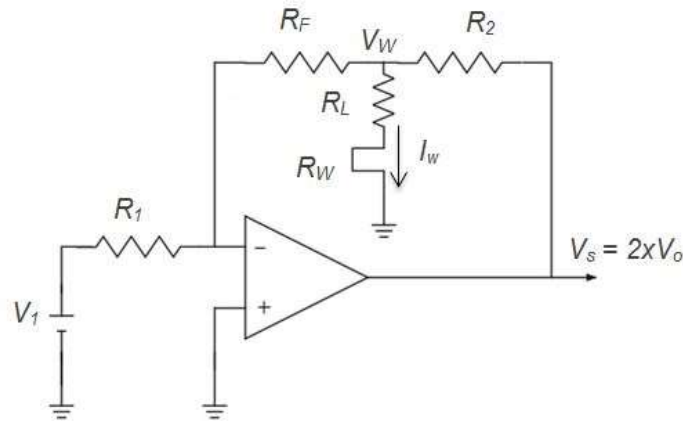
Figure 3.2 Basic CVA circuit diagram [17]

Table 3.1 Hot-wire sensor characteristics for TSI probe model 1210-T1.5 with serial number 71105221

Diameter, D [mm]	Length, L [mm]	Resistance at 25 ºC, R_∞ [Ω]	Temperature Resistance Coefficient, α_0 [$^oC^{-1}$]
0.0038	1.27	5.98	0.0042
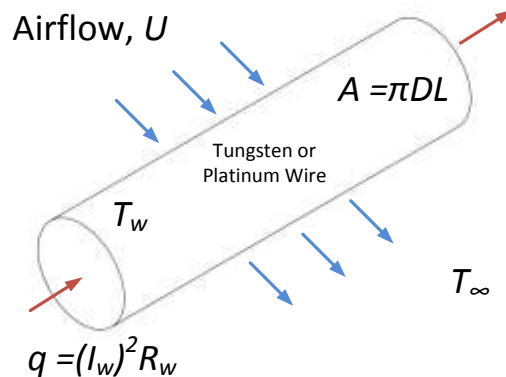
Figure 3.3 Heated cylinder in cross-flow [17]

30

Assuming instantaneous heat transfer, a simple energy balance on the hot-wire in the free stream under forced, cross-flow convection and neglecting probe-end losses as shown in Figure 3.3 [17] [28]:

$$I_w^2 R_w = \pi D L h (T_w - T_\infty). \tag{3.1}$$

Collis and Williams study [19] suggested that the correlation below could be used to obtain the heat transfer coefficient, h, for Reynolds numbers between 0.02 and 44:

$$Nu = (0.24 + 0.56 Re_D^{0.45}) \left(\frac{T_f}{T_\infty} \right)^{0.17}. \tag{3.2}$$

Using the definitions of Nu and Re, the convection coefficient h, can be expressed as

$$h = \frac{k_f}{D} \left(0.24 + 0.56 \left(\frac{\rho_f U D}{\mu_f} \right)^{0.45} \right) \left(\frac{T_f}{T_\infty} \right)^{0.17}. \tag{3.3}$$

The subscript f, denotes that the fluid properties are calculated at the film temperature:

$$T_f = \frac{T_w + T_\infty}{2}. \tag{3.4}$$

The sensor wire resistance is assumed to vary linearly with temperature [17] [29]:

$$T_w - T_\infty = \frac{R_w - R_\infty}{a_0 R_0}. \tag{3.5}$$

The temperature coefficient of resistance a_0 ($^\circ C^{-1}$) multiplied by the probe resistance at 20 $^\circ$C room temperature R_0, relates a change in temperature to a change in resistance [17]. Using Ohm's, law the final expression needed can be derived:

$$V_w = I_w (R_w + R_L). \tag{3.6}$$

With specific known values for U, T_∞, R_∞, and V_w, equations (3.1) through (3.6) can be solved simultaneously to determine the 5 unknown variables: T_w, T_f, R_w, I_w, and h [17]. The cold probe resistance R_∞, must be measured at the ambient fluid temperature T_∞, specific to the experimental environment. The V_w set-point is carefully selected by predicting the overheat ratio (OHR):

$$OHR = \frac{R_w}{R_\infty}. \tag{3.7}$$

The OHR is used to avoid burning up a hot-wire at the lowest flow speed. For this particular hot-wire probe, TSI 1210-T1.5, the recommended OHR is < 2, for an ambient fluid temperature T_∞ of approximately 25 ^{o}C [17]. More importantly, the hot-wire sensor resistance, R_w, must not exceed approximately 12 Ω or the wire temperature T_w, must not exceed approximately 237 ^{o}C. The flow velocity U, is the input, which can be varied throughout a desired range and the thermal/electrical model predicts the CVA op-amp voltage, which can be expressed as:

$$V_s = \left(1 + \frac{R_2}{R_F} + \frac{R_2}{R_w + R_L}\right) V_w. \tag{3.8}$$

The simultaneous solution of equations (3.1)-(3.6) and (Nu and Re) at specific known values for U, T_∞, R_∞, and V_w will determine these 5 unknown variables: T_w, T_f, R_w, I_w, and h. An iterative solver has been used: Engineering Equation Solver or EES [30]. EES comes with built in thermal properties, which was particularly useful because calculation of the film temperature T_f, an unknown variable, was necessary to determine the fluid properties [17]. A print out of the EES code is provided in the (Appendix C). Now that the theory behind CVA has been explained, an actual CVA system will be operated and the results will be compared to model predictions.

Test Parameters

The experimental set-up consisted of the hot-wire calibration jet apparatus, the CVA benchtop operating electronics, a vacuum chamber (described further below), a Paroscientific Digiquartz® Model 745 high accuracy pressure standard instrument, an Agilent Technologies DC power supply, a GW DC power supply, an Omega® HH23 thermocouple reader along with a k-type thermocouple, two Fluke true RMS DVMs, a Setra 239 pressure transducer and a static pressure damper (Figure 3.4). The vacuum chamber is constructed of high grade stainless steel and measures 22 inches deep with an overall diameter of 17 inches. A vacuum pump pulls the air molecules out of the system and a roughing valve is manually opened to allow the pressure to decrease in the vacuum chamber. A vacuum chamber schematic is presented in (Appendix F). The pressure was monitored using the Paroscientific Digiquartz® Model 745 high accuracy pressure standard instrument. However, the vacuum chamber did not have the capability of temperature control common to altitude chambers otherwise referred to as thermal vacuum chambers (TVAC).

To ensure that any small air drafts within the vacuum chamber did not influence the reading of its static pressure, a static pressure damper was created. The static pressure damper consisted of a plastic sealable container (i.e. coffee thermos) filled with acoustic foam, two 1/8 inch male NPTx3/16 inch barbed tube fittings and approximately two 2 feet sections of 3/16 inch tubing (Figure 3.5).
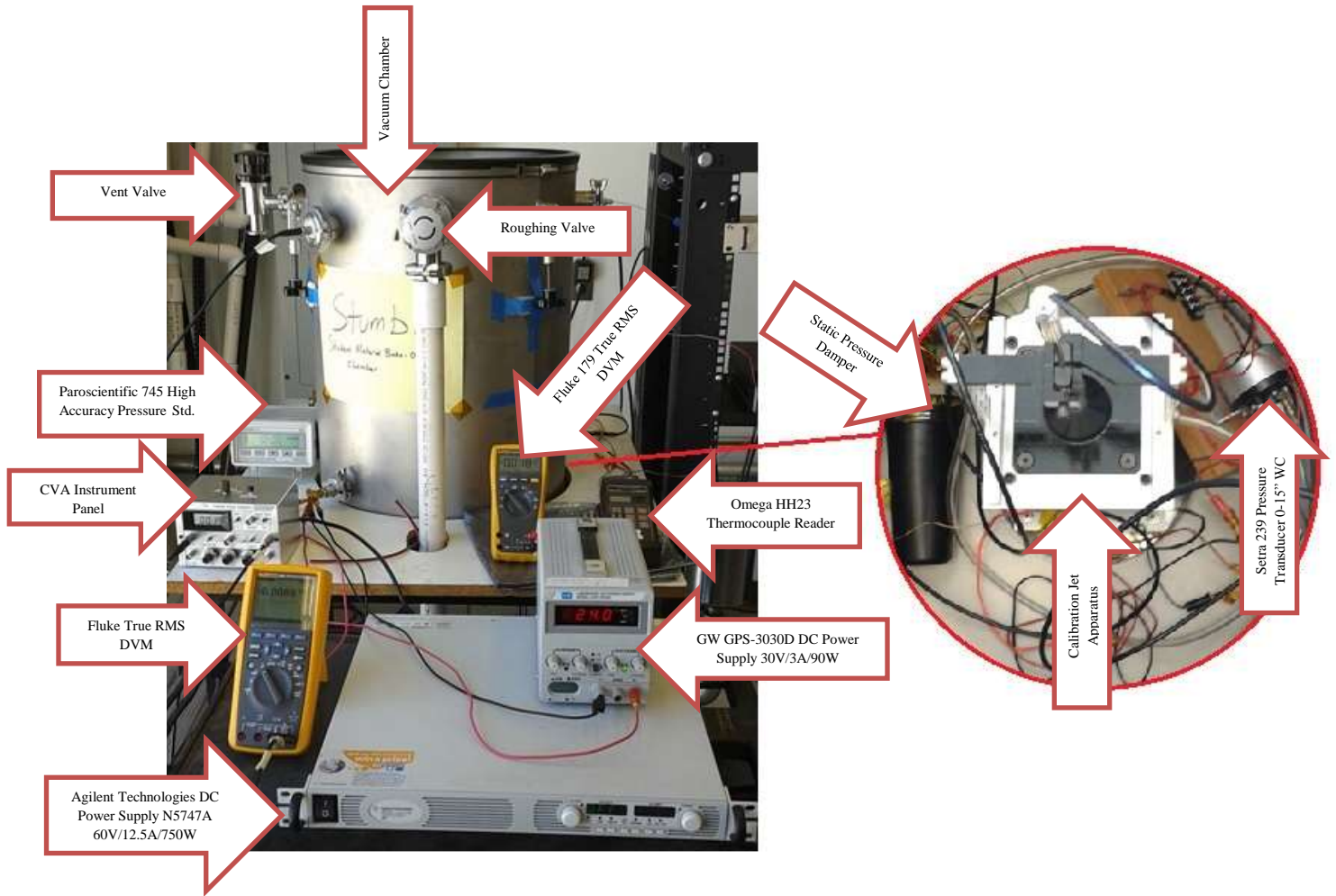
Figure 3.4 Experimental set-up with vacuum chamber (vacuum chamber schematic in Appendix F)

Figure 3.5 Static pressure damper

To minimize particulates within the vacuum chamber, the test environment as well as all test equipment was thoroughly cleaned prior to testing. The calibration apparatus, Setra pressure transducer and static pressure damper were placed inside the vacuum chamber. All of the necessary wiring and tubulation were fed through and attached to the corresponding components. The wiring was covered with Kapton tape to avoid potential arcing during testing. A continuity check was performed to ensure the correct polarity was chosen for all of the electrical feed-throughs.

Test conditions were established to validate the accuracy of the thermal/electrical CVA model at pressures of ¼, ½, ¾, and 1 ATM with flow speeds ranging from 14 to 50 m/s. The vacuum chamber used for the experiments did not have temperature control therefore the free stream temperature was recorded, by attaching a thermocouple downstream of the nozzle jet without obstructing the flow over the hot-wire. Once the vacuum chamber was at the desired pressure with a calibration apparatus flow speed of 14 m/s, the hot-wire voltage V_w, was set while measuring the operating resistance R_w, to achieve an OHR of 1.8.

Temperature Drift

Temperature drift is defined as an undesirable change in temperature that can adversely affect experimental results. A change in temperature will result in a change in hot-wire operating resistance, R_w. To correctly calibrate a hot-wire, the free stream pressure and temperature must remain constant. This will ensure that the hot-wire CVA output, I_w, is only changing due to the change in flow speed. This is important for validating predictions, since flow speed is the only parameter that is varied. Similarly, in-flight, there will be no mechanism for temperature drift, so

if we are to closely approximate flight conditions, the pressure and temperature must remain constant.

Temperature drift in the data was caused by heat transfer of the calibration apparatus fan motors to the free stream air at increasing flow velocities. The temperature drift is seen as an increase in temperature of the free stream air which causes the hot-wire CVA output, I_w, to undershoot the value it would have achieved given constant temperature. Li [21] suggested using the thermal/electrical CVA model to calculate I_w, at the actual temperature and then calculate I_w at a reference temperature, chosen at an approximate steady state seen at the lower speeds. The difference in the two calculations was then added to the experimental CVA output I_w (eq. 3.11 and 3.12).

$$\Delta I_W = \left(I_{W,Model_{Actual\,T}} - I_{W,Model_{Ref\,T}} \right) \tag{3.9}$$

$$I_{W,Corrected} = I_{W,Experimental} + \Delta I_W \tag{3.10}$$

Scaled Nusselt Number

Similarly, the Nusselt number had to be scaled to better predict hot-wire results for I_w. Previous work, as well as the current thesis, have shown that the Collis and Williams correlation [19], which is used in the thermal/electrical CVA model, under predicts the heat transfer on the wire [21] [17]. Consequently, the CVA output I_w, is also under predicted, resulting in an inaccurate calibration prediction. To correct the predictions of the CVA output I_w, the Nusselt number was scaled so that the model results matched up closely with the corrected experimental data at each corresponding pressure:

$$Nu_{SF} = SF \left[(0.24 + 0.56 Re_D^{0.45}) \left(\frac{T_f}{T_\infty} \right)^{0.17} \right]. \tag{3.11}$$

The resulting scaling factors *SF*, ranged from 1.27 to 1.34 corresponding to the pressures ranging from ¼ ATM to 1 ATM.

Scaling the model, therefore, is necessary to provide predictions that are closer to the true experimental data. However, the Nusselt number cannot be scaled at each pressure and temperature combination as this would require extensive post-processing, which goes against the objective of this thesis and previous CVA development. This would also deter the development of a single-point autonomous calibration prediction. The scaling factor *SF*, must be selected at a value that best represents all of the data. For that matter, a value of 1.3 was chosen for this particular hot-wire and will be used to scale the predictions to compare to experimental results.

Further improvements were investigated in the form of, individually, scaling the Nusselt number offset coefficient, *A*, and the Nusselt number multiplying factor, *B*. Scaling the Nusselt number by 1.3, scales both *A* and *B*. The new shift involved scaling them individually, in anticipation of the development of the single-point calibration equation which needs to be a one degree of freedom function. The improvements proved to be unsuccessful. For example, scaling *A* at ¾ ATM resulted in a better prediction, but when applied to the other pressures, the shifted curve under-shoots or over-shoots significantly. A similar trend was found when scaling *B*. Therefore, scaling the Nusselt number appears to be the best solution for the experimental CVA output data analyzed in this thesis. Future work may involve further improvements to the Nusselt number correlation to better predict CVA output. This may involve investigating radiation as an additional source of heat transfer and then adding the governing equations to the CVA thermal/electrical model.

Frequency Response and Sensitivity

Hot-wire anemometers suffer from a thermal lag due to a finite time required for the sensor temperature to reach its new value after a velocity fluctuation, and this interval is characterized by the thermal time constant. The relative amplitude of the time varying signal output from the HWA is the amplitude ratio H, the ratio of the attenuated output signal to full amplitude signal without attenuation [17]. The equation for amplitude ratio H, as stated by Hinze [29] as

$$H(\omega) = (1 + \omega^2 M^2)^{-1/2}, \tag{3.12}$$

displays how increasing frequency ω and time constant M result in a decrease in H. It is also necessary to examine the equation for the constant voltage time constant M_{CVA} derived by Comte-Bellot and Sarma in [31].

$$M_{CVA} = \frac{(1 + a_w)}{(1 + 2a_w)} \frac{\rho_w c_w D^2}{4 k_\infty} \frac{1}{A' + B' \left(\frac{\rho_\infty U D}{\mu_\infty}\right)^{1/2}}. \tag{3.13}$$

The variable a_w is the ratio of the wire's operating resistance to the cold resistance minus one.

$$a_w = \frac{R_w - R_\infty}{R_\infty} = OHR - 1 \tag{3.14}$$

Equation (3.15) exposes the influence of OHR and velocity on the M_{CVA}. The CVA time constant decreases with an increase in OHR (or a_w) due to the $(1+a_w)/(1+2a_w)$ ratio [17]. With a fixed set-point voltage V_w, an increase in velocity will cause additional heat transfer, thus reducing the OHR which will in turn increase M_{CVA}. However, the CVA time constant decreases with increasing velocity due to the $U^{1/2}$ in the denominator, making velocity the governing factor. The OHR is also a direct influence on the sensitivity as derived by Comte-Bellot [32],

$$S_u^{CVA} = \frac{1}{2}\frac{R_w - R_\infty}{R_\infty}\frac{1}{1 + 2\frac{R_w - R_\infty}{R_\infty}}\frac{B\sqrt{U}}{A + B\sqrt{U}}. \tag{3.15a}$$

Equation (3.17a & 3.17b) reveals the effect of OHR on the CVA sensitivity $S_u{}^{CVA}$. In addition, $S_u{}^{CVA}$ can be written in terms of a_w:

$$S_u^{CVA} = \frac{(1/2\,a_w)}{(1 + 2a_w)}\frac{B\sqrt{U}}{A + B\sqrt{U}}. \tag{3.15b}$$

The CVA sensitivity, a dimensionless number, decreases with a decrease in OHR (or a_w) due to the $(1/2a_w)/(1+2a_w)$ ratio. As the OHR approaches unity, the CVA sensor becomes a temperature sensor; the hot-wire will not transfer any heat and the temperature will, essentially, equilibrate to ambient. The sensitivity is tied partly to the OHR, but also to the velocity. The heat transfer law, Kings Law, tells us that the hot-wire behavior is also controlled by $Re^{1/2}$, or the square root of the velocity [33]. Therefore, the hot-wire sensor is most sensitive at low speed, and decreases with an increase in speed. This is one of the major disadvantages of CVA.

The cutoff frequency and time constant were evaluated at approximately the same OHR's using the pressures, set-point voltages and temperatures from testing in conjunction with the thermal/electrical model at two different flow speeds (30 m/s and 50 m/s). The results can be seen below in Table 3.2.

Table 3.2 Cutoff frequency comparison between the ¼ to 1 ATM pressure range at 30 and 50 m/s

OHR = 1.70 at 30 m/s, OHR = 1.63 at 50 m/s					
Pressure [ATM]	Set-Point Voltage V_w [Volts]	30 m/s M_{cva} [ms]	50 m/s M_{cva} [ms]	30 m/s cutoff Freq. [kHz]	50 m/s cutoff Freq. [kHz]
¼	0.525	0.196	0.171	1.41	1.62
½	0.590	0.155	0.134	1.78	2.07
¾	0.635	0.134	0.115	2.05	2.40
1	0.666	0.121	0.104	2.27	2.66

The behavior of the frequency response is consistent with Neumeister's [17] predictions, whereas pressure is decreased from 1 to ¼ ATM (i.e. simulating increased altitude), the frequency response is substantially decreased. Thus, the time constant M_{CVA}, will increase with an increase in altitude. The CVA time constant will decrease with an increase in velocity, which also provides enough cooling so that during flight, the engineer can increase the V_w set-point (increasing the OHR). However, flight altitude is not completely modeled here; the flow temperature at altitude is much lower than at sea level, which will be discussed further in Chapter 5, as predictions for CVA operation at flight altitude and speeds will be analyzed.

Prediction to Experimental Comparison

The first experiment was conducted at a chamber pressure of ¼ ATM (190 + 0.5 Torr). The heat transfer convection coefficient, *h*, was decreased due to the decreased density in the ¼ ATM environment. This means the decreased density, decreases the amount that heat energy is able to be convected from the hot-wire sensor to the free stream air, resulting in increased wire temperatures. To ensure that the hot-wire was at a safe OHR, a probe wire voltage set-point V_w, of 0.5250 volts was chosen with the flow speed set at 14 m/s. This produced an OHR of 1.81, which was close to the desired value of 1.80. The corrected experimental values are presented as data points in the graph Figure 3.6. The thermal/electrical CVA model prediction significantly undershoots the actual data. The model was then altered by scaling the Nusselt number by a value of 1.3, which proves to be a closer prediction, but only intersects one data point. At low flow speed, the shifted curve is low in voltage and at high speed; the curve is at voltages much higher than those observed during the experiment. At higher flow speeds, the sensor sensitivity decreases faster than predicted.

An error uncertainty analysis was performed on the experimental data. Error bars corresponding to the uncertainty were added to the experimental data at all four pressures ¼ ATM to 1 ATM. The error bars can be seen in the following figures and the uncertainty analysis is presented in detail in Appendix G.
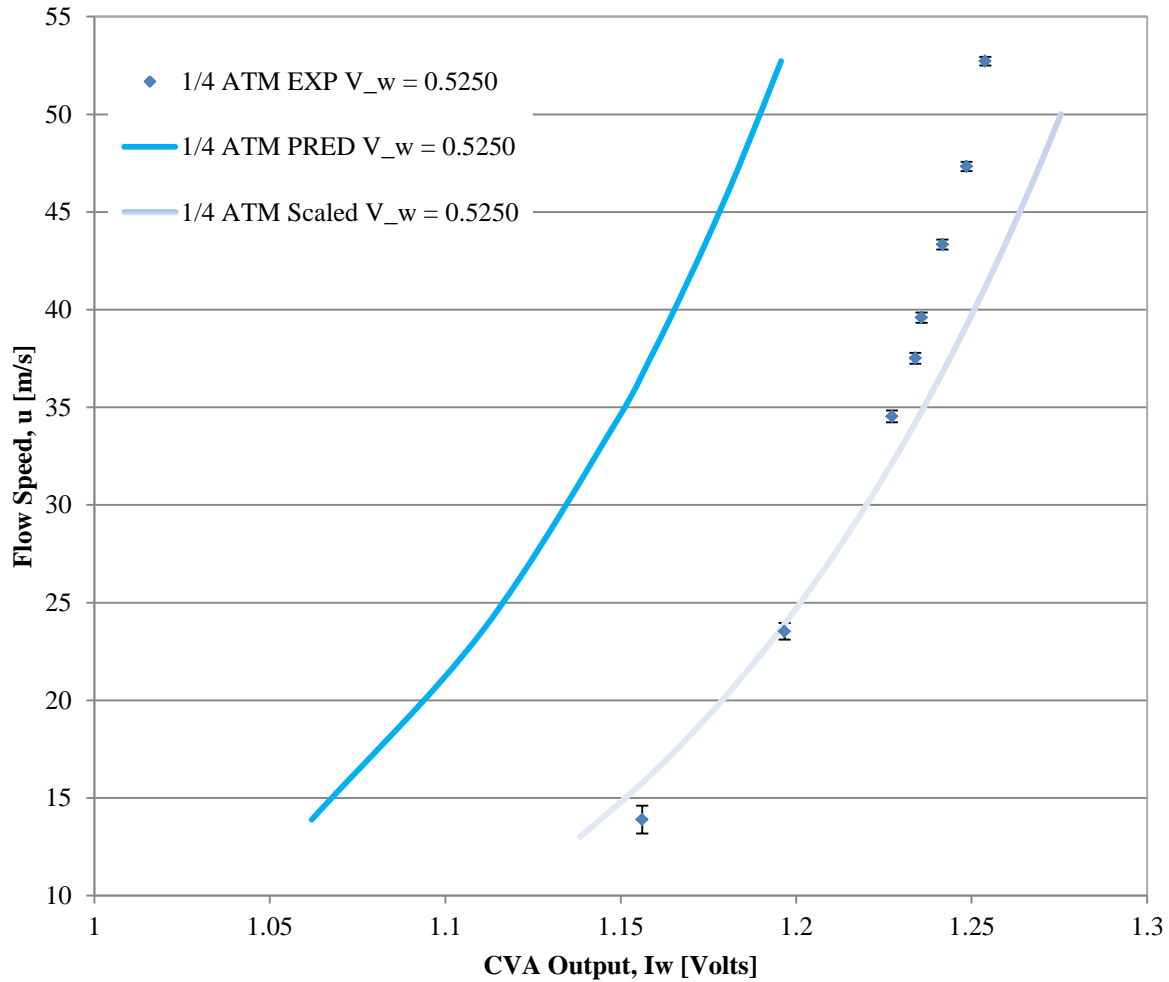
Figure 3.6 ¼ ATM: corrected experimental calibration data with error bars, predicted calibration curve and scaled Nusselt Number curve by 1.3

The next experiment was conducted at ½ ATM (380 Torr). A safe sensor operating voltage set-point V_w, of 0.5904 volts was chosen, which produced an OHR of 1.81 at 14 m/s. The

results are presented in Figure 3.7. As expected, the thermal/electrical model under-predicts the actual data. Once again, the Nusselt number was scaled by 1.3 in order to attempt an improvement in the model prediction. This resulted in a better curve than the ¼ ATM curve fit and a closer fit to the actual data that intersects approximately 3 data points. Similar to the ¼ ATM plot, at low flow speeds, the CVA output voltage is low and overshoots near flow speeds beyond 40 m/s. The behavior of the ½ ATM scaled curve is consistent with the previous ¼ ATM curve, which suggests that there may be a better solution to shift the curve to capture the data.
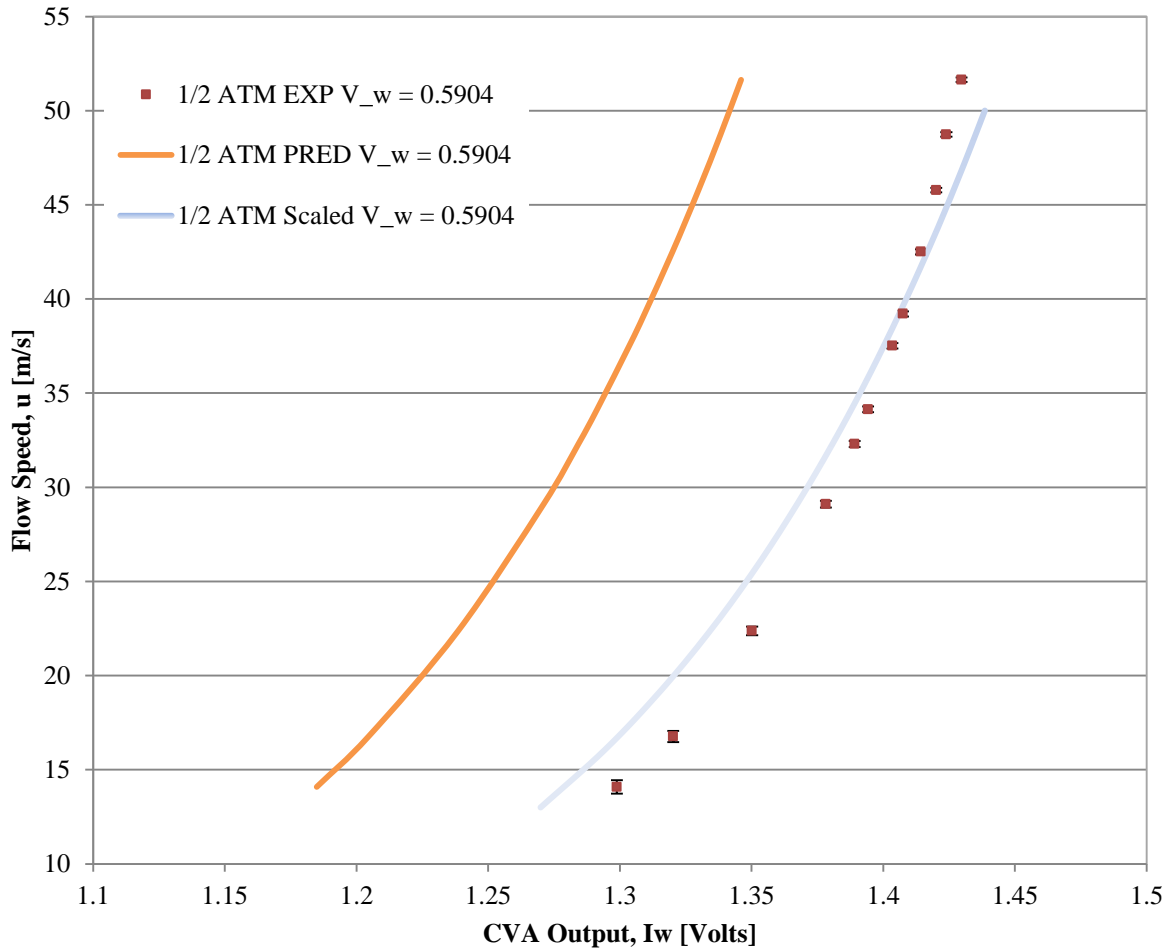
Figure 3.7 ½ ATM: corrected experimental calibration data with error bars, predicted calibration curve and scaled Nusselt Number curve by 1.3

The subsequent experiment was conducted at ¾ ATM (570 Torr). A safe probe wire voltage set-point V_w, of 0.6350 volts was chosen, which produced an OHR of 1.81 at 14 m/s. The results are presented in Figure 3.8 where the Nusselt number was scaled by 1.3. At low flow speed, the shifted curve under-predicts the CVA output voltage and at high speed; the curve is at voltages slightly higher than those observed during the experiment. The pattern is similar to the previous predictions at ¼ and ½ ATM, but at low flow speed the scaled Nusselt number curve is deviating at a greater amount, while at high speed it deviates less.

Figure 3.8 ¾ ATM: corrected experimental calibration data with error bars, predicted calibration curve and scaled Nusselt Number curve by 1.3

The final experiment was conducted at 1 ATM (760 Torr). A safe sensor operating voltage set-point V_w, of 0.6659 volts was chosen, which produced an OHR of 1.81 at 14 m/s. The results can be seen in (Figure 3.9). As stated previously, the thermal/electrical model under-predicts the actual data. To be consistent with ¼ to ¾ ATM curve, the Nusselt number was scaled by 1.3. The scaled model prediction passes through two data points, respectively. Similar to the ¾ ATM scaled curve, the 1 ATM curve under-predicts the CVA output voltage at low flow speeds and deviates at a greater amount than the ¼ and ½ ATM curves. At the highest flow speed, the scaled curve begins to over-predict the CVA output voltage.

Figure 3.9 1 ATM: corrected experimental calibration data with error bars, predicted calibration curve and scaled Nusselt Number curve by 1.3
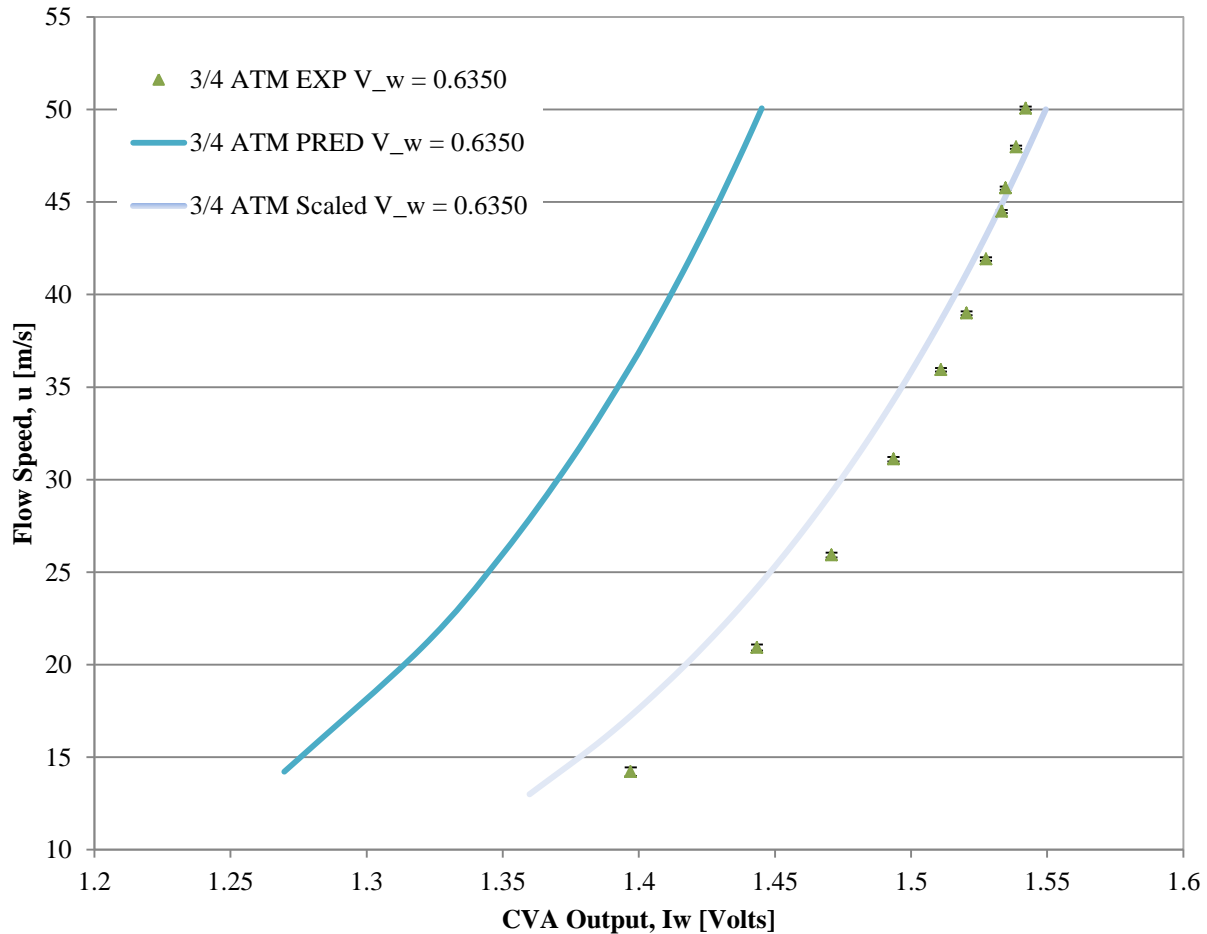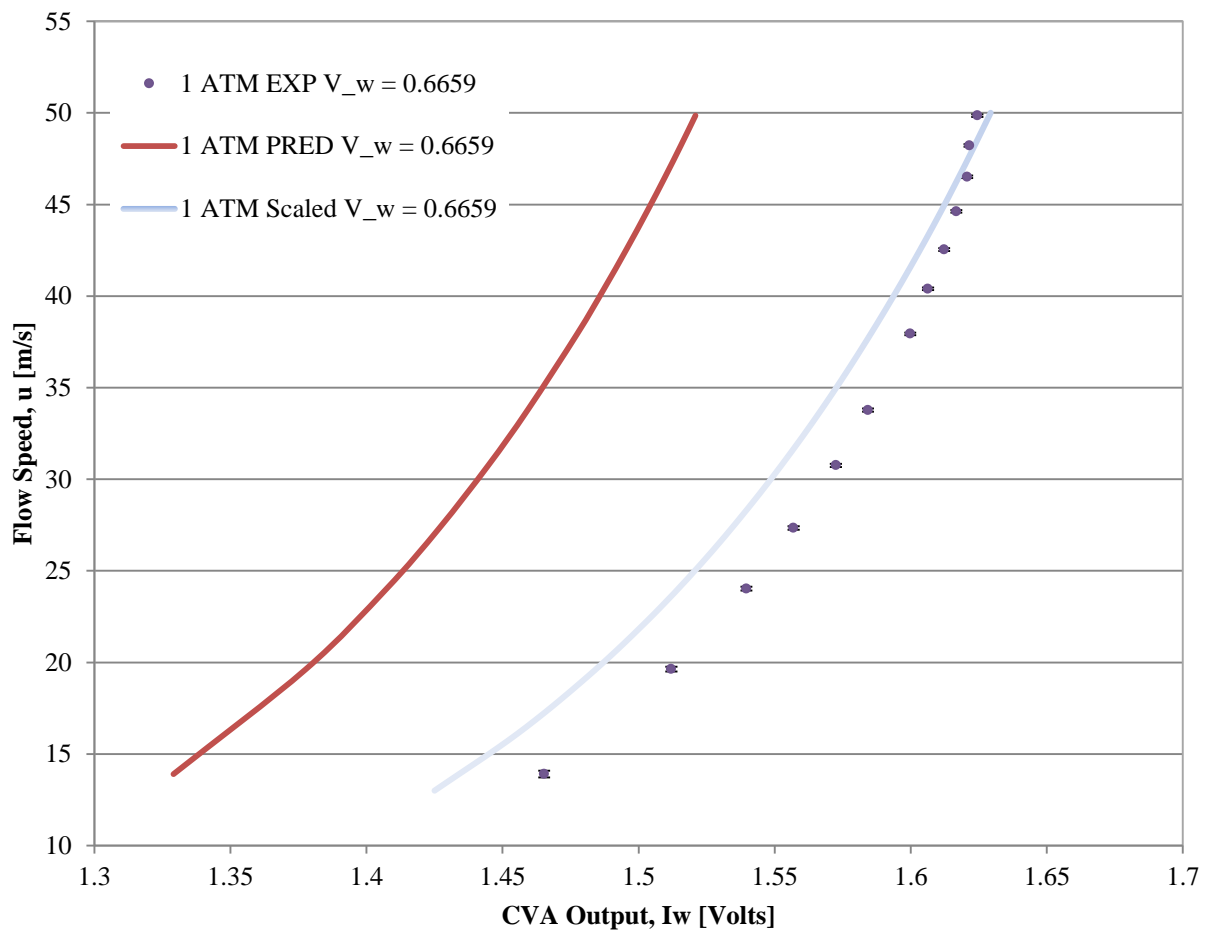
Calibration Curves

The experimental flow speed *U*, was plotted in MATLAB as a function of the CVA output I_w, at each corresponding pressure. A power-law fit is used to fit the calibration data since the heat transfer law that governs the hot-wire is in the form of a power law. Additionally, the power-law fit allows for extrapolation outside of the velocity range for which the data was taken [21]. Furthermore, the power law has been seen as a good representation of the CVA calibrations in past work [21] [17]. The power-law curve fit is in the form,

$$U = P + QI_w{}^K. \tag{3.16}$$

MATLAB's *LSQCurvefit* was then used to find each calibration curve. The power exponent *k*, was initially selected by MATLAB, and then preselected based on a value that would result in a good visual fit for all curves. The exponent chosen for this particular data-set was 16. The power-law offset coefficient *P*, and the power-law multiplying factor *Q*, were chosen separately by MATLAB for each curve. The *P* and *Q* values are presented in Table 3.3. Calibration curves for the pressure range, ¼ to 1 ATM, are presented with the experimental data in Figure 3.10.

Table 3.3 Power-law curve fit constants for ¼ to 1 ATM

Vw [Volts]	Pressure [ATM]	P	Q	K
0.525	0.25	-1.2	1.4	16
0.590	0.50	3.1	0.16	16
0.635	0.75	5.2	0.04	16
0.666	1.0	5.6	0.02	16
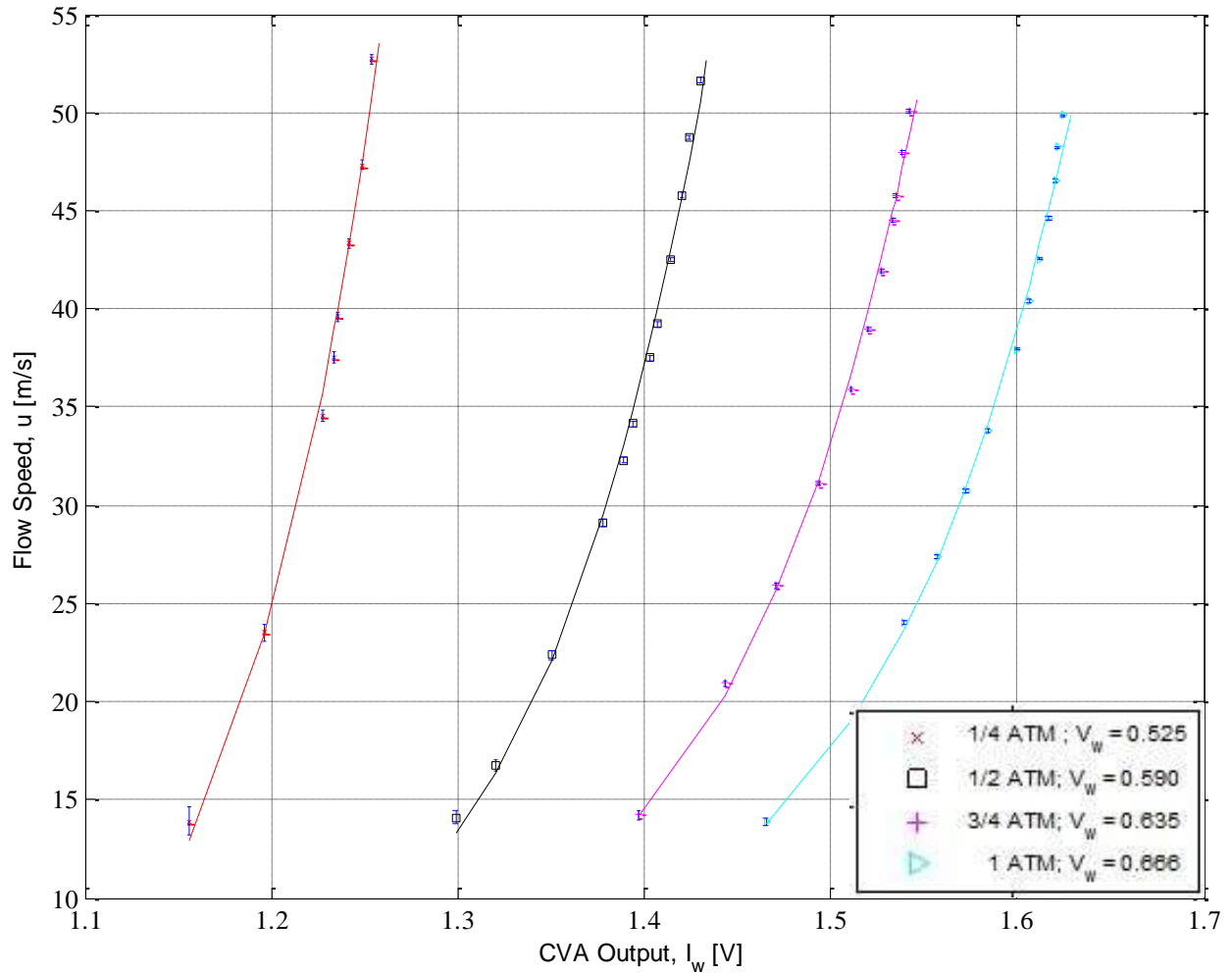
Figure 3.10 Calibration data with error bars and power-law curve fits from ¼ to 1 ATM

To further evaluate the goodness of fit for the power-law curve fit, the mean square error was calculated:

$$MSE = \frac{1}{N}\sum\left(y_{fit} - y_{meas}\right)^2 \qquad (3.17)$$

Table 3.4 MSE of the power-law calibration curve fit produced by MATLAB

Pressure [ATM]	¼	½	¾	1
Set-Point Voltage V_w [Volts]	0.525	0.590	0.635	0.666
MSE [$\frac{m^2}{s^2}$]	1.06	0.513	0.447	0.562

The lowest MSE occurred at ¾ ATM with a value of 0.447 $\frac{m^2}{s^2}$ corresponding to a percent error of 1.9% at a flow speed of 36 m/s. The uncertainty in the velocity measurement at 36 m/s and ¾ ATM was calculated at $\pm$ 0.1 m/s. The highest MSE occurred at ¼ ATM with a value of 1.06 $\frac{m^2}{s^2}$ corresponding to a percent error of 2.6% at 39.6 m/s. The uncertainty in the velocity measurements at ¼ ATM were the largest seen within the pressure range analyzed. At ¼ ATM with a flow speed of 39.6 m/s, an uncertainty of $\pm$ 0.2 m/s was calculated. The uncertainty analysis is presented briefly in Appendix G.

The CVA thermal/electrical model has been validated as a valuable prediction tool for conditions involving decreased pressure (hence decreased air density). This includes pressures ranging from ¼ ATM to 1 ATM. Although pressures below ¼ ATM were not tested in this work, it seems safe to assume that the model can be validated for lower pressures. The problem involving temperature drift has been solved by using the thermal/electrical model to calculate the change in CVA output voltage with respect to the change in temperature. Additionally, the model has been proven to under-predict the actual data in multiple scenarios (standard sea level, increased temperatures and decreased pressures) [21] [17]. Improvements to the thermal/electrical model have been attempted in the form of a scaled Nusselt number equation. Scaling the Nusselt number resulted in a similar trend at all four pressures (¼ to 1 ATM); where the scaled curves under-predict near the lowest flow speeds and over-shoot the highest flow speeds.

The P and Q variables will be used to develop a single-point autonomous calibration. Autonomous calibration is crucial for the development of a hot-wire CVA system to be used with the BLDS for in-flight conditions. Currently, BLDS is autonomous and must be kept that way to achieve its objectives without interruption of standard flight procedures. Chapter 4 will proceed with a step-by-step development of a proposed autonomous single-point calibration which will then be applied to the experimental data. This application will simulate the calibration as if it was programmed into a microcontroller to process the data.

4. Single-Point Autonomous Calibration

Autonomous Calibration Equation Development

As stated previously, in the introduction, calibrating an anemometer in-flight is a very challenging proposition. One proposed solution would involve calibrating the hot-wire on the ground within a flight simulated laboratory condition. However, replicating flight speeds, pressures and temperatures in a laboratory setting may be more problematic and costly than calibrating the hot-wire in flight. To ensure that CVA is flight ready and satisfies BLDS requirements, an innovative solution must be established. The solution proposed by Li [21], involves the development of a single degree of freedom equation. This requires fixing the power law calibration function exponent k, as a constant and correlating power-law offset coefficient P, to the power-law multiplying factor Q [21]. This approach would result in just a single degree of freedom for the calibration law, so that only one calibration data point is needed. This single-point calibration could be accomplished by measurement of velocity outside of the boundary layer with a Pitot tube, as explained below.

The process involves measuring the flow velocity with a Pitot tube next to the hot-wire in the free stream. The hot-wire voltage V_w is, then set to ensure a safe OHR while conscientiously considering the sensitivity necessary for good results. At this free stream condition, the velocity U, and the CVA output I_w, are known. As long as altitude (hence temperature and pressure) and V_w stay constant at this point, the velocity and output current voltage corresponding to any other point in the boundary layer can be predicted. Substituting the free stream velocity U_∞, and free stream CVA output $I_{w,\infty}$, into the power law calibration function, equation (3.16) becomes:

$$U_\infty = P + QI_{w,\infty}{}^K,$$

(4.1)

which provides the second equation to allow for the solution of a second unknown. Li [21] found that if k is fixed, P and Q can be approximately linearly related for special circumstances which are presented in Table 4.1. The linear relationship is presented in Figure 4.1 [21].

Table 4.1 Conditions used to test the autonomous calibration method from Li [21]

	V_w [V]	Pressure [kPa]	Temperature [℃]
Sea Level	0.65	101	20
60,000 feet	0.38	7.17	-56.5
0℃	0.62	101	0
40℃	0.65	101	40
40 kPa	0.55	40	20
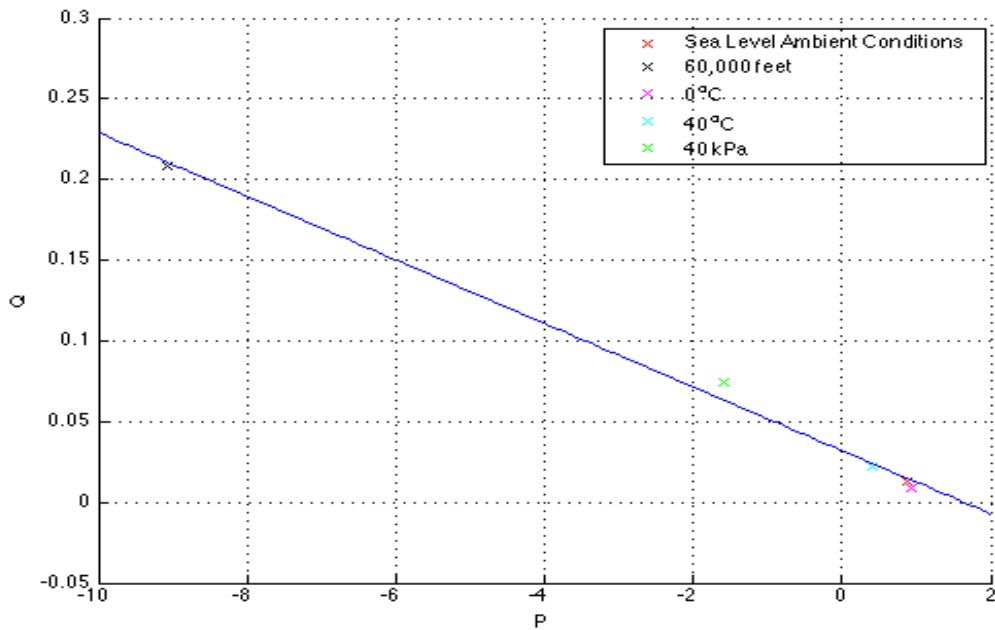
Figure 4.1 Relationship between constants P and Q from the power law for various ambient conditions [21]

With experimental data or analytical predictions, Q can be found as a function of P, using MATLAB's *polyfit* function, where m is the slope and Q_o is the Q intercept.

50

$$Q = mP + Q_o \tag{4.2}$$

Using equations (4.1) and (4.2) to solve for P yields:

$$P = \frac{U_\infty - Q_o I_{w,\infty}{}^K}{1 + m I_{w,\infty}{}^K} \tag{4.3}$$

Substituting (4.2) and (4.3) into equation (3.18) provides the autonomous single-point calibration equation (4.4) [21]:

$$u = \frac{U_\infty - Q_o I_{w,\infty}{}^K}{1 + m I_{w,\infty}{}^K} + \left[Q_o + m \left(\frac{U_\infty - Q_o I_{w,\infty}{}^K}{1 + m I_{w,\infty}{}^K} \right) \right] I_w{}^K \tag{4.4}$$

Single-Point Calibration Applied to Experimental Results

Using the experimental calibration equations developed in the previous chapter in conjunction with MATLAB's *polyfit* function, the power-law multiplying factor Q, was found as a function of the power-law offset coefficient P (Figure 4.2). The plot was then used to find constants m and Q_o, corresponding to the experimental data and substituted into (4.2):

$$Q = -0.204P + 1.05. \tag{4.5}$$

The linear trendline does not seem to be a good visual fit (Figure 4.2). Additionally, it looks as though a 2$^{\text{nd}}$ order polynomial trendline would be more appropriate, but BLDS software can only compute simple mathematical functions. However the in-flight calibration method does not necessarily have to be implemented in BLDS itself; it could be done on the ground in a spreadsheet. The mean square error (MSE), for the curve fit is $0.0223 \left(\frac{m/s}{V^{16}} \right)^2$, which corresponds to a percent error of 96% in the worst case, indicating a crude fit. Conversely, looking at the *P/Q* fit

does not directly indicate the quality of the calibration fit since it is simply an intermediate step. A more thorough quality of fit will involve assessing the accuracy of the autonomous single-point calibration applied to the experimental data.
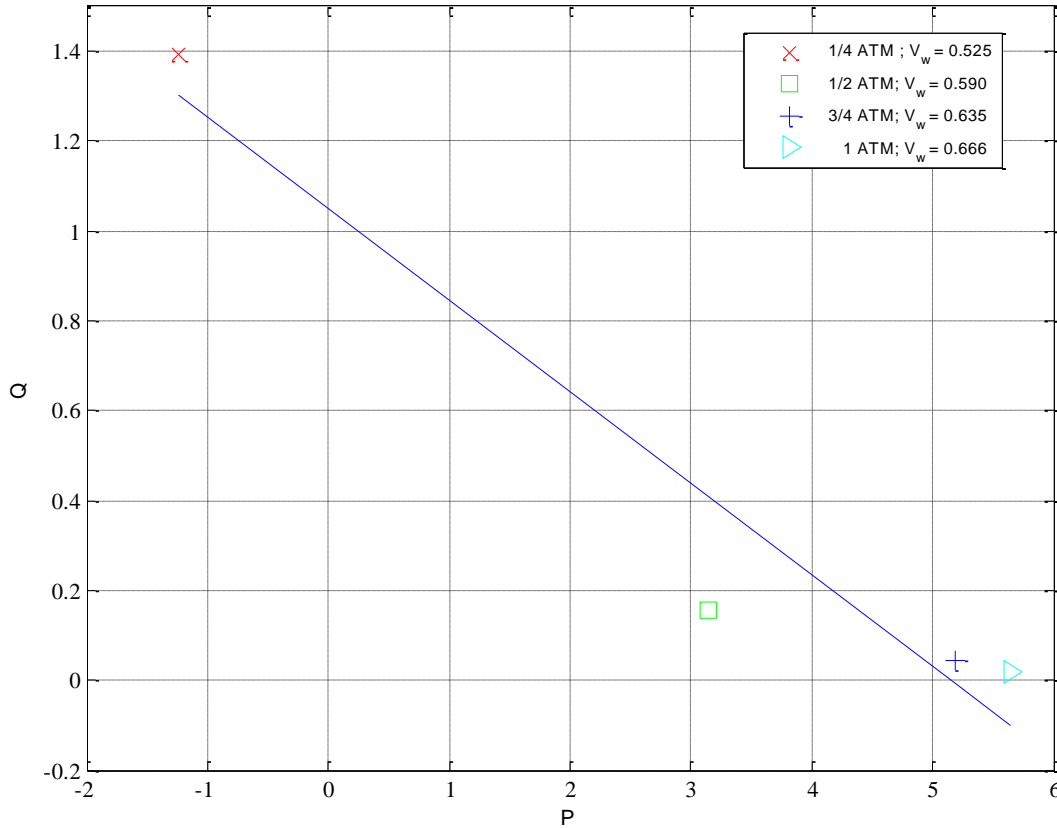
Figure 4.2 *P* and *Q* from the power-law calibration curve fits

The experimental data from Chapter 3 was used to develop the single-point autonomous calibration equation. *P* was found using equation (4.3), where constants *m* and Q_o were substituted from equation (4.5). Then one calibration point (the free stream flow speed, U_∞, and the free stream CVA output $I_{w,\infty}$), from each corresponding pressure (¼ to 1 ATM) was

substituted into (4.3) to develop equations (4.6)-(4.9). The experimental free stream conditions and constants used to solve for P, are tabulated below.

Table 4.2 Free stream conditions at each corresponding pressure used to solve for power-law offset coefficient P

Pressure [ATM]	Temperature [°C]	Set-Point Voltage V_w [Volts]	U_∞ [m/s]	$I_{w,\infty}$ [m/s]
¼	25.2	0.525	52.7	1.25
½	25.1	0.590	51.6	1.43
¾	25.1	0.635	50.1	1.54
1	24.2	0.666	49.9	1.62

¼
ATM:
$$u = \frac{52.7 - 1.05(1.25)^{16}}{1 - 0.204(1.25)^{16}} + \left[1.05 - 0.204\left(\frac{52.7 - 1.05(1.25)^{16}}{1 - 0.204(1.25)^{16}}\right)\right] I_w^{16} \quad (4.6)$$

½
ATM:
$$u = \frac{51.6 - 1.05(1.43)^{16}}{1 - 0.204(1.43)^{16}} + \left[1.05 - 0.204\left(\frac{51.6 - 1.05(1.43)^{16}}{1 - 0.204(1.423)^{16}}\right)\right] I_w^{16} \quad (4.7)$$

¾
ATM:
$$u = \frac{50.1 - 1.05(1.54)^{16}}{1 - 0.204(1.54)^{16}} + \left[1.05 - 0.204\left(\frac{50.1 - 1.05(1.54)^{16}}{1 - 0.204(1.54)^{16}}\right)\right] I_w^{16} \quad (4.8)$$

1
ATM:
$$u = \frac{49.9 - 1.05(1.62)^{16}}{1 - 0.204(1.62)^{16}} + \left[1.05 - 0.204\left(\frac{49.9 - 1.05(1.62)^{16}}{1 - 0.204(1.62)^{16}}\right)\right] I_w^{16}. \quad (4.9)$$

The functions were then plotted against the corrected experimental data (Figure 4.3). The experimental CVA output, I_w, was the only input to the autonomous single-point calibration functions. During flight, I_w will be the only variable input from the hot-wire to BLDS. Therefore, this study is a simplified simulation of a calibration during flight. The results are presented below

in Figure 4.3. The mid-range velocities tend to deviate the most from the actual data, however, the calibration appears to be a good approximate visual fit.
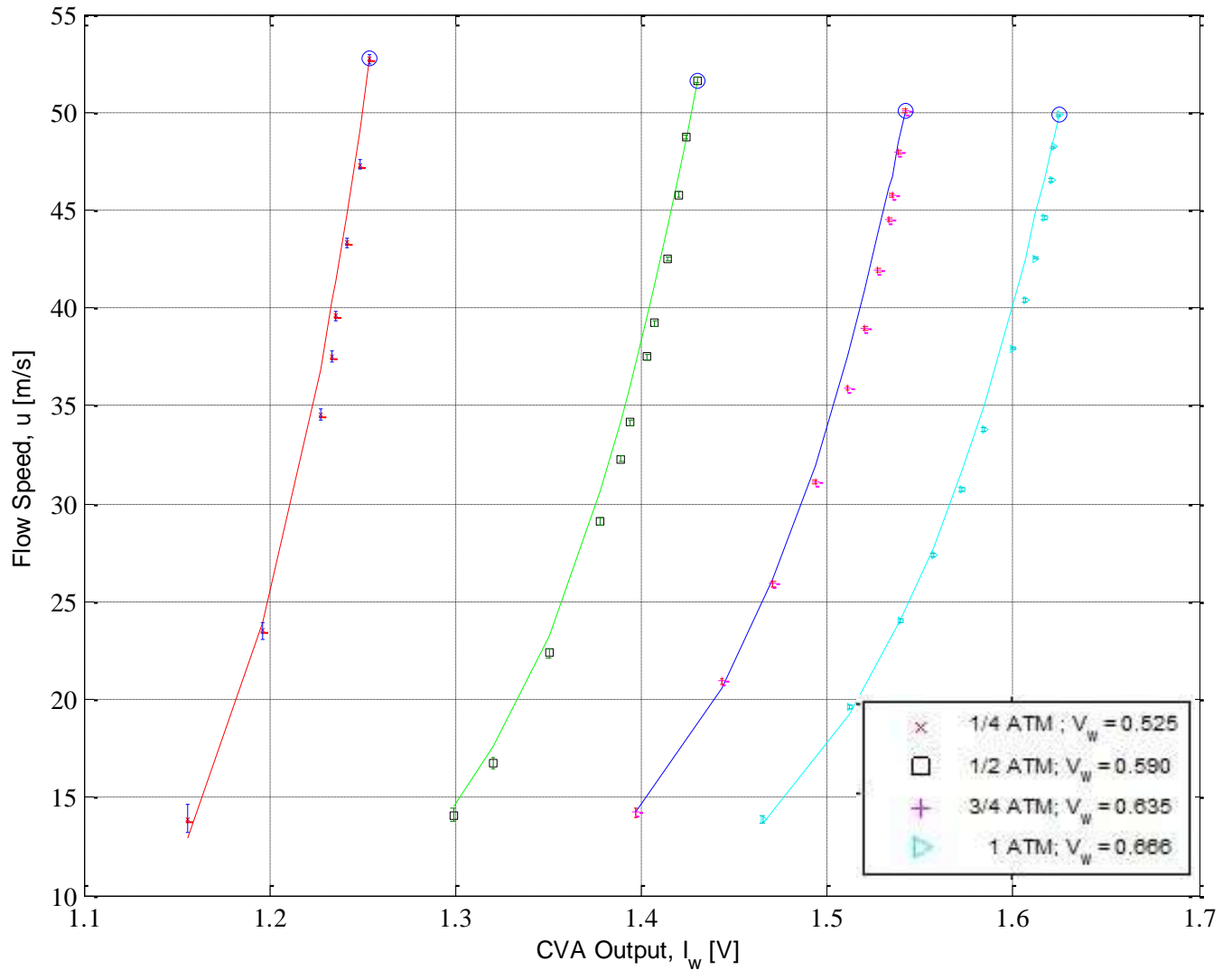
Figure 4.3 Calibration data as symbols with error bars and autonomous single-point calibration curve fits as solid lines from 1/4 to 1 ATM; single-point taken as the maximum speed at each pressure, denoted by circles

Table 4.3 MSE of the autonomous single-point calibration function at each pressure

Pressure [ATM]	¼	½	¾	1
Set-Point Voltage V_w [Volts]	0.525	0.590	0.635	0.666
MSE [$\frac{m^2}{s^2}$]	2.86	1.87	1.29	1.83

The MSE is used here to determine the goodness of the fit of the flow speed computed from the autonomous single-point calibration function compared to the flow speed from the experimental data. The lowest MSE occurs at ¾ ATM, with a value of 1.293 $\frac{m^2}{s^2}$, corresponding to a percent error of 3.6%, at a flow speed 32 m/s. This is consistent with the *P* and *Q* fit from Figure 4.2, where the linear curve fit most closely approaches ¾ ATM. The highest MSE occurs at ¼ ATM with a value of 2.863 $\frac{m^2}{s^2}$, corresponding to a percent error of 5.3% at a flow speed of 32 m/s. A percent error of 5.3% is still considered a safe error; bearing in mind the uncertainties involved with the measurements [see Appendix G]. Although the MSE is higher for the low ambient pressure conditions, this should not be a problem for in-flight conditions.

The autonomous single-point calibration function has been thoroughly derived and the process by which the calibration will be achieved has been laid out. Although, the relationship between the calibration variables *P* and *Q* tends to represent a weak linear regression trendline, the resulting calibration function proves to be a good fit. The autonomous single-point calibration has been evaluated with the experimental data produced from the tests with four different pressures developed inside the vacuum chamber.

The next step to evaluating the single-point calibration approach for possible application to CVA in flight will involve developing some simulated in-flight conditions. The thermal/electrical model developed by Neumeister [17] will be used to predict the simulated data at the specified flight conditions. Initially, the influence of low ambient temperatures and pressures at high altitude will be briefly overviewed. Then a set of conditions will be developed at five different pressures all at the same constant temperature. Each pressure condition will involve the same range of flight speeds from 40 to 150 m/s. Power-law calibrations will be applied to the simulated, variable pressure/constant temperature, data set. Then one pressure will

be selected where a single-point calibration can be applied at three different temperatures (one temperature is constant from the developed data set). This will allow for the analysis of a shift in temperature, a phenomenon common to high altitude flights. The second set of conditions will be developed at 5 altitudes; using published pressures and temperatures from U.S. Standard Atmosphere [34]. Power-law calibration curves will be applied to the simulated altitude conditions. Then one altitude will be selected where a single-point calibration can be applied at three different temperatures (one temperature from published data). This will allow for the analysis of a single-point calibration function based on published data, as well as the effect of off-standard temperatures. The frequency response at altitude will also be analyzed.

5. Predicted CVA Operation in Flight

Influence of Low Ambient Temperature and Pressure

It is well understood that flight conditions are significantly different than standard laboratory conditions near sea level. As an aircraft increases in altitude, the ambient air pressure and temperature will decrease. Taking a close look at the ideal gas law suggests that the density will increase with a decrease in temperature, at constant pressure, but will decrease with a decrease in pressure, at constant temperature. Since the change in pressure is of a larger magnitude than the change in temperature, the pressure dictates a decrease in density at altitude. This, in turn, decreases the heat transfer convection coefficient, h, significantly, which decreases the amount of heat energy that is able to be convected from the hot-wire sensor to the free stream air. For example, the heat transfer convection coefficient at standard sea level conditions, and a flow speed of 40 m/s, is 17.7 $\frac{kW}{m^2K}$, while for standard conditions at 18 kilometers, and 40 m/s, the heat transfer convection coefficient is 7.42 $\frac{kW}{m^2K}$ [34]. This roughly corresponds to a 2 to 3 % decrease in heat transfer convection coefficient per altitude rise, measured in kilometers. While the heat transfer convection coefficient at sea level at 40 m/s seems very high, the extremely small diameter size of the wire dictates the magnitude of heat transfer.

To better illustrate the influence of low ambient temperature and pressure, the heat transfer convection coefficient was calculated as a function of altitude from sea level to 18 kilometers, at flow speeds of 40, 100 and 150 m/s. The set-point voltage, V_w, was selected at each altitude to produce a safe hot-wire sensor operating resistance, R_w, equal to 12 Ω at 40 m/s. The bar graph presented in Figure 5.1, shows the heat transfer convection coefficient, h, decreasing with an increase in altitude. Additionally, h is a function of air speed, relative to the

wire, and is presented at each altitude to display this relationship. A rise in wind speed at each altitude produces an increase in h.
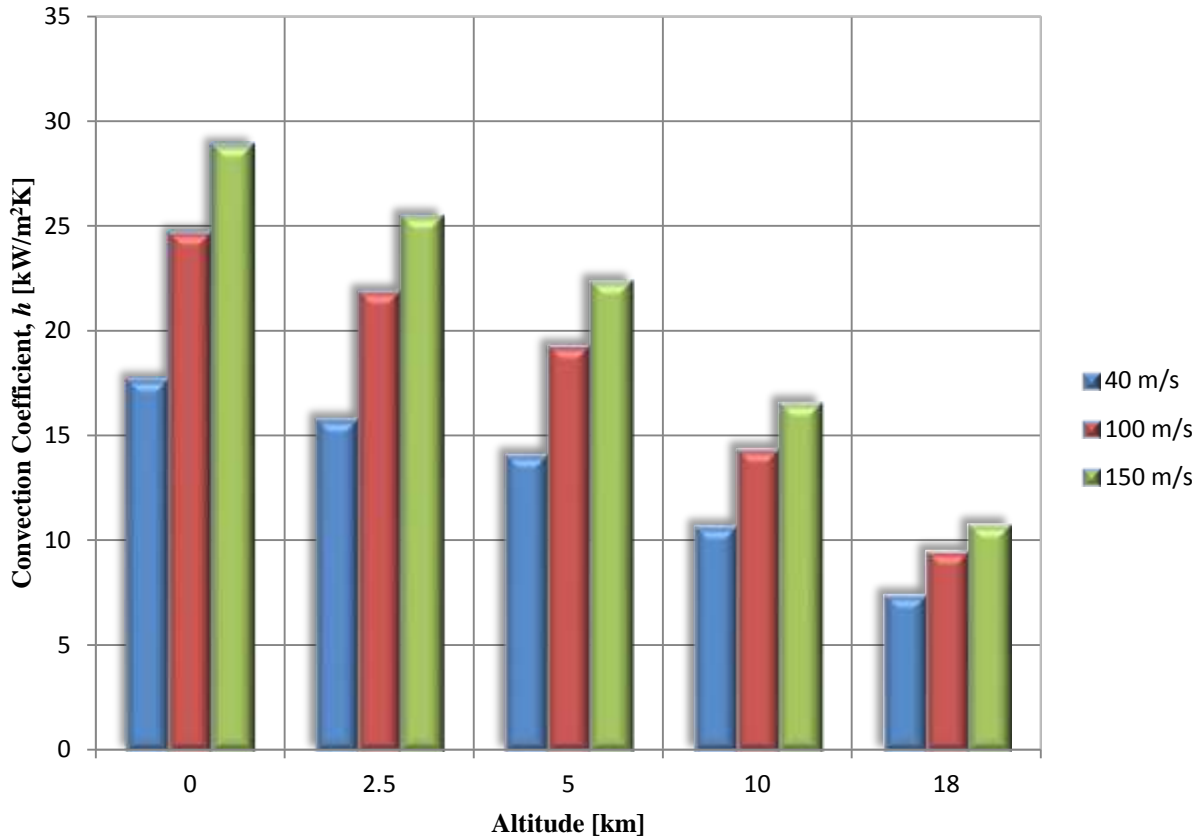
Figure 5.1 Heat transfer convection coefficient shown as a function of altitude at standard conditions and a flow speed of 40, 100 and 150 m/s

In addition to decreased densities and heat transfer convection coefficients, the increase in altitude causes a drop in the hot-wire sensor cold resistance, R_∞, due to the significant decrease in temperature. The hot-wire operating resistance, R_w, must be carefully selected, to circumvent hot-wire burnout. Additionally, it is best practice to select a set-point voltage, V_w, for each altitude or pressure condition, which produces the same R_w at the same flow speed. The safe maximum operating resistance was determined to be 12 Ω at the minimum flight speed. As the

flight speed increases, the heat transfer convection coefficient h increases, thus decreasing the hot-wire operating temperature T_w and operating resistance R_w. Therefore, the decrease in cold resistance R_∞ at high altitudes combined with the selection of the same operating resistance R_w at the minimum flight speed causes the OHRs to increase with altitude.

At sea level and 20 ℃, a hot-wire sensor cold resistance, R_∞, of 6.07 Ω was measured for the TSI probe model 1210-T1.5 (serial number 71105221) [27]. The cold resistance at altitude temperatures were not measured, but were calculated using the following equation:

$$T_b - T_a = \frac{R_b - R_a}{\alpha_0 R_0}.$$

(5.1)

The subscripts, a and b, correspond to reference temperatures, where if the temperature and resistance are known at a, the resistance at b can be calculated at the desired temperature at b, and vice versa. The term in the denominator, α_0, is the temperature coefficient of resistance referenced at 20 ℃, which is a given constant from TSI [27]. The resistance, R_o, is also referenced at 20 ℃. It is important to note that R_∞ only equals R_o at 20 ℃. Otherwise, the cold resistance, R_∞, must be calculated at the ambient temperature. At 18 kilometers (7.5 kPa and 216.6 K), a cold resistance of 4.4 Ω was calculated, corresponding to an OHR of 2.7 at 40 m/s; compared to an OHR of 2 at sea level and 40 m/s. This OHR/altitude relationship establishes that there will be an increase in CVA time constant resulting in a decreased frequency response for increased altitudes. However, CVA sensitivity will benefit from an increase in OHR and therefore altitude.

Predictions with Calibration Curves

The thermal/electrical model was used to develop predicted CVA output, I_w, data points for a range of flight speeds from 40 to 150 m/s. The pressures ranged from 7.5 to 101.3 kPa and assume a constant free stream temperature of 25 ℃ (298 K). The Nusselt number scaling factor *SF* was kept at 1.3 for all predictions. Calibrations in the vacuum chamber involved approximately constant temperature throughout the pressure range ¼ to 1 ATM ($\approx$26.4 to 101.3 kPa) at approximately 25 ℃, without considering temperature variation. Therefore, this prediction is similar to the actual calibrations, but differs in speed range and includes one lower pressure calibration at 7.5 kPa. Although this is simply a prediction, hot-wire burn-out was considered to ensure that these results would be applicable for actual in-flight conditions. As stated previously, set-point voltages V_w, were chosen to produce a safe hot-wire sensor operating resistance, R_w, of 12 Ω at a flow speed of 40 m/s. The theoretical calibration equation power-law exponent, k, was set to 10 for a good fit, which differed from an actual calibration power-law exponent of 16. A similar trend was experienced in the work of Neumeister [17] and Li [21]. This is due to sensitivity drop-off at higher flow speeds during the experiment; whereas the thermal/electrical model does not accurately model this effect, which results in slightly steeper experimental curves (hence different power-law exponents). The resulting *P*, *Q* and *k* constants are presented in Table 5.1 which will be used to develop a single-point autonomous calibration function at constant temperature.

Table 5.1 Power-law curve fit constants for 7.5 to 101.3 kPa at 25 °C

V_w [Volts]	Pressure [kPa]	P	Q	K
0.585	7.50	-12.0	11.2	10
0.708	26.4	1.05	1.23	10
0.800	54.0	5.64	0.333	10
0.849	74.8	7.31	0.176	10
0.898	101.3	8.63	0.097	10

The power-law curves which were fitted to the predicted data are presented in Figure 5.2. As expected, the power-law curves fit the predicted data very well and have much lower MSE compared to the curve fits to actual data from Chapter 3. At 101.3 kPa, the experimental MSE was 0.562 $[\frac{m^2}{s^2}]$, while the predicted data at the same pressure produced an MSE of 0.195 $[\frac{m^2}{s^2}]$. This is anticipated, since; the prediction data is produced by a computer using the thermal/electrical model, while the actual data can be easily influenced by experimental errors.
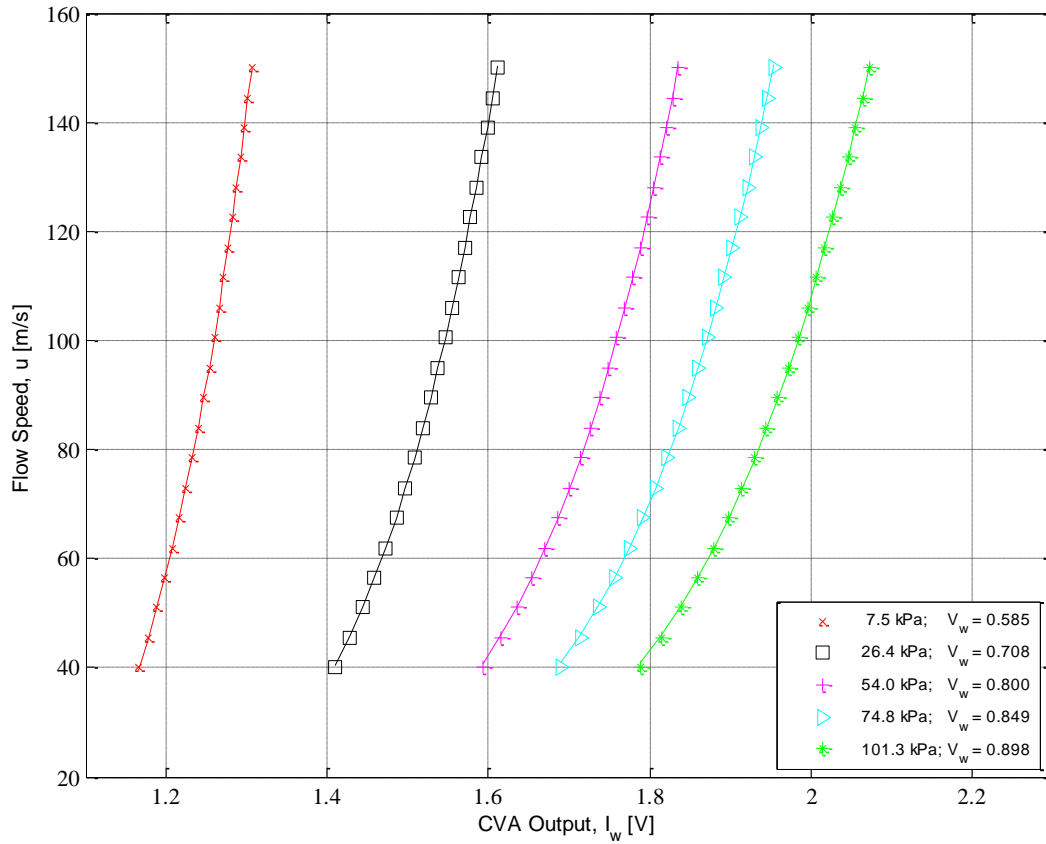
Figure 5.2 Predicted calibration data from the thermal/electrical model presented as symbols and power-law curve fits presented as lines from 7.5 kPa to 101.325 kPa at a constant temperature of 25 ℃

Table 5.2 Pressure, set-point voltages and MSE for the predicted power-law curve fits at a constant temperature of 25 ℃

Pressure [kPa]	7.5	26.4	54.0	74.8	101.3
Set-Point Voltage V_w [Volts]	0.585	0.708	0.800	0.849	0.898
MSE [$\frac{m^2}{s^2}$]	0.038	0.033	0.112	0.156	0.195

Visually, the fits look perfect at all pressures, over the whole range of speeds, therefore; the MSE values are effectively zero. It is interesting to note that, the MSE increases with pressure. This is caused by using a single constant for the power-law exponent, k. A better fit, across the board, is achievable if MATLAB was allowed to choose the k in addition to P and Q.

However, in doing so, the power-law calibration function would no longer be a one degree of freedom equation, and all of the fits seem very reasonable. At 7.5 kPa, the lowest MSE was 0.006 $[\frac{m^2}{s^2}]$, which corresponds to a percent error of 0.08% at 100 m/s. At 101.3 kPa, the highest MSE was 0.358 $[\frac{m^2}{s^2}]$, which corresponds to a percent error of 0.6% at 100 m/s. Therefore, with such infinitesimal MSE values, the power-law fits represent the data very well.

Single-Point Calibration Applied

The power-law curve fits from 7.5 to 101.3 kPa at 25 ºC were then used to establish the relationship between P and Q (Figure 5.3). As mentioned in Chapter 4, the P and Q curve provides a crude fit to the power-law constants.
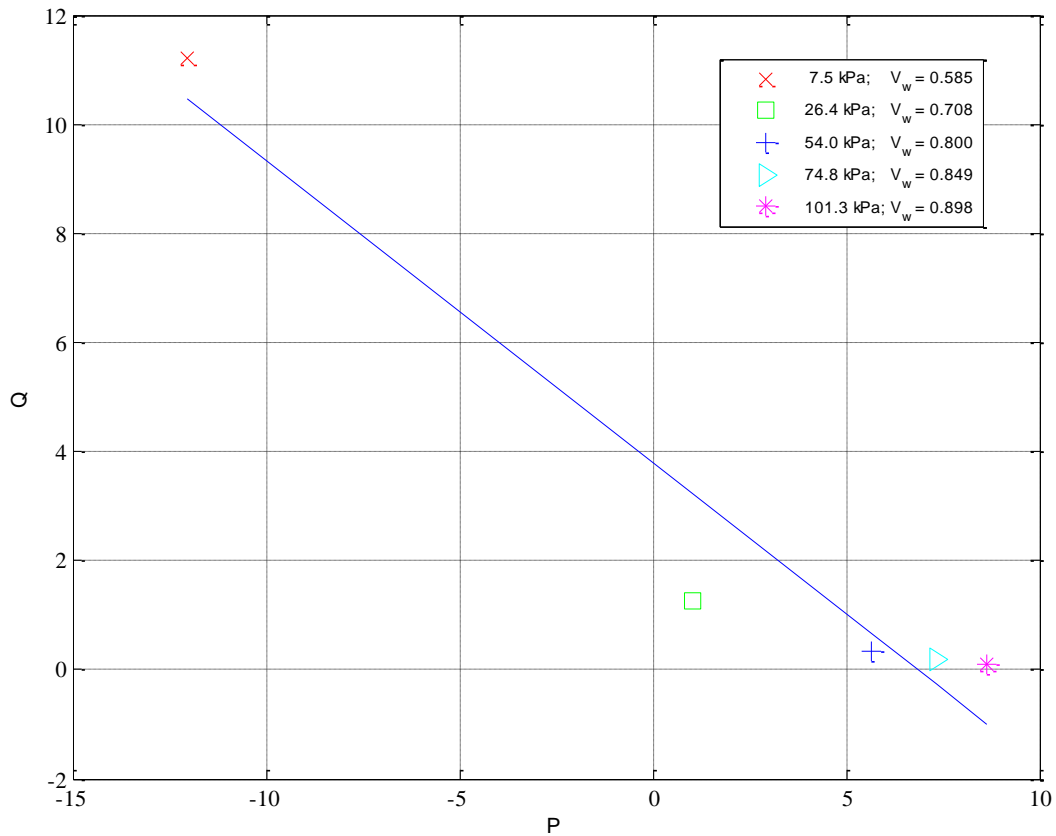
Figure 5.3 *P* and *Q* from the power-law calibration curve fits for 7.5 to 101.3 kPa at 25 ⁰C

Vary Pressure with Constant Temperature (25 ⁰C)

The *P* and *Q* relationship was then used to develop the single-point calibration functions from 7.5 kPa to 101.3 kPa at a constant temperature of 25 ⁰C. The curve corresponding to each pressure, used a single data point at the maximum flow speed; 150 m/s. Curves were produced, using the simulated CVA output data from the thermal/electrical model as the only input thereafter. The results are presented in Figure 5.4; the corresponding MSE values for the fits shown are presented in Table 5.3.
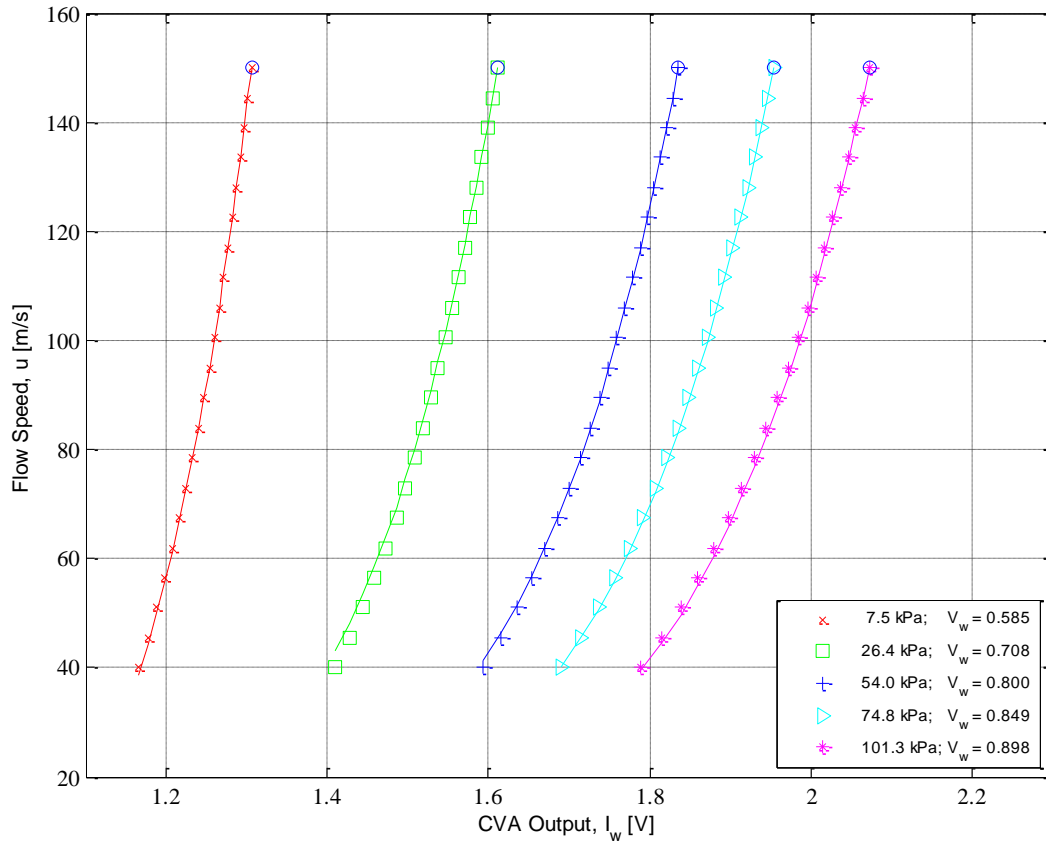
Figure 5.4 Predicted calibration data from thermal/electrical model presented as symbols and single-point calibration curve fits presented as lines from 7.50 kPa to 101.3. kPa

Table 5.3 Pressure, V_w and MSE for the predicted single-point calibration curve fits at a constant temperature of 25°C

Pressure [kPa]	7.50	26.4	54.0	74.8	101.3
Set-Point Voltage V_w [Volts]	0.597	0.726	0.817	0.866	0.916
MSE [$\frac{m^2}{s^2}$]	0.280	2.11	0.177	0.592	1.64

Consideration of the MSE at 26.4 kPa and 101.3 kPa, reveal that the highest amount of error corresponds to what appears to be outliers in the *P* and *Q* curve fit. However, the results appear to have a good visual fit nonetheless. Additionally, at 101.3 kPa, 2.185 [$\frac{m^2}{s^2}$] is the largest MSE

and at 100 m/s results in a percent error of 1.5%. Therefore, the single-point calibration function is considered a good fit.

Influence of Varying Temperature at Constant Pressure (26.4 kPa)

The next analysis involved investigating the effects of a change in temperature at one pressure. The pressure chosen for analysis was 26.4 kPa with temperatures at 248.15 K, 273.15 K and 298.15 K. The set-point voltage, V_w, was chosen at each temperature to produce a safe operating resistance, R_w, equal to 12 Ω, at 40 m/s. The single-point calibration function used to fit the data was developed from the power-law curve fits in Figure 5.2, which involved pressures ranging from 7.5 to 101.3 kPa at a constant temperature of 298.15 K. The thermal/electrical model was implemented to produce the simulated data points at the above stated temperatures. Then the single-point calibration function at 26.4 kPa and 298 K was used in an attempt to fit all of the data. The single data point consisted of the CVA output at maximum flow speed. The following CVA output data points were then plugged into the single-point calibration function. The results of this analysis are presented below in Figure 5.5 and Table 5.4. The single-point calibration curves prove to be good fits. The curve begins to deviate around 75 to 80 m/s providing a turn down of 2. However, the deviation is considered miniscule and a turn down of 2 to 3 was the objective.
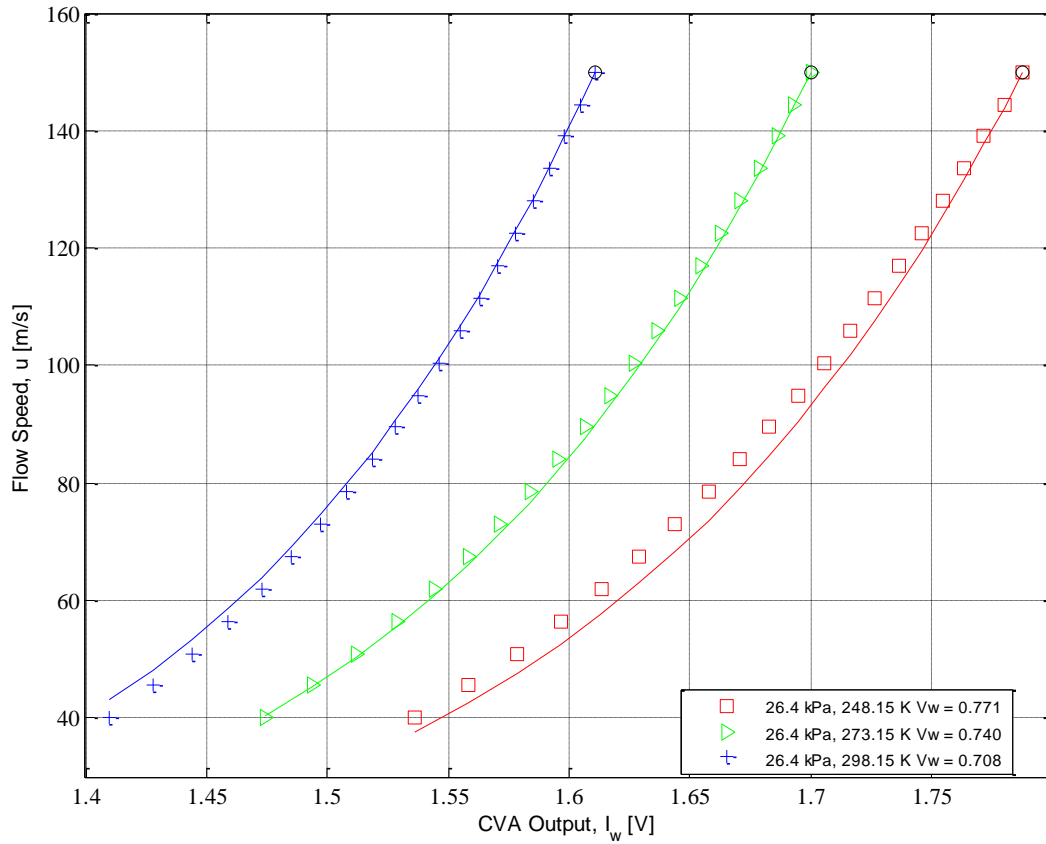
Figure 5.5 26.4 kPa: Predicted calibration data from thermal/electrical model presented as symbols and single point calibration curve fits presented as lines to determine its ability to calibrate with temperature variation

Table 5.4 Pressure, set-point voltage and MSE for the predicted power-law curve fits at 26.4 kPa with temperature variation

Pressure [kPa]	26.4	26.4	26.4
Temperature [K]	248.1	273.1	298.1
Set-Point Voltage V_w [Volts]	0.771	0.740	0.708
MSE [$\frac{m^2}{s^2}$]	13.2	1.73	2.11

The single-point calibration function proves to be a good visual fit. The lowest 26.4 kPa

MSE occurs at 273.15 K with 1.73 $\frac{m^2}{s^2}$ corresponding to a percent error of 1.3% at 100 m/s. The

highest MSE occurs at 248.15 K with 13.2 $\frac{m^2}{s^2}$ corresponding to a percent error of 3.6% at 100

m/s, which is still considered low enough to be a viable solution for in-flight calibration.

Development of a Calibration Equation for Altitude Conditions

The next analysis involved developing a single-point calibration function for altitude

conditions from sea level up to 18 km using pressures and temperatures from U.S. Standard

Atmosphere [34]. The CVA thermal/electrical model was used to produce simulated CVA output

data points in the flow speed range from 40 to 150 m/s. The set-point voltage, V_w, was chosen at

each altitude such that the sensor operating resistance was equal to 12 Ω, at 40 m/s. Power-law

curve fits with exponent k fixed at 10 were applied to the computed data to develop the P and Q

relationship. The results are presented in Figure 5.6 and Table 5.5.
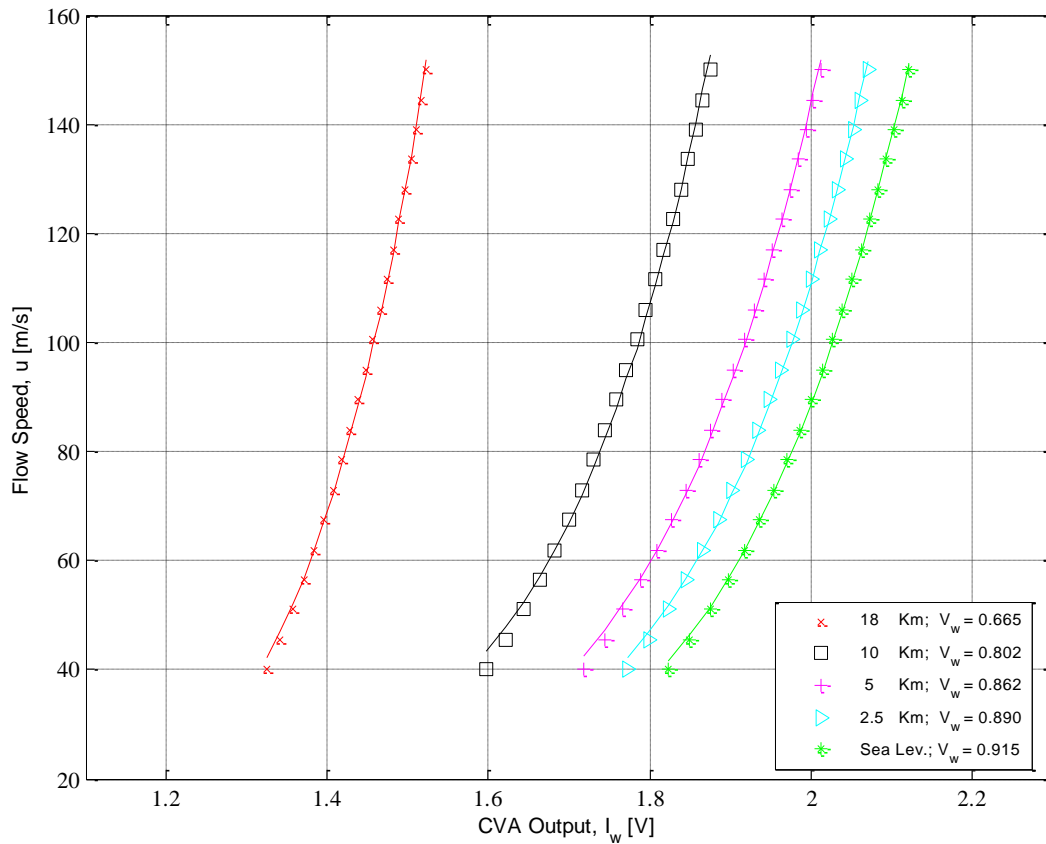
Figure 5.6 Predicted calibration data from thermal/electrical model presented as symbols and power-law curve fits presented as lines from Sea Level to 18 kilometers

Table 5.5 Pressure, set-point voltage and MSE for the predicted power-law curve fits from Sea Level to 18 kilometers

Altitude [km]	18	10	5	2.5	0
Pressure [kPa]	7.5	26.4	54.0	74.8	101.3
Temperature [K]	217	223	256	272	288
Set-Point Voltage V_w [Volts]	0.665	0.802	0.862	0.890	0.915
MSE $[\frac{m^2}{s^2}]$	1.12	2.28	1.34	0.845	0.425

The MSE of the power-law calibration curve fit was used to quantify the goodness of the fit. Once again, the power-law curve fits prove to be a good solution for calibration.

Interestingly, the MSE increases with an increase in pressure and temperature (or decreasing altitude). This same effect occurred with the analysis involving the variation of pressures with the constant temperature at 25°C, which was attributed to the constant power-law exponent, k. The lowest MSE occurs at 0 km with a value of 0.425 $\frac{m^2}{s^2}$, corresponding to a percent error of 0.65% at 100 m/s. The largest MSE occurs at 10 km with a value of 2.28 $\frac{m^2}{s^2}$, corresponding to a percent error of 1.5% at 100 m/s. Therefore, the power-law calibration curves prove to be an excellent fit to the thermal/electrical model predictions.

The power-law calibration curve fits were then used to develop the P and Q relationship in Figure 5.7. Presented as a straight line fit, many of the corresponding points still appear as outliers, as experienced in previous situations. However, the crudeness of the fit does not have a profound effect on the final single-point calibration curves. Thus, continuing with the current analysis should not be deterred by the rudimentary P and Q relationship.
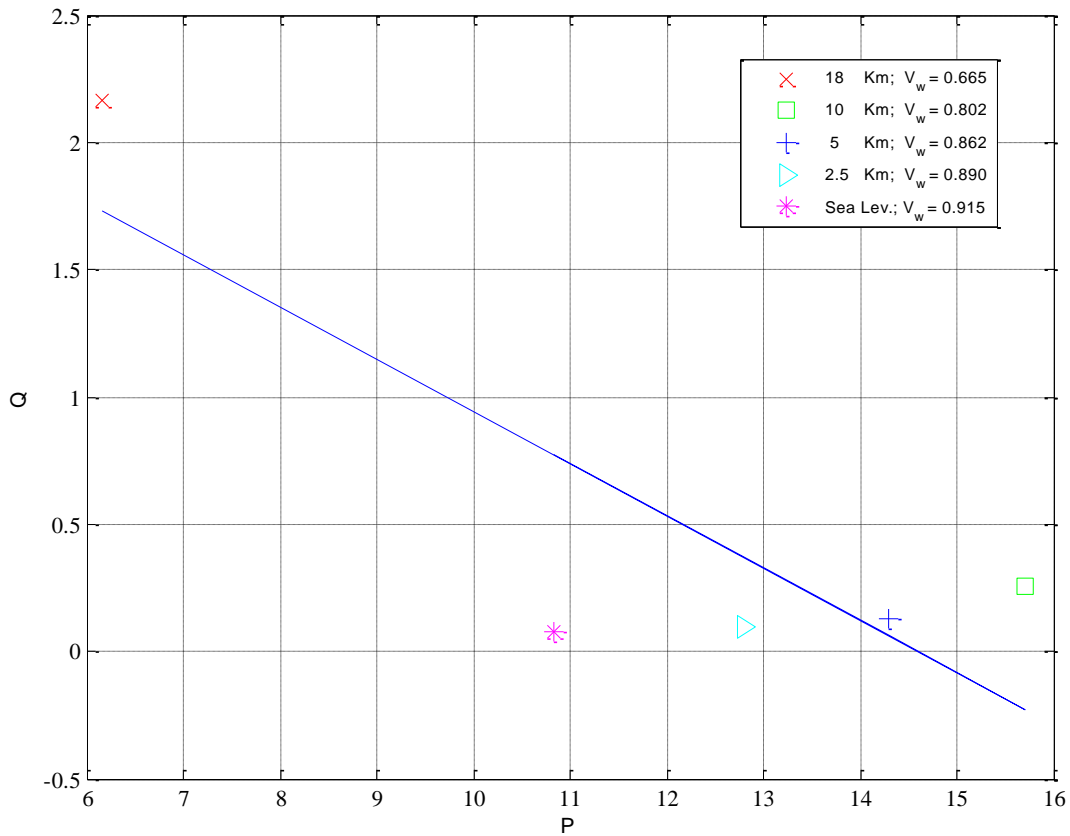
Figure 5.7 *P* and *Q* from the power-law calibration curve fits from sea level to 18 km

It made sense to the author to develop single-point calibration functions corresponding to U.S. Standard Atmosphere. The *P* and *Q* relationship were used in conjunction with the power-law exponent, *k*, to develop one single-point calibration curve corresponding to 18 km. The analysis then proceeded by subjecting the single-point calibration function to an increase and decrease in temperature of 25°C. At 18 km, the pressure is 7.50 kPa with a temperature of 216.65 K. Therefore, the simulated CVA output data, to be compared, consisted of temperatures at 191.65 K and 241.65 K. This meant that the single-point calibration function would have to

adjust for the change in temperature. This analysis is introduced as a worst case scenario, as a 25°C change in temperature would never be expected.

The 18 km results are presented in Figure 5.8 and Table 5.6. The single-point calibration function corresponding to CVA output data at 7.504 kPa and 191.65 K was observed to deviate at a higher flow speed compared to the thermal/electrical model results for 7.504 kPa at 241.65 K. The deviation for this curve, plotted in red with squares, begins right around 115 m/s while the curve corresponding to 241.65 K does not begin to deviate until 80 to 85 m/s, thus producing a turn down of about 2. Despite small deviations, the results proved to be a good visual fit, indicative of a powerful calibration function that can easily adapt to large changes in temperature.
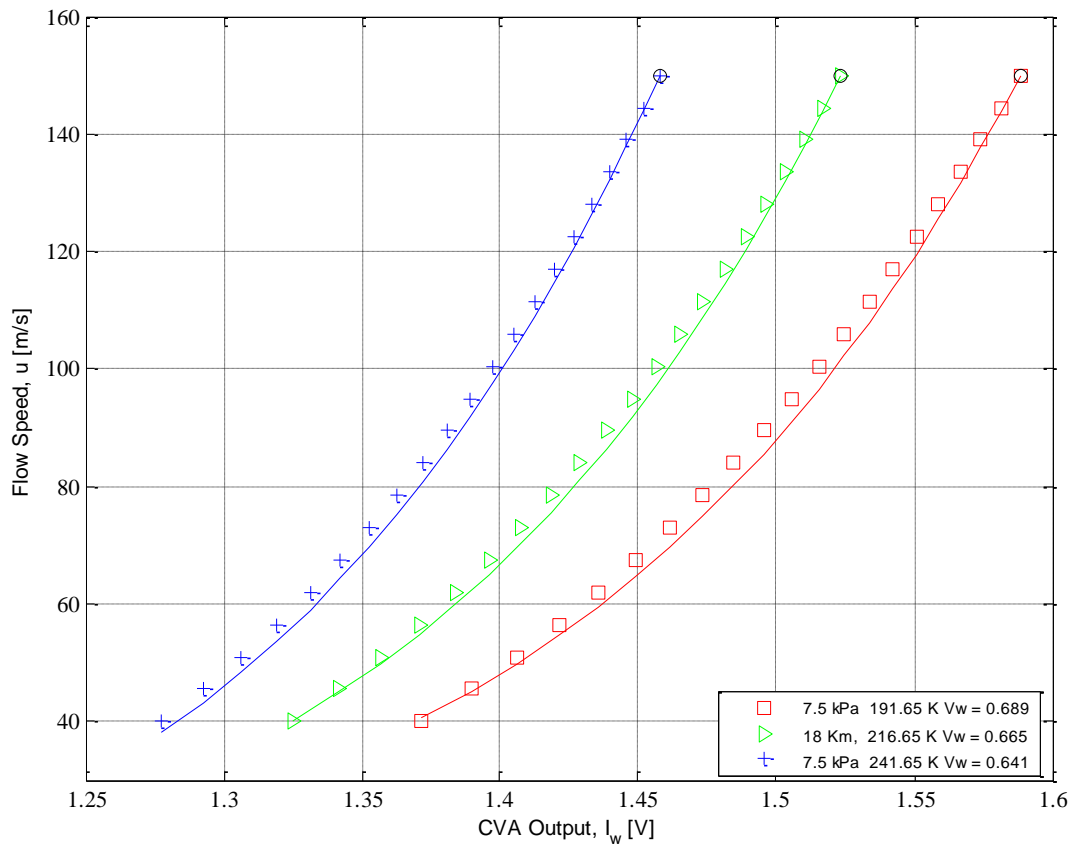
Figure 5.8 18 km single-point calibration with a temperature variation of +/- 25 °C

Table 5.6 Pressure, temperature, set-point voltage and MSE for the single-point calibrations at 18 kilometers with a temperature variation of +/- 25 °C

Pressure [kPa]	7.5	7.5 (18 km)	7.5
Temperature [K]	192	217	242
Set-Point Voltage V_w [Volts]	0.579	0.582	0.588
MSE [$\frac{m^2}{s^2}$]	7.80	5.06	6.31

The MSE is presented here to quantify the goodness of fit for the single-point calibrations at 18 km with off-standard temperatures. As expected, the lowest MSE occurs at the pressure altitude from which the single-point calibration function was developed. This is in contrast to the single-point calibration function developed for 26.4 kPa at 298 K, where the calibration function was used to apply to temperatures at 273 K and 248 K. The lowest MSE was calculated at 5.06 $\frac{m^2}{s^2}$, corresponding to a percent error of 2.2% at 100 m/s. The highest MSE occurred at the lowest temperature of 192 K with a value of 7.80$\frac{m^2}{s^2}$, corresponding to a percent error of 2.8% at 100 m/s. Therefore, even with a high MSE, the associated percent error is still small enough to be considered a good fit. The implementation of CVA into BLDS will be presented briefly in the next section.

Operation of CVA with BLDS

Extensive details were presented by Li [21] on how to implement CVA into BLDS software and will be summarized in this thesis. Unlike laboratory experiments using the CVA instrument panel that require the use of a knob to select a set-point voltage, V_w; it must be done in digital increments for flight applications. BLDS has analog inputs and digital outputs; hi or

low. Don Frame designed BLDS-CVA so that it would operate, first, by powering up and then it comes to a state. The V_w must be checked to ensure that R_w is not too high. BLDS-CVA uses a toggle switch that open circuits the sensor, allowing the user to set V_w and then the circuit closes. The circuit may have to be toggled 10 times to achieve the desired V_w. The circuit is now closed and BLDS-CVA is operating. To read the A/D signal there is the potential for two methods; either implement calibrations on the fly and store the corrected u without storing any voltages, or slowly increment sums/averages and RMS statistics.

At first, the free stream temperature will be measured with a thermocouple and the free stream velocity will be measured using a Pitot tube. Using the stage, the hot-wire will be driven to the free stream to choose a V_w that does not exceed maximum R_w. Then V_w will be slowly incremented and I_w will be measured. Then R_w can be calculated and a decision will be made whether or not to keep increasing V_w. An R_w equal to 12 Ω cannot be selected for a free stream velocity. A value closer to 10 Ω in the free stream can be selected and then a simulation can be used to predict safe R_w values within the boundary layer. Another option may include the development of an equation with a curve fit for predicting safe R_w values at different altitudes for the flight regime with a turn down of 3 to 4. A flow chart implementation of CVA operation with BLDS is presented in Appendix H.

Predicted CVA Frequency Response and Sensitivity at Altitude

The conditions used to develop the single-point calibration functions at U.S. Standard Atmosphere altitudes were used to predict CVA frequency response and sensitivity at 80 m/s and 150 m/s [34]. As stated previously, the conditions involved using set-point voltages that

produced operating resistances of 12 Ω at 40 m/s. The predicted time constant and frequency response results are presented in Table 5.7.

Table 5.7 Predicted time constants and frequency response at U.S. Standard Atmosphere altitudes

$R_w = 12\ \Omega$ at 40 m/s					
Altitude [km]	Set-Point Voltage V_w [Volts]	80 m/s M_{cva} [ms]	150 m/s M_{cva} [ms]	80 m/s cutoff Freq. [kHz]	150 m/s cutoff Freq. [kHz]
Sea level	0.915	0.080	0.065	3.44	4.24
2.5	0.890	0.088	0.072	3.12	3.84
5	0.862	0.098	0.079	2.82	3.45
10	0.802	0.122	0.100	2.26	2.74
18	0.665	0.185	0.156	1.49	1.77

The predicted trend is consistent with previous work from Neumeister [17] and Li [21]. The CVA sensor time constant increases with an increase in altitude. Taking a close look at the equation for the CVA time constant from (3.13) reveals the source of this trend. As mentioned previously, increasing altitude causes a decrease in the probe cold resistance R_∞. The OHR then increases, because of this trend, and causes the $(1+a_w)/(1+2a_w)$ ratio to decrease. This may suggest that the time constant will decrease with increase in altitude, but there are two other contributing factors inherent in the equation. First, the increase in altitude causes a decrease in the free stream density, ρ_∞, which also causes the Reynolds number, Re_∞, in the denominator to drop. Second, the free stream thermal conductivity, k_∞, in the denominator also decreases. Therefore, density and thermal conductivity are the main contributors to the increase in CVA time constant and the decrease in cutoff frequency.

The CVA velocity sensitivity coefficient was also calculated using the thermal/electrical model with equation (3.15b), at free stream pressures and temperatures from sea level to 18 km, within the flow speed range of 40 to 150 m/s. The results are presented in Figure 5.9. The predicted trend shows a decrease in sensitivity with increase in flow speed at all altitudes. This is caused by the decrease in OHR at increasing flow speeds. CVA sensitivity improves with increasing altitude. For example, at sea level with a flow speed equal to 40 m/s, the sensitivity coefficient was predicted at 0.156, while at the same flow speed at 18 km, the value jumps to 0.182. This corresponds to a 16% increase in sensitivity from sea level to 18 km.
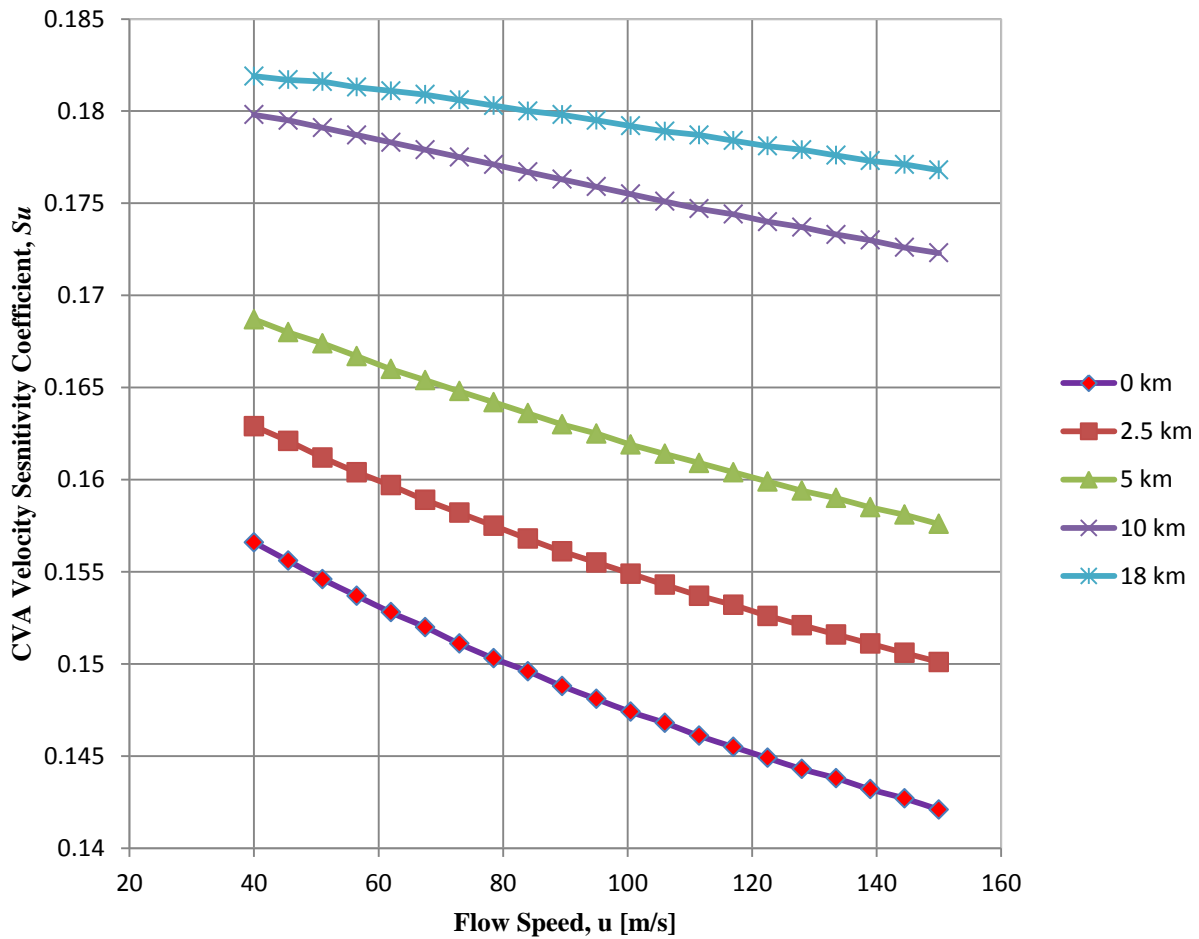
Figure 5.9 Sea Level: CVA sensitivity presented as a function of increasing flow speed

The influences of high altitude effects (i.e. low ambient pressures and temperatures) have been extensively examined. Unfortunately, the density and thermal conductivity at high altitude dictate an increase in CVA time constant and a decrease in frequency response. CVA frequency response, for altitude conditions especially, can be improved with the use of a smaller diameter hot-wire sensor. The CVA time constant is approximately proportional to the diameter raised to the 3/2 power; therefore decreasing the diameter will decrease the time constant, thus increase frequency response. However, sensitivity is expected to increase with an increase in altitude. Predictions were made for pressures from 7.5 kPa to 101.3 kPa at a constant temperature of 25 °C. These were used to develop calibrations and single-point functions for analysis. A study was then conducted to analyze the effects of a single-point calibration at 26.4 kPa with an increase and decrease in temperature of 25 °C. This proved to be a good solution and satisfied a flow speed turn down of 2. The next analysis involved an increase in altitude using U.S. Standard Atmosphere from sea level to 18 km [34]. Calibration predictions as well as single-point calibrations were developed at each altitude. The study then proceeded by analyzing a single altitude of 18 km with an increase and decrease in temperature of 25 °C. With the decreased temperature, deviations in the single-point calibration curve occur at 115 m/s (corresponding to a turn down of 1.3). Conversely, the results for increased temperature began to deviate around 80 m/s producing a turn down close to 2. The single-point calibration presented in this thesis proves to be a viable solution for autonomous calibration in flight.

6. Conclusions and Recommendations

The explicit measurement of velocity *fluctuations* in the boundary layer has been the motivation behind the development of the constant voltage anemometer (CVA) for the boundary layer data system (BLDS). CVA has proven to be a possible solution for the measurement of velocity fluctuations on aircraft. Previous work used the CVA thermal/electrical model to investigate the effect of in-flight CVA output performance at altitude, but there was no way to quantify the effects of decreased pressure. With the challenges inherent with in-flight calibration, a test environment needed to be developed to calibrate inside a laboratory. Thereafter, progress could be made by developing an autonomous single-point calibration function.

Conclusions

1.   The calibration jet apparatus was designed and fabricated by the author, to calibrate a 3.8 micron diameter, 6 ohm cold resistance at 20 °C, platinum-coated tungsten probe (TSI 1210-T1.5) inside a vacuum chamber [27]. The calibration jet apparatus demonstrated laminar flow at the nozzle exit with a flow speed range of 14 to 50 m/s, while operating inside a vacuum chamber.

2.   CVA hot-wire calibrations were conducted inside the vacuum chamber at a pressure range of ¼ ATM to 1 ATM. Calibration data was collected down to ¼ ATM; a first in hot-wire research.

3.   The CVA thermal/electrical model output predictions were compared to the corrected experimental CVA output data, which confirmed the performance of the model to predict the trend observed in experimental data. As discovered by Neumeister, the Collis and Williams

correlation under-predicts the heat transfer; resulting in predicted CVA output data, I_w, that under-shoots the experimental data [17] [19].

4.   The CVA thermal/electrical model will need to be used for future predictions; therefore the Nusselt number was scaled by 1.3 to better fit the experimental data. With this adjustment, the scaled thermal/electrical model produced the same quality of prediction for varying pressure. At low flow speeds, the scaled curve undershoots the experimental CVA output voltage, I_w, data; while at high speeds it overshoots slightly. The scaled curve appears to need a slight shift about the mid-range velocities, to better fit the data.

5.   The single-point calibration function was developed using experimental data in conjunction with power-law calibrations and was then applied to the experimental CVA output data. After success with the experimental data, single-point calibrations were developed for pressures ranging from 7.5 kPa to 101 kPa at 25ºC, in which the calibration proved capable of adjusting to temperature variations. A similar study was conducted involving altitudes from 0 to 18 km, where the single-point calibration proved itself capable of adjusting to large temperature variations. The single-point calibration function has displayed that it is able to calibrate the CVA hot-wire within a host of test regimes with the largest deviations being $\pm$ 5 m/s at mid-range velocities.

6.   CVA frequency response and sensitivity were also analyzed at altitude conditions from sea level to 18 km. Interestingly, an increase in altitude will cause CVA frequency response to decrease, but CVA sensitivity will improve. This is beneficial; the sensitivity will improve with an increase in altitude, therefore the accuracy of experimental data should improve for measurements at increasing altitudes, but the decrease in CVA frequency response will negatively affect fluctuating velocity measurements.

Recommendations

1. The CVA thermal/electrical model needs to be improved to better predict the CVA output response to flow speed. The improvement may involve the addition of a radiation model.

2. Code needs to be written to implement the autonomous single-point calibration function into the BLDS software. Previous codes have been written by Hon Li for this purpose and should be thoroughly considered as a starting point [21].

3. Improving the CVA frequency response will be necessary, especially for operation at high altitude conditions. The CVA time constant is approximately proportional to the hot-wire diameter raised to the 3/2 power; therefore decreasing the diameter will decrease the time constant thus increasing the frequency response.

4. Flight tests involving BLDS-CVA will be next.

REFERENCES

[1] L. K. Loftin Jr., Quest for Performance, The Evolution of Modern Aircraft, Washington, DC: NASA, Scientific and Technical Information Branch, 1985.

[2] H. Schlichting, Boundary-Layer Theory, New York: McGraw-Hill, 1979.

[3] E. L. Houghton, P. W. Carpenter, S. H. Collicott and D. T. Valentine, Aerodynamics for Engineering Students, Amsterdam: Elsevier, 2013.

[4] F. M. White, Viscous Fluid Flow, New York: McGraw-Hill, 2006.

[5] S. Lillywhite, "Microphone-Based Pressure Diagnostics for Boundary Layer Transition," California Polytechnic State University, San Luis Obispo, 2013.

[6] R. Joslin, "Overview of Laminar Flow Control," NASA-TP-1998-208705, Langley Research Center, Hampton, Virginia, 1998.

[7] A. Wazzan, "Spatial and Temporal Stability Charts for the Falkner-Skan Boundary-Layer Profiles," Clearinghouse, Springfield, VA, 1968.

[8] D. Bushnell and J. Hefner, "Progress in Astronautics and Aeronautics, Volume 123: Viscous drag reduction in Boundary Layers," *American Institute of Astronautics and Aeronautics,* vol. 123, 1990.

[9] R. V. Westphal, M. Bleazard, A. Drake, A. M. Bender, D. Frame and S. R. Jordan, "A Compact, Self-Containing System for Boundary Layer Measurement in-Flight," in *AIAA-2006-3828, AIAA Meeting Papers on Disc [CD-ROM]*, Reston, VA, 2006. No.10-13.

[10] A. M. Bender, R. V. Westphal and A. Drake, "Application of the Boundary Layer Data System on a Laminar Flow Swept Wing model In-Flight," in *AIAA-2010-4360, AIAA Meeting Papers on Disc [CD-ROM]*, Reston, VA, 2010.

[11] A. Karasawa, "Unsteady Total Pressure Measurement for Laminar-to-Turbulent Transition Detection," MS. Thesis, California Polytechnic State University, San Luis Obispo, 2011.

[12] L. Fingerson, "Thermal Anemometry, Current State and Future Directions," *Review of Scientific Instruments,* vol. 65, no. 2, pp. 285-300, 1994.

[13] R. McClellan, "Equilibrium Temperature and Heat Transfer Characteristics of Hot Wires in Supersonic Flow," MS thesis, California Institute of Technology, Pasadena, CA, 1955.

[14] T. R. Moes, G. R. Sarma and S. M. Mangalam, "Flight Demonstration of a Shock Location Sensor Using Constant Voltage Anemometry," NASA Dryden Flight Research Center, Edwards, CA, 1997.

[15] G. Sarma, "Flow Rate Measuring Apparatus". United States Patent 5074147, December 1991.

[16] G. Sarma, "Analysis of a Constant voltage Anemometer Circuit," in *Instrument Measurement and Technology Conference*, Irvine, 1993.

[17] W. Neumeister, "Hot-Wire Anemometer for the Boundary Layer Data System," MS Thesis. California Polytechnic State University, San Luis Obispo, 2012.

[18] G. Sarma, "Transfer Function Analysis of the Constant Voltage Anemometer," *Review of Scientific Instruments,* vol. 69, no. 6, pp. 2385-2391, 1998.

[19] D. Collis and M. Williams, "Two-Dimensional Convection from Heated Wires at Low Reynolds Numbers," *Journal of Fluid Mechanics,* vol. 6, no. 3, pp. 357-384, 1959.

[20] G. Sarma and G. Comte-Bellot, "Automated Constant Voltage Anemometer for Measurements with Fluid Temperature Drifts," *Review of Scientific Instruments,* vol. 73, no. 3, pp. 1313-1317, 2002.

[21] H. Li, "Constant Voltage Hot-Wire Anemometry for the Boundary Layer Data System," MS Thesis, California Polytechnic State University, San Luis Obispo, 2013.

[22] T. Incorporated, *Model 1127/1128 Air Velocity Calibrator,* Shoreview, Mn, 2000.

[23] R. Westphal, "Chapter 9 Wind Tunnel Design," in *Thermal Measurements in Electronics Cooling*, K. Azar, Ed., Waltham, Massachussetts: CRC Press, 1997, pp. 321-348.

[24] B. Munson, D. Young, T. Okiishi and W. Heubsch, Fundamentals of Fluid Mechanics, Missouri: R.R. Donnelley, 2009.

[25] J. Barlow, W. Rae Jr. and A. Pope, Low-Speed Wind Tunnel Testing, Canada: Wiley, 1999.

[26] R. Mehta, "Turbulent Boundary Layer Perturbed by a Screen," *AIAA Journal,* vol. 23, no. 9, 1985.

[27] T. Incorporated, *Thermal Anemometry Probes,* Shoreview, MN, 2008.

[28] H. H. Brunn, Hot-Wire Anemometry, New York: Oxford University Press, 1995.

[29] J. Hinze, Turbulence, New York: McGraw-Hill, 1975.

[30] "EES," F-Chart Software, 2015. [Online]. Available: http://www.fchart.com/ees/.

[31] G. Comte-Bellot and G. Sarma, "Constant voltage anemometer practice in supersonic flows," *AIAA Journal,* vol. 29, no. 2, pp. 261-270, 2001.

[32] G. Comte-Bellot, "Ch. 34," in *The Handbook of Fluid Dynamics*, CRC Press, 1998.

[33] L. King, "On the Convection of Heat from Small Cylinders in a Stream of Fluid: Determination of the Convection Constants of Small Platinum Wires, with Applications to Hot-Wire Anemometry," in *Proceedings of the Royal Society of London. Series A, Containing Papers of a Mathematical and Physical Character*, London, September 1914.

[34] "U.S. Standard Atmosphere," Government Printing Office, Washington, D.C., 1976.

Appendix A.   CVA Operation Procedure

CVA Quick Reference Guide

Required Equipment

CVA System

3 BNC cables

2 Digital Volt Meters (DVM)

Hot-wire probe support

Probe support shorting plug

Hot-wire probe

Nomenclature

V_w (V) = Constant voltage value across hot-wire probe

R_w (Ω) = Wire resistance at operating temperature (hot)

R_∞ (Ω) = Wire resistance at room temperature (cold)

I_w (mA) = Current through wire

R_{lim} (Ω) = Threshold at which wire voltage will decrease by 0.1 V

Output Conversions

System Parameter		Calculation Using CVA Output
V_w (V)	=	**V_w-Out** = **V_w-Set**
I_w (mA)	=	(40 mA/V) x **I_w-Out** (V)
R_w (ohms)	=	(5 Ω/V) x **R_w-Out** (V) – box (0.1 Ω) – BNC cable res. (Ω) – probe support res. (Ω) – internal probe res. (Ω)
R_∞ (ohms)	=	DVM reading (Ω) – BNC cable res. (Ω) – probe support res. (Ω) – internal DVM res. (Ω) – internal probe res. (Ω)
R_{lim} (ohms)	=	(2.5 Ω/revs) x **R-Limit** (# revs)

Operation Procedure

1. Ensure the **Ext., Off, and Int.** selector switch is set to the middle **Off** position.
2. Flip **Power** switch up to turn CVA system on. **Power** LED should light green and the **R-Limit** indicator should light red.
3. Set wire voltage (V_w) to 0.1 V using **V_w-Set** knob dial.
   Note: Measuring **V_w-Out** on a DVM without **Ext.** mode active will not show the true V_w; use numbers on knob dial.
4. Connect the probe support to one end of a BNC cable and the opposite BNC cable end to a DVM that outputs a low short circuit current (≤ 1 mA). Install probe support shorting plug. Measure and record combined resistance of the BNC cable, probe support, and internal DVM resistance. Turn off DVM.
5. Remove shorting plug from probe support and carefully install hot-wire probe. Record probe serial #.
6. Now measure combined hot-wire probe resistance with DVM and subtract off total resistance from step #4, as well as manufacturer specified internal probe resistance. The remaining value in ohms is the cold wire resistance (R_∞).
7. Remove BNC cable end connected to DVM and connect to the **Sensor** output on CVA system.
8. Set the resistance limit (R_{lim}) threshold to a couple ohms above R_∞ found in step #6 using the **R-Limit** knob dial. There are 2.5 ohms per revolution of the **R-Limit** knob dial.
   Warning: If probe resistance exceeds the **R-Limit** setting in ohms (R_{lim}), as indicated by red **R-Limit** LED illumination, V_w will drop 0.1 volts for burnout protection. V_w will raise back up 0.1 V when probe resistance is cooled below R_{lim}, indicated by the **R-Limit** LED colored green.
9. Connect one DVM to the **V_w-Out** BNC jack and another DVM to the **R_w-Out** BNC jack.
10. Move the selector switch left to **Ext.** from the center **Off** position. The **R-Limit** LED should turn green as a result of step #8 and **V_w-Out** should read 0.1 V on DVM.
11. Measure the cold probe resistance (R_∞) with the CVA by gradually lowering the **V_w-Set** knob dial over the 0.04 V – 0.05 V range while monitoring **R_w-Out** using the connected DVM with 5 Ω/V. Record the lowest observed resistance and verify that it is similar to the combined resistance ($<$ 0.5 Ω difference) from step #6.
12. Increase V_w back to 0.1 V and move selector switch to the **Off** position.
13. Position the hot-wire sensor within a nozzle diameter of the Cal-Jet nozzle outlet or set-up probe in wind-tunnel.
14. Set **R-Limit** to a couple ohms above the expected probe's hot operating resistance (R_w) using

$$R\ Limit(\#revs) = \frac{OHR\ x\ R_\infty\ (\Omega)}{2.5\ \Omega/rev}\ and\ OHR = \frac{R_w}{R_\infty}.$$

15. Turn **AIRFLOW ON** and adjust to velocity at first measurement point.

16. Move the selector switch left to **Ext.** from the center **Off** position. V_w**-Out** should read 0.1 V on DVM.

17. Increase V_w to desired set-point within 0-1 V range (**The <u>RESET</u> button on the top of the instrument panel will need to be pushed at this time. Otherwise the set-point voltage V_w will continue in safe mode.**) while monitoring R_w**-Out** with connected DVM.
    Calculate necessary value for R_w**-Out** from OHR with respect to flow speed using

    $$R_w\ Out(V) = \frac{OHR\ x\ R_\infty(\Omega) + res.\ offsets\ incl.\ 0.1\ \Omega\ for\ CVA\ box}{5\left(\frac{\Omega}{V}\right)}.$$

    Never exceed an OHR > 2.0. Lock V_w**-Set** knob dial before measurements.

18. Once V_w is properly set, use one of the DVMs for measuring the op-amp output voltage, V_o**-Out**, or the wire current output, I_w**-Out**, for mean and RMS data. Use the other DVM for monitoring the mean R_w**-Out** or V_w**-Out**.
    Note: Set DVM to Volt range for mean data and mV range for RMS data, in order to avoid accuracy problems.

19. The **R-Limit** LED should remain solid green during operation. If **R-Limit** LED illuminates solid red, immediately flip selector switch to **Off** from **Ext.** in an effort to protect the probe. Recheck R_{lim}, R_∞, and the V_w set-point.

20. If the **R-Limit** LED blinks red (possibly during large turbulent fluctuations), check that the mean value of R_w**-Out** will not cause OHR > 2.0. If safe, try increasing R_{lim} by turning the **R-Limit** knob dial ½ a revolution, equal to 1.25 ohms, in order to stabilize the green **R-Limit** LED.

21. **Once measurements are complete, DO NOT reduce airflow below first measurement point.**

22. Move selector switch to **Off** from the **Ext.** position. The **R-Limit** LED should turn red.

23. Flip **Power** switch down to power off CVA. All LED lights should become dark.

24. Decrease V_w back down to 0.1 V using V_w**-Set** knob dial.

25. Turn off airflow and DVMs.

26. Carefully remove hot-wire probe from probe support and return probe to original case.

Appendix B.   CVA Calibration Prediction (EES Code)

CVA Thermal/Electrical Model

Collis and Williams applies to fluid properties at film temperature

$\rho_f = \rho \, (\text{Air}, T = T_f, P = P_{atm})$ kg/m^3

$\mu_f = \textbf{Visc} \, (\text{Air}, T = T_f)$ N-s/m^2

$\nu_f = \dfrac{\mu_f}{\rho_f}$ m^2/s

$cp_f = \textbf{Cp} \, (\text{Air}, T = T_f)$ J/kg-K

$Pr = \textbf{Pr} \, (\text{Air}, T = T_f)$

$k_{film} = \textbf{k} \, (\text{Air}, T = T_f)$ W/m-K

Determine Ambient Fluid Properties

$\rho_\infty = \rho \, (\text{Air}, T = T_\infty, P = P_{atm})$ kg/m^3

$\mu_\infty = \textbf{Visc} \, (\text{Air}, T = T_\infty)$ N-s/m^2

$k_\infty = \textbf{k} \, (\text{Air}, T = T_\infty)$ W/m-K

$Re_\infty = \rho_\infty \cdot U \cdot \dfrac{D}{\mu_\infty}$

Ambient Conditions

$P_{atm} = 7.504831$ kPa

$T_\infty = 216.65$ K

Probe Specifications

$A_s = \pi \cdot D \cdot L$ Surface Area for cross-flow convection

$L = 0.00127$ 1.27mm Length wire - TSI 1210 T-1.5

$D = 0.0000038$ 3.8 micron dia. wire- TSI 1210 T-1.5

$b_{20} = 0.0042$ deg.C^{-1}

$C_w = 140$ J/kg-K Wire specific heat

$\rho_w = 20000$ kg/m^3 Density of wire rounded up from 19300 since platinum-coated

$m_w = \dfrac{\pi}{4} \cdot D^2 \cdot L \cdot \rho_w$ kg, Mass of wire for specific heat multiplier

$T_f = \dfrac{T_w + T_\infty}{2}$ K

$T_{wcel} = T_w - 273.15$ [K]   Temperature output in Celsius for display purposes

$U = 50$ m/s, Flow Velocity

Thermal Equilibrium

$V_w = I_w \cdot R_w$ V

$P_w = I_w \cdot V_w$ W

$P_w = h \cdot A_s \cdot (T_w - T_\infty)$ Cylinder in cross-flow convection

Circuit Properties

R_2 = 50   Ohms

R_F = 1000   Ohms

R_P = 0.17   Ohms, Internal Probe Resistance

R_C = 0.38   0.11 + 0.02   Ohms, Cable and ProbeSupport Resistance

V_{wtotal} = 0.5785   V, Total Set-Point Across Cable Containing Probe

Resistance Relations

$R_w = R_\infty \cdot (1 + b_{20} \cdot (T_w - T_\infty))$ Probe Resistance Assuming Linear Temperature Dependent

R_∞ = 5.98   Ohms, Measured Cold Resistance At 20 deg. C

$OHR = \dfrac{R_w}{R_\infty}$

$a_w = \dfrac{R_w - R_\infty}{R_\infty}$

Nusselt Number from Collis Williams Correlation

Scaling Factor used to adjust the heat transfer. Collis and Williams underpredicts this Nu particular hot-wire by 30%

SF = 1.3

$Nus = SF \cdot (A + B \cdot Re_{film}{}^n) \cdot \left[\dfrac{T_f}{T_\infty}\right]^{0.17}$

A = 0.24

B = 0.56

n = 0.45

$Nus = h \cdot \dfrac{D}{k_{film}}$

$Re_{film} = \rho_f \cdot U \cdot \dfrac{D}{\mu_f}$ Collis Williams Coefficients Valid for 0.02<Re<44

Output Parameters

$V_o = \left[1 + \dfrac{R_2}{R_F} + \dfrac{R_2}{R_{wtotal}}\right] \cdot \dfrac{V_{wtotal}}{2}$ V

$R_{wtotal} = R_w + R_C + R_P$ Ohms

$V_{wtotal} = I_w \cdot R_{wtotal}$ V

$I_{wmA} = I_w \cdot 1000$ [dim/A]   mA

$I_{wvolts} = \dfrac{I_{wmA}}{40\ \text{[dim/V]}}$ V, Actual CVA outputs Voltage with 40 mA/Volt

$PDR = \dfrac{P_w}{R_w - R_\infty}$ W/ohm, Temperature Correcte Calibration Quantity

Calculated Time Constant and Frequency Response

$M_{cca} = C_w \cdot m_w \cdot \left[\dfrac{R_w - R_\infty}{b_{20} \cdot I_w{}^2 \cdot R_\infty{}^2}\right]$ sec

$$M_{cva} = \frac{M_{cca}}{1 + 2 \cdot a_w} \quad sec$$

$$M_{cvams} = M_{cva} \cdot 1000 \quad [ms/s] \quad ms$$

$$H_{ratio} = \left(1 + (2 \cdot \pi \cdot f_{cva})^2 \cdot M_{cva}^2 \right)^{\left[\frac{-1}{2} \right]}$$

$$H_{ratio} = 0.5 \quad \text{Calculate Frequency at Half Amplitude}$$

89

Appendix C.   Calibration Apparatus System Model (EES Code)

Ryan Murphy

Fan Curve Analysis

$P_{vac} = 0.25$ atm

$P_{vac,conv} = P_{vac} \cdot 406.8$ [inH2O/atm]   inH2O

$T_{vac} = 77$ F

$\rho_{vac} = \rho\,(\,Air\,,\,T=T_{vac}\,,\,P=P_{vac}\,)$ lbm/ft^3

$\rho_{vac,conv} = \dfrac{\rho_{vac}}{32.174 \;\; [lbm/slug]}$ slug/ft^3

$\mu_{vac} = Visc\,(\,Air\,,\,T=T_{vac}\,)$ lbm/ft-hr

$\mu_{vac,conv} = \mu_{vac} \cdot 0.0000086336103$ [lbf-hr-s/(lbm-ft)]   lbf-s/ft^2

$\nu_{vac} = \dfrac{\mu_{vac,conv}}{\rho_{vac,conv} \cdot 1 \;\; [lbf-(s^{2)/}(ft-slug)]}$ ft^2/s

Cross Section Nozzle

$U_{jet} = 164.32209$ ft/s

$U_{MPH} = U_{jet} \cdot 0.681818$ [mph/ft/s]   mph

Nozzle Diameter

$D_4 = \dfrac{0.385}{12}$ ft

Length of nozzle center-line

$L_4 = 0.1818$ ft

Nozzle Area

$A_4 = \dfrac{\pi \cdot D_4^{\,2}}{4}$ ft^2

$Q_4 = A_4 \cdot U_{jet} \cdot 60$ [s/min]   CFM

Colebrook Friction Formula

$K_L = 0$ Nozzle Exit

$P_{LMinor,4} = \dfrac{K_L \cdot \rho_{vac,conv} \cdot U_{jet}^{\,2}}{2}$ psf

$P_{LMinor,4,conv} = P_{LMinor,4} \cdot 0.19$ [inH2O/psf]   inH2O

$P_{v,4} = \dfrac{\rho_{vac,conv} \cdot U_{jet}^{\,2}}{2}$ psf

$P_{v,4,conv} = P_{v,4} \cdot 0.19$ [inH2O/psf]   inH2O

Cross Section 2 to 3 (Duct)

$D_{23} = \dfrac{2.75}{12}$ ft

$U_{23} = U_{jet} \cdot \dfrac{D_4^{\,2}}{D_{23}^{\,2}}$ ft/s

$$Re_{23} = \rho_{vac,conv} \cdot U_{23} \cdot \frac{D_{23}}{\mu_{vac,conv}}$$

$$\varepsilon_{23} = 0.000005 \quad ft$$

$$\frac{1}{f_{23}^{0.5}} = -2 \cdot \log\left[\frac{\varepsilon_{23}}{D_{23} \cdot 3.7} + \frac{2.51}{Re_{23} \cdot f_{23}^{0.5}}\right]$$

$$L_{23} = 8.25 \quad ft$$

$$P_{LMajor,23} = \frac{f_{23} \cdot \frac{L_{23}}{D_{23}} \cdot \rho_{vac,conv} \cdot U_{23}^2}{2} \quad psf$$

$$P_{LMajor,23,conv} = P_{LMajor,23} \cdot 0.19 \quad [inH2O/psf] \quad inH2O$$

Screen Loss Coefficients

Coarse Mesh

$$\beta_{coarse} = 0.62$$

$$d_{coarse} = \frac{0.054}{12} \quad ft$$

$$K_{coarse} = 6.5 \cdot \left[\frac{1 - \beta_{coarse}}{\beta_{coarse}^2}\right] \cdot \left[U_{23} \cdot \frac{d_{coarse}}{\beta_{coarse} \cdot v_{vac}}\right]^{-0.33}$$

Medium Mesh

$$\beta_{medium} = 0.672$$

$$d_{medium} = \frac{0.0075}{12} \quad ft$$

$$K_{medium} = 6.5 \cdot \left[\frac{1 - \beta_{medium}}{\beta_{medium}^2}\right] \cdot \left[U_{23} \cdot \frac{d_{medium}}{\beta_{medium} \cdot v_{vac}}\right]^{-0.33}$$

Fine Mesh

$$\beta_{fine} = 0.627$$

$$d_{fine} = \frac{0.0065}{12} \quad ft$$

$$K_{fine} = 6.5 \cdot \left[\frac{1 - \beta_{fine}}{\beta_{fine}^2}\right] \cdot \left[U_{23} \cdot \frac{d_{fine}}{\beta_{fine} \cdot v_{vac}}\right]^{-0.33}$$

$$K_{L,23} = K_{coarse} + K_{medium} + K_{fine}$$

$$P_{LMinor,23} = \frac{K_{L,23} \cdot \rho_{vac,conv} \cdot U_{23}^2}{2} \quad psf$$

$$P_{v,23} = \frac{\rho_{vac,conv} \cdot U_{23}^2}{2} \quad psf$$

$$P_{LMinor,23,conv} = P_{LMinor,23} \cdot 0.19 \quad [inH2O/psf] \quad inH2O$$

$$P_{v,23,conv} = P_{v,23} \cdot 0.19 \quad [inH2O/psf] \quad inH2O$$

Summing Sections

$$P_2 = P_{LMajor,23,conv} + P_{LMinor,23,conv} + P_{v,4,conv} \quad \text{inH2O}$$

$$q_{fan} = \frac{\rho_{vac,conv} \cdot U_{23}^2}{2} \cdot 0.19 \quad [\text{inH2O/psf}] \quad \text{inH2O}$$

$$P_{System,Static,vac} = P_2 \quad \text{inH2O}$$

Fan Scaling Laws

$$T_{novac} = 77 \quad \text{F}$$

$$P_{novac} = 1 \quad \text{atm}$$

$$\rho_{novac} = \rho(\text{Air}, T=T_{novac}, P=P_{novac}) \quad \text{lbm/ft}^3$$

$$\rho_{novac,conv} = \frac{\rho_{novac}}{32.174 \quad [\text{lbm/slug}]} \quad \text{slug/ft}^3$$

$$P_{System,Static,novac} = P_{System,Static,vac} \cdot \frac{\rho_{novac,conv}}{\rho_{vac,conv}} \quad \text{inH2O}$$

Appendix D. Calibration Apparatus Bill of Materials

Pkg. Qty.	Description	Quantity to Order	Supplier	Item Number
1	32 Stainless Steel Bolting Cloth, 0.0065" Wire Diameter, 0.0248" Opening, 62.7% Opening	1ft. X 1ft.	Howard Wire	N/A
1	Weather-Resistant Neoprene/EPDM/SBR Foam, Adhesive-Back, 1/8" Thick, 1/4" Wide, 50' Long	1	McMaster	8694K117
1	Corrosion-Resistant 304 Stainless Steel Woven Wire Cloth, 2 x 2 Mesh, .105" Wire Diameter	12"x12"	McMaster	85385T16
1	Corrosion-Resistant 304 Stainless Steel Woven Wire Cloth, 4 x 4 Mesh, .054" Wire Diameter	12"x12"	McMaster	85385T27
1	Soft Buna-N O-Ring Cord Stock, 1/8" Fractional Width, .139" Actual Width	3 ft.	McMaster	9864K27
25	Type 316 Stainless Steel Socket Head Cap Screw, 10-24 Thread, 1/2" Length	1	McMaster	92185A242
25	Type 316 Stainless Steel Socket Head Cap Screw, 10-32 Thread, 1/2" Length	1	McMaster	92185A989
1	Black-Oxide Alloy Steel Socket Head Cap Screw, 1/4"-20 Thread, 9" Long	4	McMaster	90044A311
10	Alloy Steel Flat-Head Socket Cap Screw, 1/4"-20 Thread, 9/16" Long, Black Oxide	1	McMaster	91253A289
1	18-8 Stainless Steel Knurled Head Thumb Screw, Narrow Head, 1/4"-28 Thread, 1" Long	2	McMaster	91746A475
1	Impact-Resistant UHMW Polyethylene Tube, 3-1/8" OD x 2-3/4" ID	2 ft.	McMaster	8705K88
1	Multipurpose 6061 Aluminum, Rectangular Bar, 1/4" x 3/4", 1/2' Long	2	McMaster	8975K594
1	Multipurpose 6061 Aluminum, Rectangular Bar, 3/8" x 3/4", 1/2' Long	2	McMaster	8975K615
1	Multipurpose 6061 Aluminum, 3/8" Thick, 6" x 6"	2	McMaster	9246K473
1	Multipurpose 6061 Aluminum, Rectangular Bar, 3/4" x 2", 1/2' Long	2	McMaster	8975K78

SANYO DENKI

San Ace 70 9GA type
Low Power Consumption Fan

■ Features

Low Power Consumption
Realizes a low power consumption of 31.2 W.*

High Static Pressure and High Air Flow
Achieves a maximum static pressure of 860 Pa,
and a maximum air flow of 2.65 m²/min.*

Suitable for 2U Devices
Measuring 70 mm square, this new fan is ideal for 2U sized
equipment.

* : Specification of Model No. 9GA0712P1G001. When PWM duty cycle is 100%.

70×70×38mm

■ Specifications

Model No.	Rated Voltage [V]	Operating Voltage Range [V]	PWM Duty Cycle Note1 [%]	Rated Current [A]	Rated Input [W]	Rated Speed [min⁻¹]	Max. Air Flow [m³/min]	[CFM]	MAX. Static Pressure [Pa]	[inchH₂O]	SPL [dB(A)]	Operating Temperature [°C]	Expected Life Note2 [h]
9GA0712P1G001(0011)	12	10.8 to 13.2	100	2.6	31.2	16,500	2.65	93.6	860	3.45	65	−20 to +70	40,000/60°C (70,000/40°C)
			0	0.16	1.92	4,400	0.70	24.7	61	0.24	30		
9GA0712P1H001(0011)			100	1.1	13.2	12,000	1.92	67.8	465	1.83	57		
			0	0.07	0.84	2,500	0.40	14.1	20	0.08	19		

The numbers in ( ) represent ribless models
Note1 : PWM Frequency : 25kHz
Note2 : Expected life at 40 degreeC ambient is just reference value.

■ Common Specifications

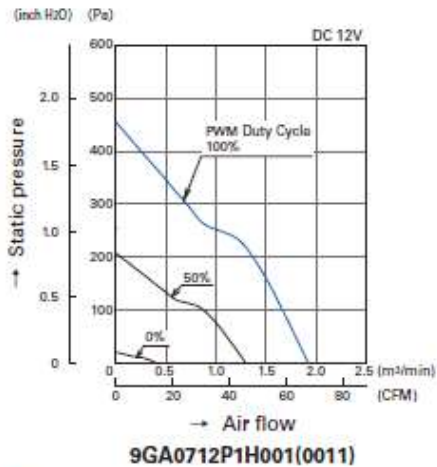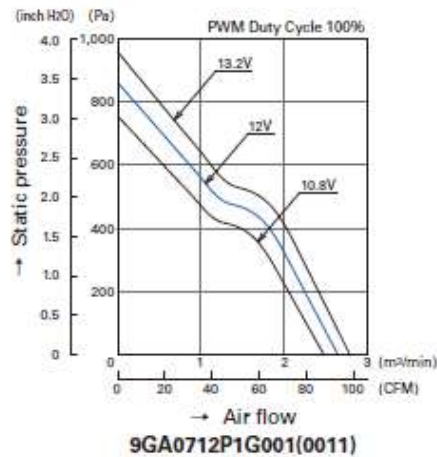|	
☐ Material	Frame, Impeller : Plastics (Flammability: UL94V-0)
☐ Expected Life	Varies for each model
	(L10: Survival rate: 90% at 60°C, rated voltage, and continuously run in a free air state)
☐ Motor Protection System	Current blocking function and Reverse polarity protection
☐ Dielectric Strength	50/60 Hz, 500VAC, 1 minute (between lead conductor and frame)
☐ Sound Pressure Level (SPL)	Expressed as the value at 1m from air inlet side
☐ Operating Temperature	Varies for each model (Non-condensing)
☐ Storage Temperature	−30°C to +70°C (Non-condensing)
☐ Lead Wire	⊕Red ⊖Black Sensor: Yellow Control: Brown
☐ Mass	Approx. 170g

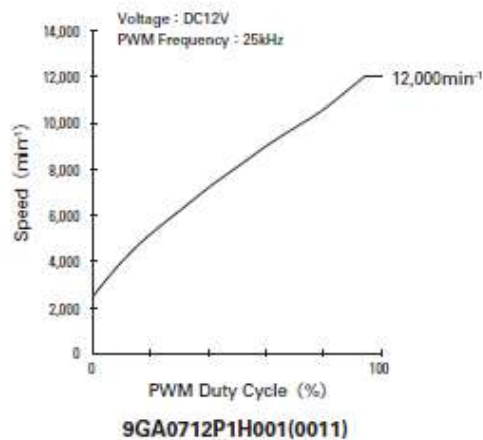# San Ace 70 9GA type
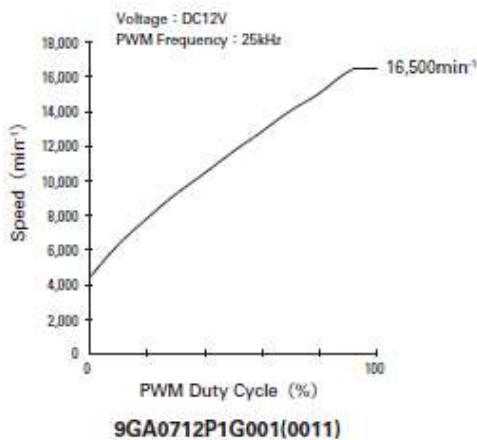
■ Air Flow - Static Pressure Characteristics

- PWM Duty Cycle

9GA0712P1G001(0011)

- Operating Voltage Range

9GA0712P1G001(0011)

9GA0712P1H001(0011)

9GA0712P1H001(0011)
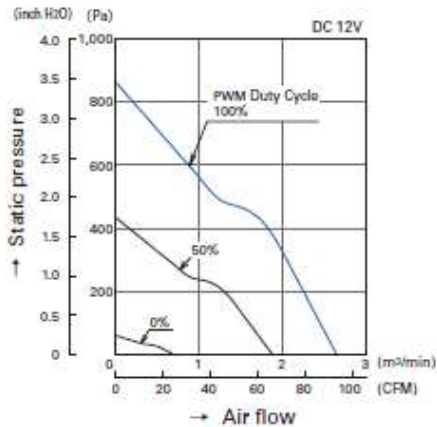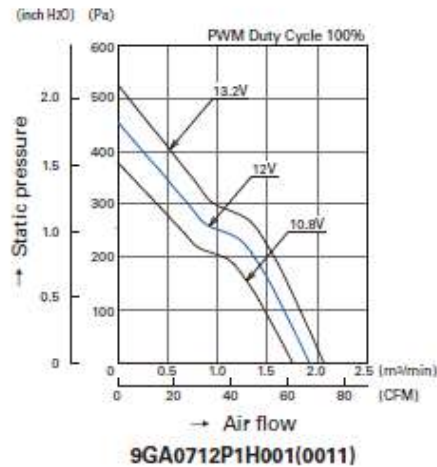
■ PWM Duty - Speed Characteristics Example

Voltage : DC12V
PWM Frequency : 25kHz

16,500min⁻¹

9GA0712P1G001(0011)

Voltage : DC12V
PWM Frequency : 25kHz

12,000min⁻¹

9GA0712P1H001(0011)

■ PWM Input Signal Example

Input Signal Waveform
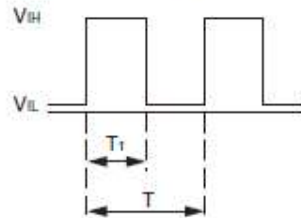
V_{IH}=4.75V to 5.25V

V_{IL}=0V to 0.4V

PWM Duty Cycle (%) = $\frac{T1}{T}$ ×100

PWM Frequency 25 (kHz) = $\frac{1}{T}$

Source Current (Isource) : 1mA Max. at control voltage 0V

Sink Current (Isink) : 1mA Max. at control voltage 5.25V

Control Terminal Voltage : 5.25V Max. (Open Circuit)

When the control lead wire is open,
speed is same as one at 100% PWM duty cycle.

This fan speed should be controlled by PWM input signal of either
TTL input or open collector, drain input.

■ Example of Connection Schematic
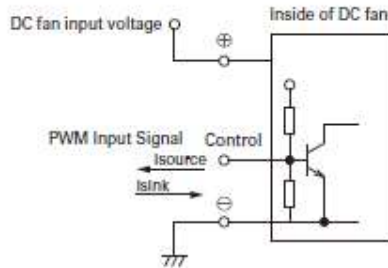
■ Specifications for Pulse Sensors

Output circuit : Open collector

V_{α} = +13.8V MAX.

Ic=5mA MAX. [V_{α} (SAT) =0.6V MAX.]
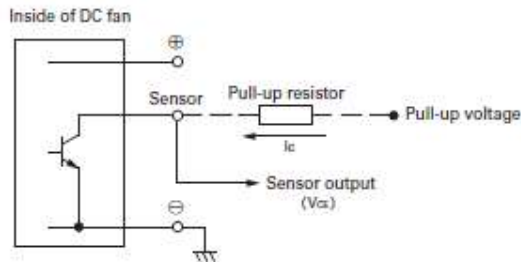
Output Waveform (Need pull-up resistor)

In case of steady running
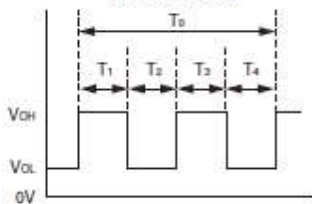
$T_{1\sim4} \fallingdotseq$ (1/4) T_0

$T_{1\sim4} \fallingdotseq$ (1/4) T_0=60/4N (sec)

N=Fan speed (min⁻¹)

■ Dimensions (unit : mm) (With ribs)

4-φ4.5±0.3
Mounting Hole

70±0.5
61.5±0.3

+50
300   0

(10)

61.5±0.3
70±0.5

Lead Wire
AWG24
UL1430

Rotating Direction

(4)   (4)
38±0.5

Air Flow Direction
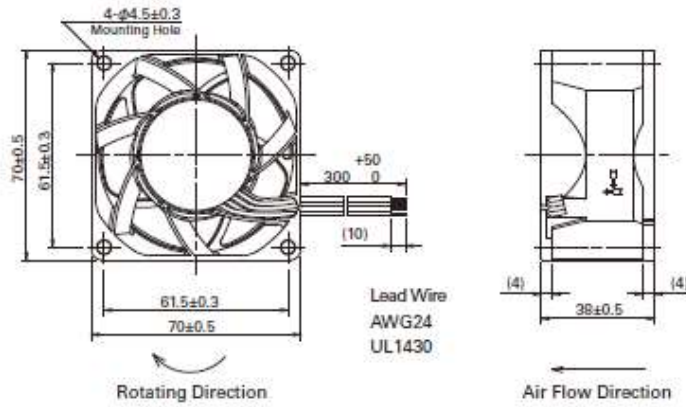
■ Reference Dimension of Mounting Holes and Vent Opening (unit : mm)

Inlet Side

61.5
4-φ4.5
φ74
69
61.5
69

Outlet Side

61.5
4-φ4.5
φ78
69
61.5
69
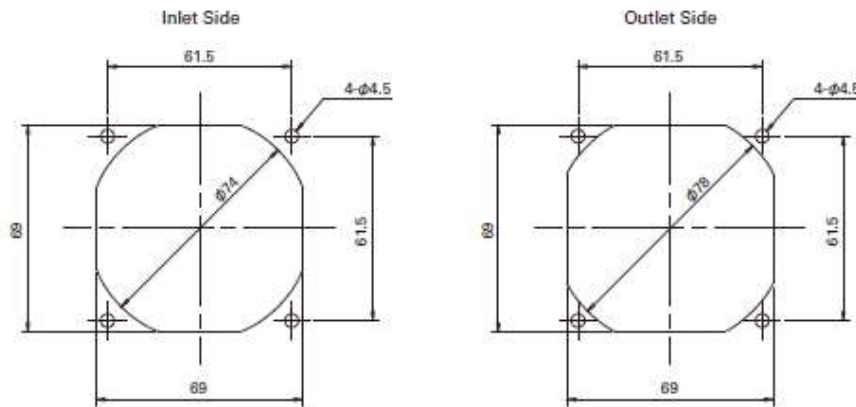
■ Option

Finger guards   Color
Model : 109-1128   Surface treatment : Nickel-chrome plating (silver)

Inlet Side, Outlet Side

4.3±0.3
φ1.6
φ1.6 φ16
91
78

Appendix F. Vacuum Chamber Schematic
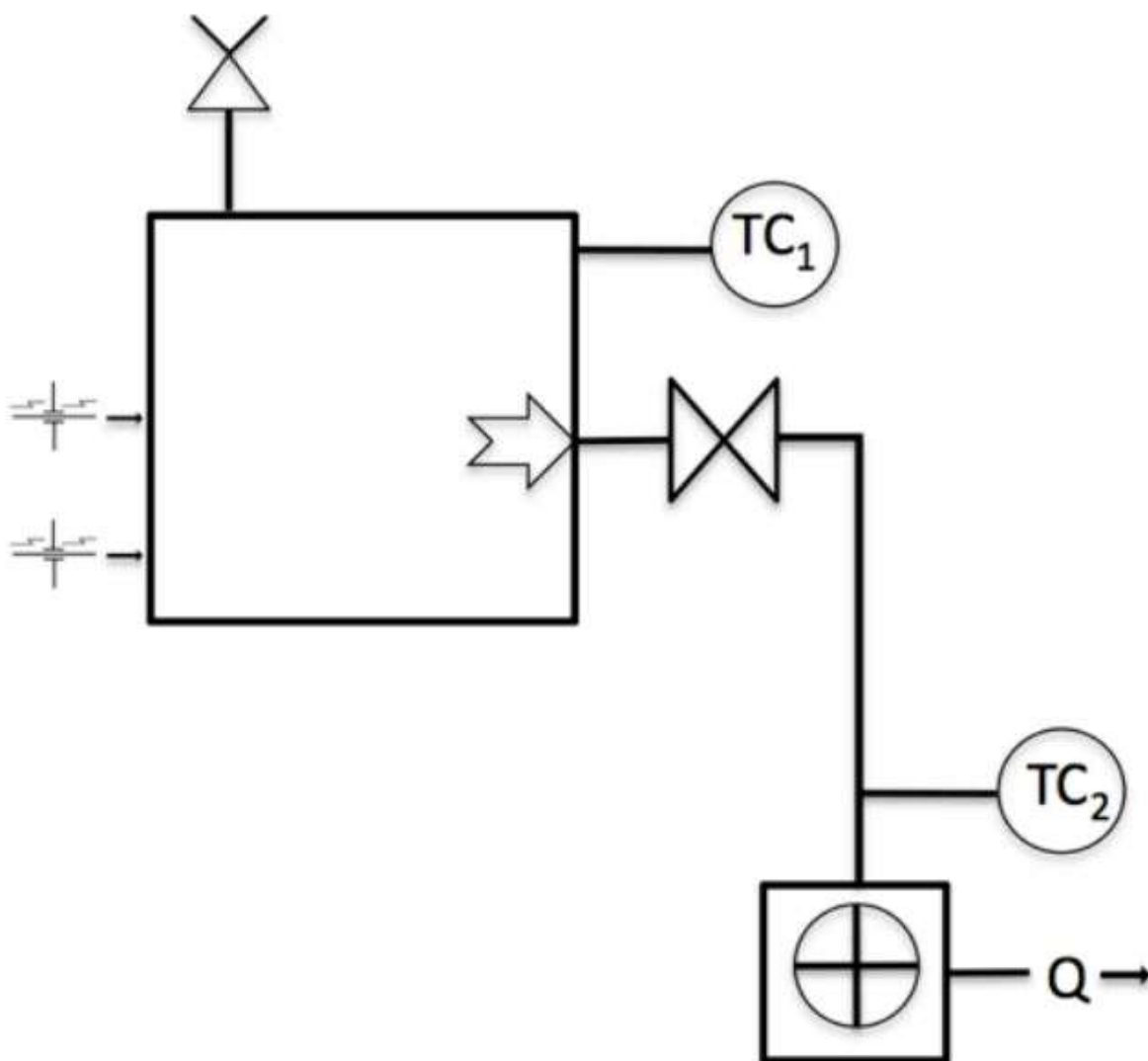
Appendix G.   Uncertainty/Sensitivity Analysis

This appendix formally shows the benchtop CVA uncertainty analysis corresponding to the velocity measurement. In Chapter 3, a comparison was made between the CVA thermal/electrical predictions and the experimental data results from testing inside the vacuum chamber. Uncertainty analysis was performed to determine the major contributing factors to the uncertainty in the velocity measurements corresponding to the CVA output, I_w.

The following equations were used to determine the uncertainty in entirety:

- Sensitivities calculated as: $S_{x_i} = C(x_i + u_{x_i}) - C(x_i) \approx \frac{\partial C}{\partial x_i} u_{x_i}$

- Total uncertainty calculated as: $u_c = \sqrt{\sum S_i^2}$

The variables considered for the analysis included:

- The ambient temperature measured with an Omega HH23 thermocouple reader with a k-type thermocouple.

    o $\pm 5\,^{\circ}\text{C}$

- The static chamber pressure measurement with a Paroscientific.

    o $\pm 100\ \text{Pa}$

- The dynamic pressure measured with a Setra pressure transducer.

    o $\pm 0.004\ \text{V}$

The uncertainties were then used to display the error bars in Figure 3.6 through Figure 3.9.

Appendix H. Single-Point Calibration Implementation Into BLDS

Measure free stream temperature with a thermocouple and free stream velocity using a Pitot tube.

Use the stage to drive the hot-wire to the free stream to choose a V_w that does not exceed R_w.

Slowly increment V_w and measure I_w.

Calculate R_w and decide wether or not to continue increasing V_w.

After determining the flight speed regimes, an R_w should be chosen keeping in mind that it will only increase during flight measurements.